Title

Role of crystal orientation and void location on void growth in polycrystalline metals

Author

Christodoulou, Paul Grant

Publication Date

2023

University of California
Santa Barbara

Role of crystal orientation and void location on void growth in polycrystalline metals

A dissertation submitted in partial satisfaction
of the requirements for the degree

Doctor of Philosophy
in
Materials

by

Paul Grant Christodoulou

Committee in charge:

Professor Irene Beyerlein, Chair
Professor Frank Zok
Professor Tresa Pollock
Professor Frederic Gibou

September 2023

The Dissertation of Paul Grant Christodoulou is approved.

Professor Frank Zok

Professor Tresa Pollock

Professor Frederic Gibou

Professor Irene Beyerlein, Committee Chair

August 2023

Role of crystal orientation and void location on void growth in polycrystalline metals

by

Paul Grant Christodoulou

Curriculum Vitæ

Paul Grant Christodoulou

Education

2023	Ph.D. in Materials (Expected), University of California, Santa Barbara.
2021	M.S. in Materials, University of California, Santa Barbara.
2016	B.S. in Materials Engineering and Science, The Ohio State University

Publications

Callaway, E. B., **Christodoulou, P. G.** & Zok, F. W. Deformation, rupture and sliding of fiber coatings in ceramic composites. *J. Mech. Phys. Solids* 132, (2019).

Samuel, A. F., **Christodoulou, P. G.** & Zok, F. W. Strain fields around strain-concentrating features in fiber-reinforced oxide composites. *J. Am. Ceram. Soc.* 103, (2020).

Christodoulou, P. G., Dancette, S., Lebensohn, R. A., Maire, E. & Beyerlein, I. J. Role of crystallographic orientation on intragranular void growth in polycrystalline FCC materials. *Int. J. Plast.* 147, 103104 (2021).

Christodoulou, P. G., Lebensohn, R. A. & Beyerlein, I. J. Study of the interplay between lower-order and higher-order energetic strain-gradient effects in polycrystal plasticity. *J. Mech. Phys. Solids* 164, 104906 (2022).

Christodoulou, P. G., Zecevic, M., Lebensohn, R. A. & Beyerlein, I. J. Role of grain boundary crystallography on void growth in FCC metals. *Submitted, 2023*

Christodoulou, P. G., Zecevic, M., Lebensohn, R. A. & Beyerlein, I. J. Role of crystallography on void growth in FCC-BCC two-phase metals. *In preparation, 2023*

Rovinelli, A., **Christodoulou, P. G.**, Lebensohn, R. A. & Capolungo, L. Generalization of the concept of gauge factor to predict void growth in single crystals deforming by diffusion and dislocation creep. *In preparation, 2023*

Abstract

Role of crystal orientation and void location on void growth in polycrystalline metals

by

Paul Grant Christodoulou

A better understanding of failure mechanisms in metals allows engineers to build more reliable structural components. One such failure mechanism is ductile failure, defined by the nucleation, growth, and eventual coalescence of voids in a material. This thesis focuses on how crystallographic orientation, as well as triaxiality, grain boundary misorientation, grain or phase boundary inclination, phase orientation relationship, and material differences between two phases affect the growth of voids in polycrystalline metals. Void growth in face-centered cubic (FCC) and body-centered cubic (BCC) metals is studied using two crystal-plasticity (CP) fast-Fourier transform (FFT)-based models: a small-strain dilatational viscoplastic (DVP) FFT algorithm and a large-strain (LS) elasto-viscoplastic (EVP) FFT algorithm. The macroscopic response, including the growth of the void, is in good agreement between the DVP-FFT and LS-EVP-FFT algorithms. The study begins with an investigation of the growth of intragranular voids in single-crystal and polycrystal FCC microstructures. This study indicates that the loading type plays a significant role in the relationship between the crystal orientation and void growth. In strain-rate controlled simulations, voids in the hardest [111] crystals grow the fastest in time, whereas in stress-controlled simulations, voids in the softest [100] crystal grow the fastest in time. Void growth rate increases with triaxiality, which has been widely observed in the literature. Then, intergranular voids in FCC bicrystalline and tricrystalline simulations are studied. This study indicates that the grain boundary misorientation and inclination have very little effect on the overall rate of void growth. Crystal orientation remains a strong indicator of the rate of void growth, although there are some voids at grain junctions that appear to grow faster than within any constituent single crystal. Grain boundary inclination affected how quickly the voids grew within one part of the bicrystal or tricrystal simulations because of the stress and strain rate states in which the inclination angle placed each constituent grain. Finally, the study concludes with a focus on voids at FCC/BCC phase interfaces. This study confirms that the behaviors seen in single-phase bicrystals apply in most cases to biphase interfaces, but the hardening rate difference between Cu and Ta caused the void growth to exceed the average growth rate of a void in each crystal alone. Finally, the void grew slightly faster in the BCC phase when more slip systems were available.

Contents

List of Figures

List of Tables

Chapter 1

Introduction

Over the past century, engineers have leveraged a greater understanding of the mechanisms of damage and failure in metals to build more reliable parts for structural applications. These metallic parts are typically composed of polycrystalline aggregates, whose microstructures comprise crystals with a heterogeneous orientation, size, and shape distribution. The crystal orientation plays a critical role in the mechanical response of polycrystalline metals. The choice of chemistry and processing method influences the texture of the resultant material, which then influences the mechanical response. Crystal orientation dictates, among other things, the yield strength, modulus, and anisotropy. In particular, the orientation of each grain dictates plastic deformation, since plastic slip occurs in discrete planes in crystallographic directions. Behaviors that are plasticity-mediated thus depend on crystal orientation as well. Ductile failure, where voids nucleate, grow, and coalesce, is one such aspect of the mechanical response and is plastically mediated. It is an important aspect of failure, and ongoing research is necessary to understand ductile failure in crystalline materials.

1.1 Ductile failure and its stages

Ductile damage and failure are defined by the nucleation, growth, and eventual coalescence of voids in the material. The formation of voids during material deformation, both under quasistatic and dynamic loading, is well documented [1, 3–8]. Additionally, many as-manufactured metals are highly porous — additively manufactured metals, for example, are generally not fully dense [9–13]. Voids generally appear spherical, but upon coalescence connecting threads join the voids, as in Figure 1.1. Because materials are crystalline, the crystallographic nature of the material plays a role in all three stages of void nucleation, growth, and coalescence.

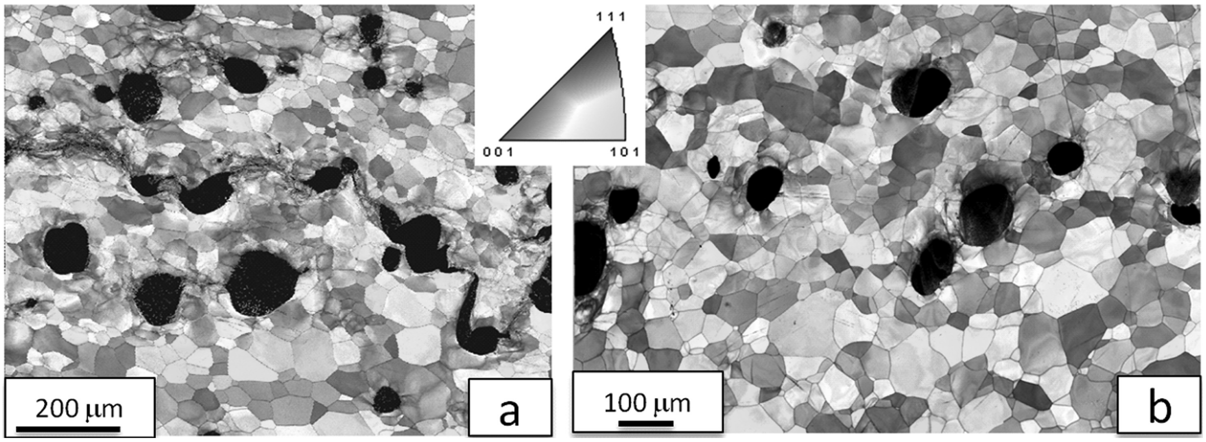

Figure 1.1: Damage in shocked Ta, showing (a) spherical voids that have begun to coalesce and (b) spherical voids with very few localization linkages. Reproduced from Bronkhorst et al. [1].

Voids nucleate at various locations within crystalline media. Void nucleation in single crystals occurs only by the coalescence of vacancies [14, 15], but in polycrystals, the formation of voids can occur at the boundaries of defects [3–7, 15]. In engineering materials with precipitates, voids may be found inside the interior of the ductile grain after decohesion occurs at the grain-precipitate interface [3–5, 15]. In single-phase materials where precipitates are not present, voids typically nucleate at grain boundaries and higher-order junctions such as triple junctions and quadruple points [6, 7]. Recent MD simulations [16] suggest the formation of voids at twin interfaces during the dynamic deformation process of BCC. The twins undergo a reverse transformation, and the voids remain within the grain interior without any indication of a twin. Thus, even when ex situ studies do not observe voids near grain boundaries, this does not necessarily prove that the voids did not nucleate at a grain boundary. In multiphase metals, voids can also form at the phase boundary [17]. However, high strain rate tests of Cu / Nb have indicated that spallation occurs in Cu, rather than at the Cu/Nb interfaces [8]. This could have occurred at poorly bonded Cu/Cu interfaces as a result of the processing method, although this is speculation.

Void growth occurs by one or more of the three proposed mechanisms: dislocation loop emission from the void surface [18–21], vacancy diffusion assisted by mechanical or chemical driving force [22], or dislocation adsorption from the material [23, 24]. It has also been proposed that these mechanisms operate in different strain-rate regimes, where dislocation loop emission is the primary mechanism during dynamic loading, while a different mechanism, such as dislocation adsorption, is the primary mechanism at lower strain rates [23, 24], with the vacancy diffusion method acting simultaneously at low strain rates. These mechanisms are all plastically mediated processes.

Dislocations, described as line defects (an irregularity in the crystalline material), and their movement are important mechanisms of plasticity. Dislocation movement is generally divided into glide and climb, and crystal orientation affects both. In dislocation glide, the dislocation move within a slip plane, which is dependent on the phase. The particular slip direction and plane (called a slip system) are related to the external loading and the crystal orientation, defining the impetus and available slip systems. Dislocation climb is a diffusion-based process in which the dislocations move out of the slip plane. Climb is dependent on the movement of vacancies and is thus a diffusion-based process.

However, mechanical loading can affect the movement of vacancies, and the specific stress state is a function of crystal orientation in crystals with anisotropic elastic properties. Most models, described in the next section, focus on void growth using various models of plasticity.

The length scale of the void also affects its behavior. Nanovoids, for example, act as barriers to dislocation slip [25–29]. Larger voids act as stress concentrators, causing the material to plastically deform at lower external loads, further propagating void growth. Work hardening is present around the voids, which slows the surrounding plasticity and thus void growth [30]. Witzen et al. [31] showed the development of shell-like regions with a high dislocation density around voids in shocked Ta. These regions then show elevated plastic activity around the voids, which then harden, slightly slowing the void growth.

Ductile failure, also termed ductile fracture, terminates with the coalescence of voids. This process is first characterized by plastic flow localization in the material, typically by necking of the intervoid ligaments [32–34]. This constrained plastic flow slows the void growth until the material can no longer sustain any more force and fractures, causing two or more voids to become one. Beyond coalescence by necking, voids can coalesce in a shear band or in columns [34], although these mechanisms are not as frequently observed.

Coalescence cannot occur without the voids first occupying sufficient space to lead to plastic flow localization. While the first and third stages are key elements in ductile fracture, the research in this dissertation focuses only on void growth, a topic that has long been the focus of modeling.

1.2 Models of void growth

1.2.1 Implicit models

Implicit or analytical models, i.e., where voids are not explicitly modeled, have been developed for void growth.

Historical void growth models, such as those developed Rice and Tracey [35] and later by Gurson, Tveegard, and Needleman [32, 33, 36–39], have typically been limited to analytical solutions of one void in a homogeneous material or a regular array of voids in a homogeneous material, primarily due to computational limitations. These models were developed for solids that are rigid-perfectly plastic and obey the von Mises yield criterion and define a yield surface for a porous medium given a macroscopically applied stress using an upper bound approach. The yield surface for spherical voids is

$$\left(\frac{\Sigma_{\mathrm{eq}}}{\sigma_0}\right)^2 + 2q_1 f \cosh\left(\frac{3}{2} q_2 \frac{\Sigma_m}{\sigma_0}\right) - 1 - q_3 f^2 = 0, \tag{1.1}$$

where Σ_{eq} and Σ_{m} are the macroscopic von Mises equivalent and hydrostatic stresses, respectively, q are values that account for void interactions (although typically only q_1 deviates from unity), f is the porosity, and σ_0 is the yield stress of the solid. The value of the applied von Mises stress will always be less than the yield stress of the solid for porous materials, $f > 0$. From there, a flow law can be derived using the normal to this yield surface. This flow surface can then be used within simulations as an implicit model.

The classical model applies to a homogeneous, isotropic, perfectly-plastic solid, and as such, others have extended the model to account for various heterogeneities and power-law plasticity [40–47]. Several models have sought to understand the growth of voids in the context of heterogeneous crystalline materials, typically homogenizing the polycrystalline matrix's properties and then applying anisotropic extensions of limit-analysis models [44, 45, 47]. More recently, Han et al. [48] developed an implicit model for a crystalline material that followed power-law viscoplastic crystal-plasticity, and a new model is being developed by Rovinelli et al. [49] to account for interacting voids in single crystals over a range of porosities, crystal orientations, and power-law exponents.

These models generally are empirical, and are fit to experimental or simulation data, whether finite element or another discretization method, at the hydrostatic and deviatoric limits. Implicit models are useful for simplifying the void-material and void-void interactions at the continuum level, but the behavior for voids in heterogeneous materials is inherently more complex than any implicit model. Implicit models cannot yet capture the full range of simulation possibilities. However, they can give us insight on overall trends that should be present. Firstly, yield stress is depressed as porosity increases, and the flow rate (and thus void growth) increases as voids grow, barring any hardening in the material. Voids interact with one another, increasing void growth further. Looking alone at Equation 1.1, the yield stress is depressed as the stress triaxiality increases, that is, the ratio of hydrostatic stress to the von Mises stress. This then translates to a faster growth rate as the triaxiality increases, a fact that is well documented in explicit simulations [2, 24, 50–52].

1.2.2 Explicit models

The models employed to develop these implicit models need to capture the local interactions of the material at the boundary of the void. Heterogeneity is apparent at the mesoscale, with the presence of grains with different crystallographic orientations relative to the loading direction. Because the deformation of one grain can affect the deformation of the grains surrounding it, mean-field techniques, in which an individual feature's response is determined by its interaction within a homogenized matrix that represents all other features, can over-generalize the behavior of the material, and cannot model the interactions between heterogeneities. A mean-field technique may capture the approximate global behavior, but it neglects any neighborhood effects. And since the local stress and strain tensors around the void may differ from their global counterparts due to the grains surrounding them (the so-called grain neighborhood), it is insufficient to use macroscopic loading alone to determine void growth in highly heterogeneous materials.

Thus, full-field models, wherein the response of each material feature is determined within its heterogeneous neighborhood, have the ability to fill this gap in knowledge of how voids typically grow at the local level. A variety of full-field techniques are available to treat void growth in metals. Four techniques will be described now, for context: Molecular Dynamics (MD), Dislocation Dynamics (DD), Finite Element Analysis (FEA), and the technique employed in this dissertation, Fast-Fourier Transform (FFT)-based modeling.

Beginning with the smallest length scale, MD is a computational technique that simulates the movement of atoms given a known electronic potential. This method has been used to confirm the mechanisms of void growth in crystalline materials, having shown that dislocation loop emission was the primary mechanism for void growth [53–59], but not in quasi-static loading [60], where dislocation adsorption appears to dominate void growth [24]. MD simulations have demonstrated that grain orientation has a profound effect on void nucleation and growth, not only in single crystals [55, 57, 61–65], but also in bicrystals and tricrystals [16, 53, 66]. It has also been found that voids can move towards grain boundaries when void and grain boundary are within a few nanometers [67]. It is important to note that the mechanisms of growth in quasi-static loading are not necessarily the same, as noted above. While MD is an excellent choice for understanding the fundamental mechanics during dynamic loading, the necessary time scale prohibits this technique from fully assisting the understanding void growth in quasi-static loading.

Moving up in length scale, DD is a method that does not model individual atoms, but rather describes dislocations, using their interactions to describe the rather stochastic nature of dislocation movement in metals. This technique has not been used widely to describe void growth, but Segurado and Llorca [68, 69] and Chang et al. [23] have demonstrated in multiple studies on voids in FCC single crystals that the flow stress and strain-hardening rate increased as the void size decreases (in their work routinely labeled "smaller is stronger"), and the void growth rate increases with void size ("smaller is slower" or "the larger, the faster"), both trends which were more apparent as triaxiality increased. They also found that strain-hardening rate increased and void growth rate decreased as the number of active slip systems increased, but only in the case when the plastic deformation along said systems were incompatible with externally applied deformation. They also noted that void size limited dislocation shearing/adsorption, with submicron voids lacking sufficient active dislocation sources near the void surface.

The final length scale, which will be the focus of this dissertation, is the so-called "mesoscale" which does not simulate individual atoms, but rather the directional properties of metals. The term mesoscale is used here to describe the scale below a macroscale part, at the grain scale. The two techniques that will be discussed in this context are FEA and FFT-based algorithms, both of which perform numerical calculations on discrete units of material, without explicitly modeling atoms or dislocations. Most commonly, void studies at this scale use either isotropic plasticity or crystal plasticity constitutive models. The latter class of models, developed by Asaro [70] and used widely in these mesoscale techniques to understand the orientation-dependent plastic properties of metals. Crystal plasticity is predicated on the idea that plastic movement occurs in specific slip directions and in distinct slip planes. Slip is treated at the grain level, noting the orientation of the grain and using slip directions and planes to define the slip, but not explicitly defining discrete atoms or dislocations. The slip systems for each phase are defined, and the crystal orientation are explicitly defined.

The first technique, FEM, is a numerical method to solve a boundary value problem by subdividing the system into finite elements, forming a mesh (the numerical domain of the solution) composed of polygonal or polyhedral units. FEM calculations of voids in polycrystalline media have been conducted extensively to demonstrate growth in single crystals [2, 48, 50, 52, 71], at grain boundaries and triple junctions [51, 72], and phase boundaries Asim et al. [73], demonstrating that the orientation dependence of plasticity strongly affects void growth. Simulations have also indicated that the trends related to void growth rate seen in single crystals are reversed when the void is placed at a bicrystal [74]. Several simulations have leveraged polycrystalline materials with interacting voids to develop implicit models Fritzen et al. [75]. Simulations generally demonstrate that void growth rate increases with triaxiality, and that void growth rate is dependent on the grain orientation of the surrounding material, albeit studies have not extensively sought to understand how load vs displacement controlled deformation affects that parameter.

The FFT-based methodology is another micromechanical technique that was originally conceived as an efficient alternative to FEM, and is the principal methodology used in this dissertation. FEM is limited in complexity and size due to meshing difficulties and the large number of degrees of freedom, while FFT is a meshless technique. FFT-based formulae require periodic unit cells and provides a solution of the governing equations of equilibrium and compatibility, limited only by the discretization and iterative nature of the numerical algorithm, so that the converged stress and strain fields require the constitutive relation at every discrete point. Moulinec and Suquet [76, 77] developed the FFT algorithm to calculate the local and effective mechanical response using the image contrast of pixel-based optical images of materials to determine the spatial distribution of the constituent phases, given the mechanical properties of the phases as inputs. While developed originally for linear elastic and nonlinear elastoplastic [76, 77] and later viscoplastic composites [78, 79], the method was later adapted for visoplastic [80–82], and elasto-viscoplastic [83, 84] polycrystalline materials, such as metals. Most recently, the method, typically couched in a small-strain framework, has been adapted to a finite-strain framework [84–89], making it comparable to most commercial FEA software. The FFT method for polycrysttaline materials with directional mechanical properties is ideal for use with pixel-based orientation images (e.g. Electron Backscatter Diffraction).

The FFT algorithm iteratively adjusts a compatible strain or strain-rate field that is related to an equilibrated stress field through a constitutive potential to minimize the average of local work or power. The use of a periodic unit cell and Green functions, Fourier transforms of the fields can be taken to efficiently solve the micromechanical problem. However, the requirement of the periodic microstructures makes the FFT-based formulation less general than FEA. Additionally, while FEA can form relatively smooth curved surfaces, FFT has been historically constrained to regular, rectangular grids—although this has been recently remedied by Zecevic et al. [89].

Dilatational schemes for pore growth were developed by Lebensohn et al. [90, 91] to treat pore growth in porous crystalline media. However, FFT simulations of porous media have been limited. Bilger et al. [92] demonstrated that void clustering enhanced void growth in an isotropic, perfectly plastic material. Studies intended for studying the dilatational plastic response under various applied stress conditions without evolving the porosity evolution represent the majority of studies for FFT [90, 93–95]. The DVP-FFT algorithm was used by Lebensohn et al. [91] to demonstrate that the growth rate in FCC polycrystals obeying a power-law slip constitutive equation was not identical to that of a homogeneous isotropic matrix following power-law plasticity. Notably, they found that certain crystals lying between two voids could either enhance plastic activity and thus void growth, or suppress it, simply based on the crystal orientation relative to the loading direction.

1.3 Problem statement and outline

While there has been work completed to understand void growth in crystalline materials, void growth in highly heterogeneous materials is still not well understood. The aim of this dissertation research is to further our understanding of how the crystallographic nature of metals, both single phase and biphase, affects void growth in face-centered cubic (FCC) and body-centered cubic (BCC) metals. A particular focus is to what extent the void neighborhood affects the void growth, and we attempt to pinpoint what microstructural features contribute to void growth. Since void growth is mediated by plasticity, we quantify plastic deformation in the neighborhood.

There is a need to further understand the growth of mesoscale voids within a heterogeneous crystalline medium. When a void lies within a heterogeneous neighborhood—at a grain boundary, phase boundary, triple junction, etc.–its growth is not generally perfectly symmetric about the initial location. Voids the size of grains are often found prior to coalescence, and there have been mesoscale studies of void growth, but more work is necessary to understand the micromechanical effects of crystallinity on void growth. Void growth is often faster in the direction where deformation occurs most easily, i.e. into a soft crystal. A particular focus on what metrics dictate growth, and how best to quantify growth, is part of this study. It is important to compare what we see in homogeneous materials to the heterogeneous materials. The local fields resulting from the microstructural response and the macroscopic fields based largely on the externally applied boundary conditions are tracked for deviations that could not be determined in mean-field techniques. The purpose of this dissertation research is to explore void growth and understand key gaps in knowledge, in such a way that could be useful for implicit models in the future. It is insufficient to couch the ultimate failure of the material in terms of its macroscopic properties and the hydrostatic stress alone. Key microstructural populations exist, intrinsic to a material and its processing method, which determine the extent of void growth and onset of coalescence.

The focus of this dissertation is on mesoscale growth of voids from plastic glide at the grain level using a quasi-static micromechanical model. Using a full-field technique assists us in determining how grains grow within heterogeneous materials. This research uses two fast-Fourier transform (FFT)-based solvers, with some modifications from their original formulation to quantify void growth. These methods are quasi-static in nature, although we seek to study the dynamic properties of this material by simulating triaxialities found as a result of shock loading. The simulations within this dissertation explicitly model voids using power-law crystal plasticity constitutive equations to explore the nature of void growth in crystalline media. The simulations herein use a dilatational viscoplastic (DVP) FFT model, with minor modifications for use with porous single crystals, as well as the more recently developed large-strain (LS) elasto-viscoplastic (EVP) FFT model, or LS-EVP-FFT, to determine void growth.

The research in this dissertation tests the hypothesis that both the void neighborhood and loading state are the major determiners in how quickly a void grows. This dissertation will demonstrate studies voids in various neighborhoods: within grains aligned at different orientations with respect to loading, at grain boundaries, and at phase boundaries. In each case, quantifying void growth rate and direction allows us to identify those neighborhoods.

In this dissertation, void nucleation will not be studied. Instead, voids will be placed in one of three settings: (1) entirely within a grain, termed either “voids in grain interiors” or “intragranular voids;” (2) intersecting a grain boundary, referred to here as “voids at grain boundaries” or “intergranular voids;” or (3) at a phase boundary (“voids at phase boundaries” or “interphasic voids”). Void growth, the middle stage of ductile failure, is the focus of this research.

This dissertation is structured with the intention of starting with the simplest of microstructures and progressively increasing in complexity. The dissertation focuses the effects of crystallographic character on void growth, beginning with a study on intragranular voids in FCC single crystals and polycrystals, exploring voids at FCC grain boundaries and triple junctions, and finishing with void growth at BCC/FCC phase boundaries. Specifically, chapter 2 discusses the growth of voids in FCC single crystals and polycrystals, modeled using a dilitational viscoplastic (DVP) fast-Fourier transform (FFT) algorithm; chapter 3 describes a large-strain elasto-viscoplastic (LS-EVP) FFT algorithm and its modifications, as well as show some key void growth comparisons to analytical solutions, FEA, and the DVP-FFT model; chapter 4 shows void growth at grain boundaries and triple junctions in FCC metals modeled using the modified LS-EVP-FFT; chapter 5 shows voids at FCC/BCC phase boundaries modeled using LS-EVP-FFT; chapter 6 outlines the general conclusions that can be drawn from these studies; and chapter 7 poses additional questions and recommend future avenues of study that would benefit our further understanding of void growth.

Chapter 2

Void growth in grain interiors

2.1 Introduction

Over several decades, progress in the fundamental understanding of damage and failure of metallic materials has enabled the engineering of more reliable structural components. In most applications, metallic parts are polycrystalline aggregates made of anisotropic crystals of complicated shapes containing a variety of defects. This complexity determines microstructure-sensitive damage and failure behavior under thermo-mechanical processing. Recent advances in materials characterization techniques include *in situ* 3-D microscopic visualization of ductile damage due to porosity evolution, from nucleation to growth and coalescence of cavities. In polycrystalline materials, these techniques revealed a large diversity in void growth-rates likely due local crystalline environments [96, 97]. Despite these recent experimental observations, damage and failure models remain largely insensitive to local microstructural characteristics, due to a lack of consideration of the controlling processes at the scale of single crystals, whose elastic and plastic properties vary from grain to grain depending on orientation and, in some cases, are strongly anisotropic. Dealing with and quantifying these microstructural effects on ductile damage from a micromechanical perspective requires combining single crystal/polycrystal plasticity and dilatational plasticity models, which is the main focus of this chapter. When the metal contains inclusions, which is the case for most industrial alloys, damage nucleation is connected to these inclusions (e.g. Goods and Brown [98]) and these inclusions are not always located at grain boundaries, especially when grains are large. As a consequence, it is important to study intragranular growth of cavities.

Crystal plasticity (CP) models, which approximates plastic deformation accommodated by dislocation slip in single crystals, have been combined with the finite element (FE) method (e.g. Roters et al. [99]) to account for spatial variations of mechanical properties of fully-dense polycrystalline materials. The implementation of CP constitutive behavior in FFT-based formulations, conceived as an efficient alternative to CP-FE (e.g. Lebensohn [80], Lebensohn et al. [81] in the rigid-viscoplastic (VP-FFT) regime, Lebensohn et al. [83] and Eisenlohr et al. [84] in the small-strain and large-strain elasto-viscoplastic (EVP-FFT) regimes), has enabled fine-scale microstructural information in polycrystalline materials to be accounted for with an unprecedented level of detail.

Analytical dilatational plasticity models, on the other hand, describe the growth of a cavity in a plastically deforming homogeneous matrix. These models are largely based on the analysis of the mechanical response of a hollow sphere with isotropic rigid-perfectly plastic behavior and were pioneered by Rice and Tracey [35] and Gurson [36], and have been generalized to consider different geometries and material behavior [40–47]. Other analytical homogenization methods were extended to the problem of dilatational plasticity [100, 101]. Concurrently, FE-based cell calculations have been used extensively, either in purely numerical studies, or for validation and calibration of analytical dilatational plasticity models, including the study of void growth in single crystals [2, 48, 50, 52, 71]. A number of similar studies conduct simulations on single crystals and a singular void at a grain boundary or triple junction [51, 73]. These integrated dilatational/single crystal plasticity analyses and numerical calculations showed that the directionality of the plastic response of the single crystal strongly affect void growth. However, the ideal configurations considered by the aforementioned analytical and numerical dilatational plasticity models are unable to capture the complex way in which the microstructure of polycrystalline materials affects damage evolution associated with void growth. For such more realistic configurations, analytical expressions are not available and numerical models are very limited. Analytical model extensions may be adopted to capture some effects related polycrystalline character of the matrix, e.g. texture-induced plastic anisotropy, by first homogenizing the polycrystalline matrix's properties and then applying anisotropic extensions of limit-analysis models [44, 45, 47]. Liu et al. [102] conducted a series of CP-FE simulations on a single void in a heterogeneous FCC polycrystal with random orientations. They found that macroscopic triaxiality played an important role in the growth of voids, and that at lower triaxialities, the effect of the orientation of the crystals around the void had a greater effect on the void growth, particularly the dispersion of said growth between individual simulations. Ultimately, they proposed a statistical micro void growth model to capture the dispersion of the results from the study. There is relatively little studied on orientation effects within polycrystals. One exception is this study Liu et al., although the study used only CPFEM, and only includes one void in the central grain with a cuboid arrangement of grains. In addition, less orientations are simulated than in the current study.

Only a handful of numerical simulations have dealt with configurations involving multiple interacting voids. In the context of FE, Fritzen et al. [75] investigated the effective material response of metals with multiple spherical voids for different volume fractions with varying loading types. It was found that the Gurson–Tvergaard–Needleman [103] analytical model only required one additional parameter to efficiently predict the macroscopic stress for all examined porosities. Ghosh et al. [104] performed FE calculations on a metal with hard inclusions and individual, albeit isotropic, domains representing grains. The source of the heterogeneity was the voids that eventually formed near the inclusions.

In the context of FFT-based models, Bilger et al. [92] performed calculations on isotropic, perfectly-plastic materials with voids in various configurations to determine the effect of the void distribution on yielding. These simulations showed that the clustering of voids reduced the yield strength of the material, which motivated Bilger et al.'s [105] proposal of analytical expressions to predict the yield stress of a material using a clustering parameter. However, they found that at high triaxialities, the yield strength was difficult to predict in microstructures with highly clustered voids. None of these models, neither in FEA nor FFT-based simulations, used crystal plasticity, and as such lacked the ability to account for crystal orientation.

Lebensohn et al. [90] and Vincent et al. [94] used FFT-based methods with explicit representation of voids in polycrystalline and isotropic matrices, respectively, but their analysis was limited to fixed configurations, i.e. studying the dilatational plastic response under different applied stress conditions, but without porosity evolution. Lebensohn et al. [91] extended the VP-FFT formulation to account for dilatational effects (resulting in dilatational viscoplastic (DVP-FFT) formulation) associated with the presence of intergranular voids in a polycrystalline matrix. This DVP-FFT model included specific algorithms inspired by the particle-in-cell (PIC) method (e.g. Sulsky and Schreyer [106], FFT-based implementation of Lahellec et al. [85]) to take porosity evolution into account. DVP-FFT calculations allowed, for the first time, consideration of microstructural effects on porosity growth-driven ductile damage, with crystals and voids represented explicitly. In particular, DVP-FFT calculations were performed on two materials with identical initial porosity distribution: one representing an FCC polycrystal with uniform texture and intergranular cavities, and the other representing a porous material with homogeneous isotropic matrix. Comparative calculations were performed on these two materials to study the effect of the matrix's polycrystallinity on porosity evolution.

Although intragranular growth of cavities in single crystals is a widely studied topic, our findings are not completely in line with some previous results and, to the authors' knowledge, no CPFE vs. FFT comparisons have been conducted within this field. In addition, a very limited number address void growth in polycrystals, and none attempting to decorrelate the effect of crystallographic orientation and grain neighborhood as we have done here.

In this chapter, we study the effect of crystallographic orientation and applied triaxiality on the growth of intragranular spherical voids. Note that we focus on the void growth stage of ductile damage, assuming pre-existing voids that have already nucleated in the interior of crystals/grains, and not considering the late stage of void coalescence. We employ the DVP-FFT and CPFE formulations, which both incorporate a combination of crystalline plasticity and dilatational plasticity and permit explicit representation of intracrystalline voids. Such voids would occur, for example, by decohesion or fracture of second-phase particles in the grain interiors of engineering materials. For several single crystal orientations and triaxialities, we demonstrate that predictions of void growth from both formulations agree reasonably well. Based on this cross-validation, we proceed to employ the more computationally efficient DVP-FFT to investigate intragranular void growth in polycrystalline microstructures, wherein every crystal contains a single intragranular void. We show that whether the loading type is full-stress controlled or longitudinal strain-rate/stress-triaxiality controlled plays a significant role of the orientation vs. growth rate relationship. In strain-rate controlled conditions, voids in the hardest [111]-crystals grow the fastest in time, whereas in stress-controlled conditions, voids in the softest [100]-crystal grow the fastest in time. The implications of these results are discussed, particularly focusing on the interplay between orientation, triaxiality, and loading types.

The plan of this chapter is as follows: In section 2.2 we present relevant details on the basics and modifications of the DVP-FFT and CP-FE to account for dilatational effects in single crystals and polycrystals with intragranular cavities, as well as the simulations conducted to probe the effect of lattice orientation on intragranular void growth. Section 2.3 presents a comparison of void growth in single crystals under axisymmetric tension, with different crystal orientations aligned with the major tensile axis and different stress triaxialities, predicted with DVP-FFT and CP-FE, followed by a comprehensive study of orientation effects on intragranular void growth using DVP-FFT in both single crystals and polycrystals. The implications of these results are discussed in the same section, particularly focusing on the interplay between orientation, triaxiality, and loading types. Finally, key takeaways of this study and outstanding questions are addressed in section 2.4.

2.2 Method and Simulation Procedures

2.2.1 Single crystal viscoplastic behavior

In the current configuration, the viscoplastic behavior of a single crystal material point is described by means of the following non-linear, incompressible, rate-sensitive equation relating the Cauchy stress σ and the Eulerian plastic strain rate $\dot{\varepsilon}$ at point $\mathbf{x}$:

$$\dot{\varepsilon}(\mathbf{x}) = \sum_{k=1}^{K} \mathbf{m}^k(\mathbf{x})\dot{\gamma}^k(\mathbf{x}) = \dot{\gamma}_0 \sum_{k=1}^{K} \mathbf{m}^k(\mathbf{x}) \left(\frac{\left|\mathbf{m}^k(\mathbf{x}) : \sigma(\mathbf{x})\right|}{\tau^k(\mathbf{x})} \right)^n \operatorname{sgn}\left(\mathbf{m}^k(\mathbf{x}) : \sigma(\mathbf{x})\right) \tag{2.1}$$

with $\dot{\gamma}^k(\mathbf{x})$, $\tau^k(\mathbf{x})$, and $\mathbf{m}^k(\mathbf{x})=\frac{1}{2}\left(\mathbf{n}^k(\mathbf{x})\otimes\mathbf{b}^k(\mathbf{x})+\mathbf{b}^k(\mathbf{x})\otimes\mathbf{n}^k(\mathbf{x})\right)$ being, respectively, the shear rate, the critical resolved shear stress, and the symmetric part of the Schmid tensor, associated with each slip system k of the K systems available, where $\mathbf{n}^k$ and $\mathbf{b}^k$ are the normal and Burgers vector direction of such slip system, $\dot{\gamma}_0$ is a reference rate, and n is the stress exponent.

If the shear rates $\dot{\gamma}^k(\mathbf{x})$ can be considered constant in a time increment Δt such that $\Delta\gamma^k(\mathbf{x}) = \dot{\gamma}^k(\mathbf{x})\Delta t$, the critical stresses of the deformation systems can be explicitly updated due to strain hardening. Here we use an extended Voce law [107], such that the evolution of the critical stress with accumulated shear strain in each grain is given by:

$$\tau^k(\mathbf{x}) = \tau_0^k + (\tau_1^k + \theta_1^k\Gamma(\mathbf{x}))(1 - \exp(-\Gamma(\mathbf{x}) \left|\theta_0^k/\tau_1^k\right|)) \tag{2.2}$$

where $\Gamma(\mathbf{x}) = \sum_{k=1}^{K} \gamma^k(\mathbf{x})$ is the total accumulated shear in the grain, and τ_0^k, τ_1^k, θ_0^k, and θ_1^k are the initial threshold stress, the initial hardening rate, the asymptotic hardening rate, and the back-extrapolated threshold stress, respectively.

2.2.2 DVP-FFT formulation

FFT-based formulations are spectral numerical methods to compute the local and effective response of heterogeneous materials, solving the governing equations inside a periodic unit cell that give an equilibrated stress field constitutively related to a compatible strain field. The heterogeneity of the unit cell may come from the presence of different isotropic phases, as in the case of composites, different grain orientations, as in the case of polycrystals, or a combination of both, i.e. multiphase polycrystalline materials. Porous polycrystals are a special case of the latter, in which one of the phases is the void phase, which cannot sustain stress. The starting point to combine crystal plasticity and dilatational effects has been the rigid-viscoplastic VP-FFT formulation [80, 81] for fully-dense polycrystalline aggregates with single crystals obeying the constitutive equation given in Equation 2.1. With the addition of voids, the latter incompressible formulation was extended [90], resulting in the DVP-FFT model to compute the instantaneous dilatational viscoplastic behavior of porous polycrystals. The addition of algorithms to account for void growth based on the use a Lagrangian grid of material points on top of the Eulerian computational regular grid where FFTs are performed [85], allowed extending DVP-FFT to predict porosity evolution in voided polycrystals, as well as porous materials with homogenous rigid-viscoplastic isotropic matrix [91]. The extension of the latter to consider porosity evolution in single crystals is straightforward, adopting the constitutive equation (Equation 2.1) for materials points belonging to the single crystal matrix.

We adopt the use of two grids: a Lagrangian grid of material points and an Eulerian computational grid. We generate the material points by first considering a regularly-spaced set of $2N_1 \times 2N_2 \times 2N_3$ voxels that discretize the unit cell and have single-crystal rigid-viscoplastic properties (Equation 2.1). These properties can be homogeneous throughout the entire unit cell (single crystal case) or periodically heterogeneous (polycrystal case). Next, we seed the void phase using certain criteria, as described in subsection 2.2.4, by removing the voxels occupied by the voids from the set of materials points. The points remaining in the material phase represent a set of material points denoted as $\{\mathbf{x}^{\mathbf{M}}\}$. Next, every other point of the regular grid along the three directions is identified as Fourier points, resulting in a $N_1 \times N_2 \times N_3$ computational grid, to be denoted $\{\mathbf{x}\}$. This Fourier grid in Cartesian space has a corresponding grid of the same size in Fourier space $\{\mathbf{k}\}$. When a strain rate $\dot{\mathbf{E}}$, or a stress $\boldsymbol{\Sigma}$, or a combination of both is applied to the unit cell, the local strain rate field is a function of the local velocity field, and can be split into its average and a fluctuation term:

$$\dot{\varepsilon}_{ij}\left(\mathbf{v}(\mathbf{x})\right) = \dot{E}_{ij} + \tilde{\dot{\varepsilon}}_{ij}\left(\tilde{\mathbf{v}}(\mathbf{x})\right) \tag{2.3}$$

where:

$$v_i(\mathbf{x}) = \dot{E}_{ij} x_j + \tilde{v}_i(\mathbf{x}) = V_i(\mathbf{x}) + \tilde{v}_i(\mathbf{x}) \tag{2.4}$$

The local constitutive relation between the strain rate and the stress for Fourier points with single crystal properties is given by Equation 2.1. The strain rate at these points has no dilatational component. As for the Fourier points belonging to voids, the stress vanishes. In FFT-based formulations, a fourth-order tensor $\mathbf{L}^{\mathrm{o}}$ is the stiffness of a linear reference medium, and the polarization field is given as:

$$\phi_{ij}(\mathbf{x}) = \tilde{\sigma}_{ij}(\mathbf{x}) - L^{o}_{ijkl}\tilde{\dot{\varepsilon}}_{kl}(\mathbf{x}) \tag{2.5}$$

such that the stress fluctuation is written as:

$$\tilde{\sigma}_{ij}(\mathbf{x}) = L^{o}_{ijkl}\tilde{\dot{\varepsilon}}_{kl}(\mathbf{x}) + \phi_{ij}(\mathbf{x}) \tag{2.6}$$

Combining Equation 2.6 with the equilibrium condition: $\sigma_{ij,j}(\mathbf{x})$=$\mathbf{0}$ and $\tilde{\dot{\varepsilon}}_{kl}(\mathbf{x})$=sym($\tilde{v}_{k,l}(\mathbf{x})$) gives:

$$L^{o}_{ijkl}\tilde{v}_{k,lj}(\mathbf{x}) + \phi_{ij,j}(\mathbf{x}) = \mathbf{0} \tag{2.7}$$

The differential equation whose solution is the Green's function G_{km} associated with the velocity field is then given by:

$$L^{o}_{ijkl}G_{km,lj}\left(\mathbf{x}-\mathbf{x}'\right) + \delta_{im}\delta\left(\mathbf{x}-\mathbf{x}'\right) = \mathbf{0} \tag{2.8}$$

where δ_{im} and $\delta(\mathbf{x})$ are the Kronecker and Dirac delta functions, respectively. The convolution integral that gives the velocity field is:

$$\tilde{v}_i(\mathbf{x}) = \int_{R^3} G_{ik,l}\left(\mathbf{x}-\mathbf{x}'\right)\phi_{kl}\left(\mathbf{x}'\right)\mathrm{d}\mathbf{x}' \tag{2.9}$$

Applying the convolution theorem, the velocity and velocity gradient fields in Fourier space are given by:

$$\hat{\tilde{v}}_i(\mathbf{k}) = (-ik_l)\,\hat{G}_{ik}(\mathbf{k})\,\hat{\phi}_{kl}(\mathbf{k}) \tag{2.10}$$

$$\hat{\tilde{v}}_{i,j}(\mathbf{k}) = \hat{\Gamma}_{ijkl}(\mathbf{k})\,\hat{\phi}_{kl}(\mathbf{k}) \tag{2.11}$$

where the symbol "^" indicates Fourier transform, and Γ_{ijkl}=$G_{ik,jl}$, which, using the definition of the Green's function, can be calculated in Fourier space as (see Lebensohn [80] for details on derivation):

$$\hat{G}_{ik}(\mathbf{k}) = A^{-1}_{ik}(\mathbf{k}), \text{ where: } A_{ik}(\mathbf{k}) = k_j k_l L^o_{ijkl}, \text{ and: } \hat{\Gamma}_{ijkl}(\mathbf{k}) = -k_j k_l \hat{G}_{ik}(\mathbf{k}) \tag{2.12}$$

Note that with $\hat{\Gamma}_{ijkl}(\mathbf{k})$ from Equation 2.12, and the current value of the polarization field in Fourier space, the symmetric part of Equation 2.11 gives the new guess of the strain-rate fluctuation field, which can then be antitransformed to obtain the associated new stress fluctuation field by evaluating the local constitutive equation. These updated guesses for the strain-rate and stress fluctuation fields can in turn be used in Equation 2.5 to update the polarization field, and so on and so forth.

From these equations, an iterative procedure based on the augmented Lagrangian algorithm [78] is adapted and adopted for the case of porous single crystals (this chapter), and polycrystals (see Lebensohn et al. [90]). The algorithm for a full stress tensor $\mathbf{\Sigma}$ imposed to the unit cell requires an initial guess (indicated by the iteration index (0)) for the average strain rate:

$$\dot{E}^{(0)}_{ij} = \dot{E}'^{(0)}_{ij} + \frac{\dot{E}^{(0)}_{kk}}{3}\delta_{ij} \tag{2.13}$$

that is then adjusted iteratively. Initial guess values also need to be assigned to the local strain rate field. The deviatoric and hydrostatic parts are adopted as:

$$\tilde{\dot{\varepsilon}}'^{(0)}_{ij}(\mathbf{x}) = \mathbf{0} \Rightarrow \dot{\varepsilon}'^{(0)}_{ij}(\mathbf{x}) = \dot{E}'^{(0)}_{ij} \tag{2.14}$$

$$\tilde{\dot{\varepsilon}}^{(0)}_{kk}(\mathbf{x}) = -\dot{E}^{(0)}_{kk} \Rightarrow \dot{\varepsilon}^{(0)}_{kk}(\mathbf{x}) = \mathbf{0} \tag{2.15}$$

With this initial guess for the strain rate field, the corresponding stress field in the material points $\sigma^{(0)}(\mathbf{x})$ can be obtained by inverting the local constitutive relation given by Equation 2.1. For those points belonging to voids, however, the stress simply vanishes. For the choice of the linear reference medium stiffness $\mathbf{L}^{\mathrm{o}}$, its deviatoric part can be obtained as an average over local stiffneses, e.g. the tangent stiffness based on $\sigma^{(0)}(\mathbf{x})$ for materials points and zero stiffness for void points, while the bulk modulus can be taken proportional to the norm of the deviatoric part and the initial porosity (see Lebensohn et al. [90, 91] for details).

These initial specifications provide a way to calculate an initial guess for the polarization field in direct space (Equation 2.5), which in turn is Fourier-transformed. Furthermore, assuming:

$$\lambda^{(0)}_{ij}(\mathbf{x}) = \sigma^{(0)}_{ij}(\mathbf{x}) \tag{2.16}$$

as the initial guess for an auxiliary stress field, the iterative procedure is as follows. With the polarization field after iteration i being known, the $(i+1)$-th iteration starts by computing the new guess for the kinematically-admissible strain rate fluctuation field:

$$\hat{\tilde{d}}^{(i+1)}_{ij}(\mathbf{k}) = -\hat{\Gamma}^{sym}_{ijkl}(\mathbf{k})\,\hat{\phi}^{(i)}_{kl}(\mathbf{k}), \quad \forall \mathbf{k} \neq \mathbf{0}; \quad and \quad \hat{\tilde{d}}^{(i+1)}_{ij}(\mathbf{0}) = \mathbf{0} \tag{2.17}$$

The corresponding field in real space is thus obtained by application of the inverse

FFT, and the new guess for the stress field in the single crystal material points is calculated from:

$$\sigma^{(i+1)}(\mathbf{x}) + \mathbf{L}^{\mathrm{o}} : \dot{\varepsilon}^{(i+1)}(\mathbf{x}) = \lambda^{(i)}(\mathbf{x}) + \mathbf{L}^{o} : \left(\dot{\mathbf{E}}^{(i)} + \tilde{\mathbf{d}}^{(i+1)}(\mathbf{x})\right) \tag{2.18}$$

which, combined with Equation 2.1, gives a 6×6 system of nonlinear algebraic equations to solve for $\sigma^{(i+1)}(\mathbf{x})$. The iteration is completed with the calculation of new guesses for the Lagrange multiplier field:

$$\lambda^{(i+1)}(\mathbf{x}) = \lambda^{(i)}(\mathbf{x}) + \mathbf{L}^{o} : \left(\tilde{\dot{\varepsilon}}^{(i+1)}(\mathbf{x}) - \tilde{\mathbf{d}}^{(i+1)}(\mathbf{x})\right) \tag{2.19}$$

and the new guess for the average strain rate:

$$\dot{\mathbf{E}}^{(i+1)} = \left\langle \dot{\varepsilon}^{(i)}(\mathbf{x}) \right\rangle + \mathbf{L}^{o^{-1}} : \left(\mathbf{\Sigma} - \left\langle \sigma^{(i+1)}(\mathbf{x}) \right\rangle\right) \tag{2.20}$$

where $\langle . \rangle$ indicates average over the entire Fourier grid. The algorithm then advances to the next iteration, until the stress fields and strain rate fields coincide within a threshold.

Upon convergence, the critical stresses of the Fourier points with single crystal properties can be explicitly updated according to the strain hardening law using Equation 2.2. The lattice rotation rate field can be also obtained (see Lebensohn et al. [91] for details). This field, if assumed constant over the time increment Δt used to march in time, can be integrated and used to update the crystallographic orientations associated with the points in the Fourier grid $\{\mathbf{x}\}$ with single crystal properties. Interpolation between $\{\mathbf{x}\}$ and the set of material points $\left\{\mathbf{x}^{M}\right\}$ (see Lebensohn et al. [91]) allow updating the critical stresses and crystallographic orientations of the latter, resulting in strain-hardening and texture evolution.

Equation 2.4 and the anti-transformation of Equation 2.10 give the time integration and interpolation of the velocity field mapped onto the Fourier grid. Together, they provide the local displacements of the material points, which scale with Δt. Under positive triaxialities, porosity increases and the aforementioned displacements are such that the material points move away from neighboring voids. This results in a local incompressible strain, dependent on the local single crystal plastic anisotropy and microstructure. The corresponding void growth accommodates the volume change imposed to the unit cell, which is given by $\dot{E}_{kk}\Delta t$. The new positions of the material points can be used as input of an algorithm (see Lebensohn et al. [91]) to reassign void properties to certain Fourier points (i.e. those whose distance to the nearest material point becomes higher than a threshold), which previously had material properties. This reassignment determines local void growth, and contributes to the overall porosity increase. As part of this algorithm, the time increment Δt can by controlled, such that the change in macroscopic porosity f given by $\Delta f = (1-f)\,\dot{E}_{kk}\Delta t$ (Tvergaard's formula [37]) coincides with the average of local porosity changes.

In this chapter, DVP-FFT simulations for two types of imposed loads are presented. The first one, used only in subsection 2.3.2 to precisely understand the influence of different loading types, is fully-imposed stress $\mathbf{\Sigma}$ (therefore also imposing stress triaxiality), which corresponds to the algorithm previously described. The other loading type used throughout the chapter is the one used by Ling et al. [2], in which the stress triaxiality is imposed (i.e. the ratio between stress components, but not the magnitude of stress itself) along with the longitudinal component of the strain-rate. The latter loading type requires a correction to the stress tensor applied to the unit cell, based on the consideration of the homogeneity of degree n of the strain-rate response to a given applied stress, explained as follows. For a porous material with single crystal or polycrystal matrix, whose local material behavior is given by Equation 2.1, if $\dot{E}^{(1)}$ is a scalar measure (e.g. longitudinal component) of the strain rate response to a stress tensor $\mathbf{\Sigma}^{(1)}$ applied to the unit cell,

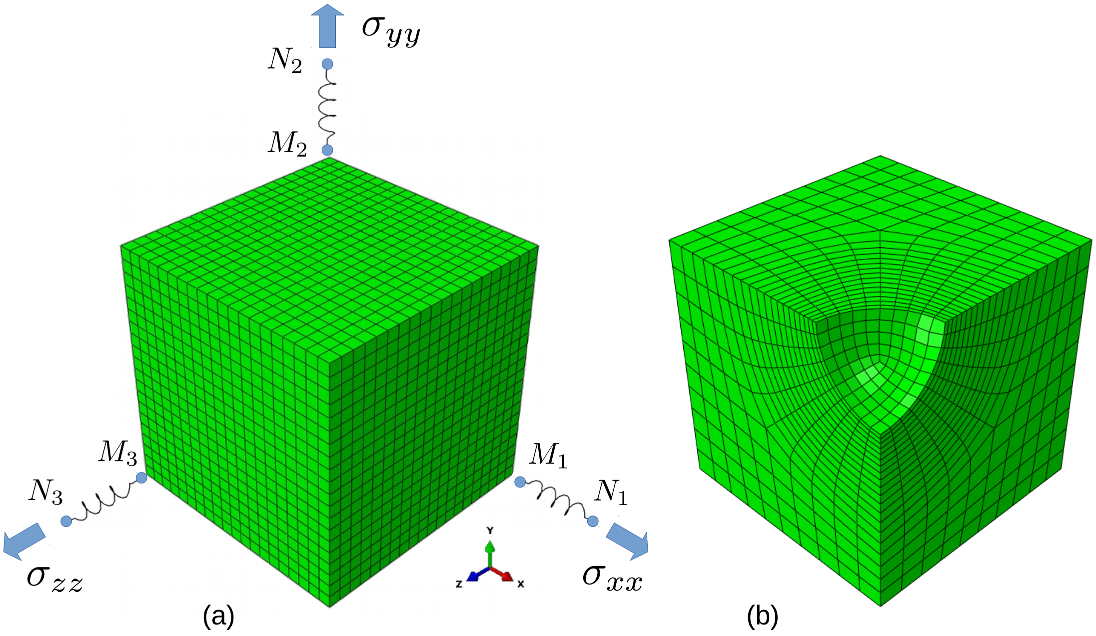

Figure 2.1: (a) Finite element setup for strain-rate and stress-triaxiality controlled loading of the porous unit cells containing a central cavity and composed of Abaqus C3D8 brick elements. Axial strain rate is imposed by displacement of node N_3, while the stress triaxiality and the axisymmetric stress condition are controlled by the displacements of node N_1 and N_2 in Equations 2.26 and 2.27 (Abaqus nodal MPC). (b) One eighth of the unit cell highlighting the central cavity (f=0.01).

then the imposed stress can be corrected according to $\mathbf{\Sigma}^{(2)}=\left(\dot{E}^{(2)}/\dot{E}^{(1)}\right)^{1/n}\mathbf{\Sigma}^{(1)}$ to obtain a strain rate response with $\dot{E}^{(2)}$ longitudinal component.

2.2.3 FEM formulation

The finite element model of the voided single crystal problem consists of a FE mesh of a periodic unit cell with a void in the center (Figure 2.1) and a single crystal plasticity subroutine [108, 109] to compute the constitutive response at the level of the FE integration points, within the framework of an Abaqus-Implicit solver.

The control of both strain rate and stress triaxiality is achieved in the FE model by the use of dummy nodes connected by linear springs outside of the unit cell for the control of boundary conditions (Figure 2.1.a), as inspired from the work of Lecarme et al. [110]. The FE mesh of the cuboidal single crystal unit cell is periodic, in the sense that the node coordinates on each opposite outer surfaces are related by a translation. Periodic boundary conditions are applied by coupling the displacement degrees of freedom (DOF) of node pairs that face each other through the displacement of the master nodes M_1, M_2 and M_3 in Figure 2.1.

Assuming an axisymmetric stress state with z as the primary loading direction and using the definitions of the mean (hydrostatic) stress σ_H and the Von Mises equivalent stress σ_{eq}, the stress triaxiality $T=\frac{\sigma_H}{\sigma_{eq}}$ reduces to:

$$T = \frac{2\sigma_{xx} + \sigma_{zz}}{3(\sigma_{zz} - \sigma_{xx})} \tag{2.21}$$

which can be re-arranged to express σ_{xx} as a function of the primary stress σ_{zz}:

$$\sigma_{xx} = \sigma_{zz}\frac{3T-1}{3T+2} \tag{2.22}$$

The forces exerted on the faces of the unit cell by the springs (with identical stiffness K) is written:

$$F_x = K(u_x^{N_1} - u_x^{M_1}), \quad F_y = K(u_y^{N_2} - u_y^{M_2}), \quad F_z = K(u_z^{N_3} - u_z^{M_3}) \tag{2.23}$$

The instantaneous area of the faces of the unit cells can be written as a function of the initial edge length L_0 of the unit cell and the displacement of the master nodes M_1,

M_2, and M_3 shown in Figure 2.1:

$$\begin{aligned} S_x &= (L_0 + u_y^{M_2})(L_0 + u_z^{M_3}) \\ S_y &= (L_0 + u_x^{M_1})(L_0 + u_z^{M_3}) \\ S_z &= (L_0 + u_y^{M_2})(L_0 + u_x^{M_1}) \end{aligned} \tag{2.24}$$

from which the instantaneous (true) stress components can be written as:

$$\sigma_{xx} = \tfrac{F_x}{S_x}, \quad \sigma_{yy} = \tfrac{F_y}{S_y}, \quad \sigma_{zz} = \tfrac{F_z}{S_z} \tag{2.25}$$

To satisfy the stress triaxiality constraint of Equation 2.22, Equations 2.23, 2.24, and 2.25 can be combined and inserted into Equation 2.22 to yield the following expression of $u_x^{N_1}$:

$$u_x^{N_1} = u_x^{M_1} + B\frac{(L_0 + u_z^{M_3})(u_z^{N_3} - u_z^{M_3})}{L_0 + u_x^{M_1}} \tag{2.26}$$

where B stands for $\frac{3T-1}{3T+2}$.

Moreover, when the axisymmetric stress state condition, σ_{xx}=σ_{yy}, is satisfied, the following expression of $u_y^{N_2}$ results:

$$u_y^{N_2} = u_y^{M_2} + \frac{(L_0 + u_x^{M_1})(u_x^{N_1} - u_x^{M_1})}{L_0 + u_y^{M_2}} \tag{2.27}$$

While $u_z^{N_3}$ is prescribed to achieve the desired axial strain-rate of the unit cell, Equations 2.26 and 2.27 are solved iteratively using an Abaqus Multi-Point Constraint (nodal MPC), coded as a Fortran user subroutine.

The crystal plasticity constitutive behavior is computed with a user subroutine, which is summarized below (see [108, 109] for more details). The stress developed in the crystals at each integration point is obtained based on the multiplicative decomposition of the deformation gradient tensor $\mathbf{F}$=$\mathbf{R}^*\mathbf{U}^{\mathbf{el}}\mathbf{F}^{\mathbf{p}}$, where $\mathbf{R}^*$ is the lattice rotation, $\mathbf{U}^{\mathbf{el}}$=$\mathbf{1}$+ϵ is an infinitesimal elastic stretch, and $\mathbf{F^p}$ is the result of dislocation slip (plastic deformation). The velocity gradient tensor $\mathbf{L}$ is:

$$\mathbf{L} = \dot{\mathbf{F}}\mathbf{F^{-1}} \simeq \dot{\mathbf{R}}^{*}\mathbf{R}^{*\mathbf{T}} + \mathbf{R}^{*}\left(\dot{\epsilon} + \mathbf{L^p}\right)\mathbf{R}^{*\mathbf{T}} \tag{2.28}$$

where

$$\mathbf{L^p} = \dot{\mathbf{F^p}}\mathbf{F^{p-1}} = \sum_{\mathbf{k}} (\mathbf{b^k} \otimes \mathbf{n^k})\dot{\gamma}^{\mathbf{k}} \tag{2.29}$$

The slip rate $\dot{\gamma}^k$ on slip system k and the hardening rule for the critical resolved shear stress τ^k are calculated as detailed in subsection 2.2.1. The elastic part of the strain rate $\dot{\epsilon}$ is related to the elastic stiffness tensor and the time-derivative of the second Piola-Kirchhof stress computed in the intermediate configuration. Lattice rotation $\mathbf{R}^*$ is calculated by the time-integration of the skew-symmetric part of the velocity gradient $\mathbf{L}$ (Equation 2.28). Time integration is fully implicit based on a Newton-Raphson scheme.

In summary, the FFT-based and FE crystal plasticity formulations at the material points are similar, but differ by the consideration of a (relatively small, compared with the viscoplastic part) elastic contribution to the total deformation in the CP-FE approach, which is neglected in DVP-FFT computations. Moreover, the adopted CP-FE is based on large-strain kinematics (Equations 2.28 and 2.29), while DVP-FFT microstructure (including porosity evolution) is based on the combined use of a Lagrangian set of material points and an Eulerian computational grid, as described in the previous sub-section.

2.2.4 Simulations designed to probe orientation dependence

In this section, we describe the different simulations conducted to determine the effect of crystal orientation on void growth employing the DVP-FFT and CP-FE formulations. Three groups of microstructures were employed to probe the orientation dependence of intracrystalline void growth under axisymmetric tension: one group of single crystal simulations, and two groups of polycrystalline simulations, shown in Figure 2.2. All simulations employed a set of 72 predetermined orientations of the crystal axes with respect to the tensile axis: 45 orientations originally introduced by Lebensohn et al. [111], and 27 additional orientations to cover the intermediate regions of orientation space between the [100], [101], and [111] orientations, shown in Figure 2.2b. These 27 orientations are not as evenly spaced as the original 45 orientations, but they cover the missing regions without duplication. These selected orientations are presented in an inverse pole figure/stereographic triangle relative to the z-direction, i.e. the axis of the largest principal stress in our simulations.

The first set of simulations conducted using DVP-FFT and CP-FE considers single crystalline unit cells. CP-FE is used here to compare to DVP-FFT and verify its results in simple cases. For the majority of simulations that follow, the DVP-FFT is employed because of its computational efficiency and that it is a much easier way to discretize and treat complex structures. In the DVP-FFT simulations, 72 individual voided single crystals were created and the corresponding unit cells were discretized with 128×128×128 material points (minus those in the void region), corresponding to a Fourier grid size of 64 in each direction, with the void at the center of the simulation, occupying 1% of the volume of the initial crystal. The selected percentage permitted a sufficient amount of observable voxel points and grid refinement (i.e., we had spherical voids) without initiating significant void-to-void interaction. The difference between the grid employed in this chapter and that of a finer one are approximately 3% in axial stress and less than 1% in void fraction and void fraction growth rate. Each single crystalline unit cell had an orientation corresponding to one of the 72 orientations described above. Of the 72 unit cells, four single crystal orientations were compared against corresponding CP-FE simulations: [100], [101], [111], and [210] orientations. The CP-FE single crystal unit

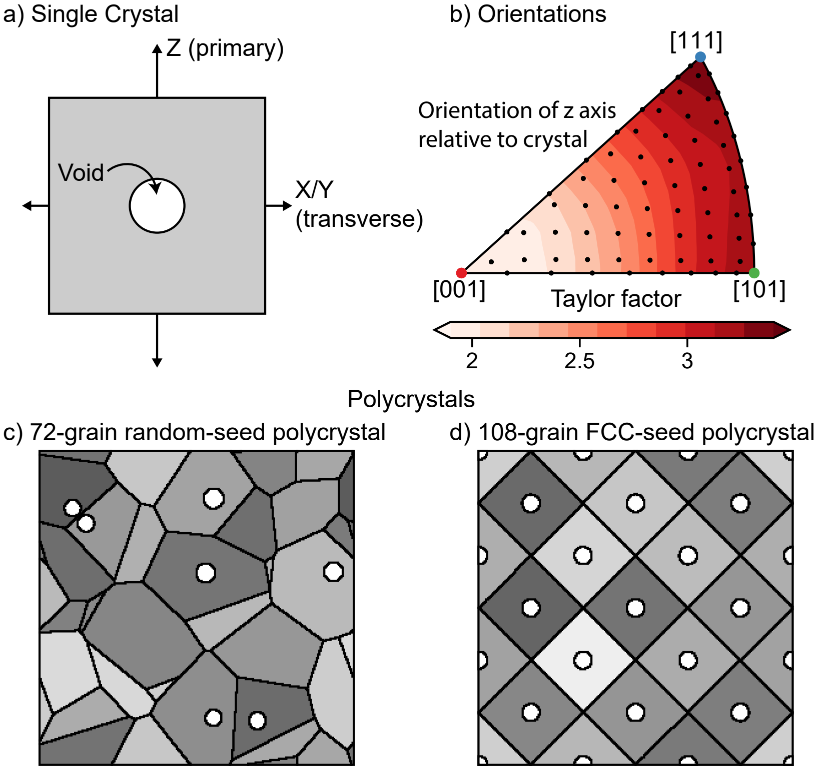

Figure 2.2: Figures of the three 3-dimensional microstructure sets used in the simulations: (a) a periodic single crystal with a void in the interior, with a primary stress in the Z direction; (b) the 72 key crystal orientations used in the simulations (as dots), and are colored with the Taylor Factor of the fully dense material calculated for a n=5; and (c) and (d) are the two polycrystalline microstructures. Sub-figure (c) is a 2-D slice through the random 72-grain voronoi tesselation with voids at the seed of each of the Voronoi cells. Sub-figure (d) shows a 2D slice through the plane of the 108-void system, in which the voids are placed in an FCC-like array and the grains form the Wigner-Seitz cells around each void. The center of the grain and the center of the void coincide in this regular grid, and the grains form dodecahedrons, consistent with a coordination number of 12. In each case, the boundary conditions are the same as in (a), with the primary axis is in the Z direction.

cells were composed of 16000 Abaqus C3D8 brick elements (eight nodes, eight integration points). Convergence of the CP-FE results was checked with respect to the number and type of finite elements used to mesh the unit cell. The chosen orientations also allowed qualitative comparison with previously reported CP-FE simulations by Ling et al. [2].

Besides voided single crystals, we studied polycrystalline microstructures with intragranular voids as well, in order to access nearest grain neighborhood effects. Two sets of polycrystalline microstructures were simulated using DVP-FFT. Both types were composed of 256×256×256 material points before removing those from the voids, corresponding to 128×128×128 Fourier points. The first microstructure was a 72-grain unit cell, with the grains randomly-generated by periodic Voronoi tessellation. Voids were located at the seed points of the Voronoi structure, and occupied 1% of that grain's volume, i.e. larger grains contained larger voids. 72 random orientations were assigned to the grains. The same 72-grain partition was used in different realizations to maintain the same morphology, while the orientations assigned to each grain were randomly reassigned, for a total of 30 realizations.

The second type of polycrystalline microstructures, and the third microstructure group, was created by placing the center of the voids in an FCC-type super-lattice (i.e. regular arrangement of grains, not of atoms), and forming the grains around them, using their Wigner-Seitz cells. This placement ensured that all voids were at the center of the grains, and that all voids were identical in shape and size, reducing the variables to the individual grains orientation and neighborhood. However, because the microstructures needed to have four (for one FCC unit cell) voids, and power-of-three numbers of FCC super-cells are convenient, 108 voided grains were created (4×36). The 72 orientations were randomly assigned to 72 of the 108 grains, and the remaining 36 grains were randomly assigned 36 random orientations. As before, these 108 orientations were randomly assigned in 30 separate realizations.

All simulations were stress-triaxiality controlled and of these, most were additionally strain-rate controlled, while a small group of six simulations were instead stress-controlled (reasons to be discussed shortly). The applied strain rate in strain-rate controlled simulations was $\dot{\varepsilon}^{p}_{eq}$=1.0 s^{-1} in the DVP-FFT, and $\dot{\varepsilon}^{p}_{33}$=1.0 s^{-1} in the FEA. Each microstructure was simulated using DVP-FFT at four stress triaxialities: T_X=0.6, 1, 2, and 3, with the primary axis along the z-direction, and axisymmetric stresses in the x and y-directions. FEM simulations are presented at two of those four triaxialities: T_X=0.6 and 3. Not all of the results are presented, given that the intermediate triaxialities were found to represent intermediate states between the lowest and highest triaxialities.

A set of single-crystal simulations at the highest and lowest stress triaxiality but with fully-prescribed equivalent stress of σ_{eq}=2.5τ_0 were additionally conducted with DVP-FFT. Only the [100], [101], and [111] single crystal orientations were simulated. These simulations are discussed in subsection 2.3.2.

The crystals were able to plastically deform activating the 12 $\langle 110\rangle$ $\{111\}$ slip systems associated with FCC slip. The reference slip rate and stress exponent in Equation 2.1, are $\dot{\gamma}_0$=1.0 and n=5, respectively. The Voce hardening parameters from the Equation 2.2 were τ_0=1.0 MPa, τ_1=3.0 MPa, θ_0=8.0 MPa, and θ_1=0.0 MPa. Additionally, in the FEM calculations, isotropic elastic coefficients were assumed: C_{11} = 1346 MPa, C_{12} = 577 MPa and C_{44} = 385 MPa, resulting in a Young's modulus more than 1000 times larger than τ_0.

2.3 Results & Discussion

2.3.1 Voids in single crystals, comparisons between CP-FE and DVP-FFT

To ascertain that the CP-FE and DVP-FFT models show the same void growth trends, single crystal simulations were compared for the highest and lowest triaxialities (T_X=0.6 and T_X=3). Figure 2.3 shows the normalized void volume, V/V_0; remote stress, σ_{33}/τ_0; and transverse plastic strain, ε_T^p, as a function of plastic strain in the axial direction, ε_{33}^p at the lowest triaxiality. The stresses and transverse strains are within 10% of each other at strains above 0.2 for the lower triaxiality simulations. The volume fraction of the voids, except for voids in the [101]-oriented crystals, differ by less than 10% at all strains. The voids in the [101]-oriented crystals differ by less than 10% up to strains of 0.5, and then increase to 25% by 100% axial strain.

The DVP-FFT and CP-FE at the higher triaxiality do not match as closely, as shown in Figure 2.4. The trends are consistent for the transverse strains, at least from the perspective of the ordering of the crystal orientations. The trends in growth rate, the focus of the current study, are consistent. Figure 2.4(c-d) shows that the transverse strains calculated by FFT and FEA differ significantly initially, by 2.5 times, but then eventually converge at higher plastic strains. At low strains, the transverse strains are going to be primarily due to the elastic strain contribution in the CP-FE. This large strain difference is also likely due to the difference in prescribed strain rate, since the specific strain rate prescribed in each method differs slightly ($\dot{E}_{eq}$ in the DVP-FFT and $\dot{E}_{33}$ in the CP-FE). The stress and volume fraction are within 20% between the corresponding CP-FE and DVP-FFT simulations. At both triaxialities, the void in the [111]-oriented crystal grows the fastest, while the void in the [101]-oriented crystal at the lower triaxiality and in

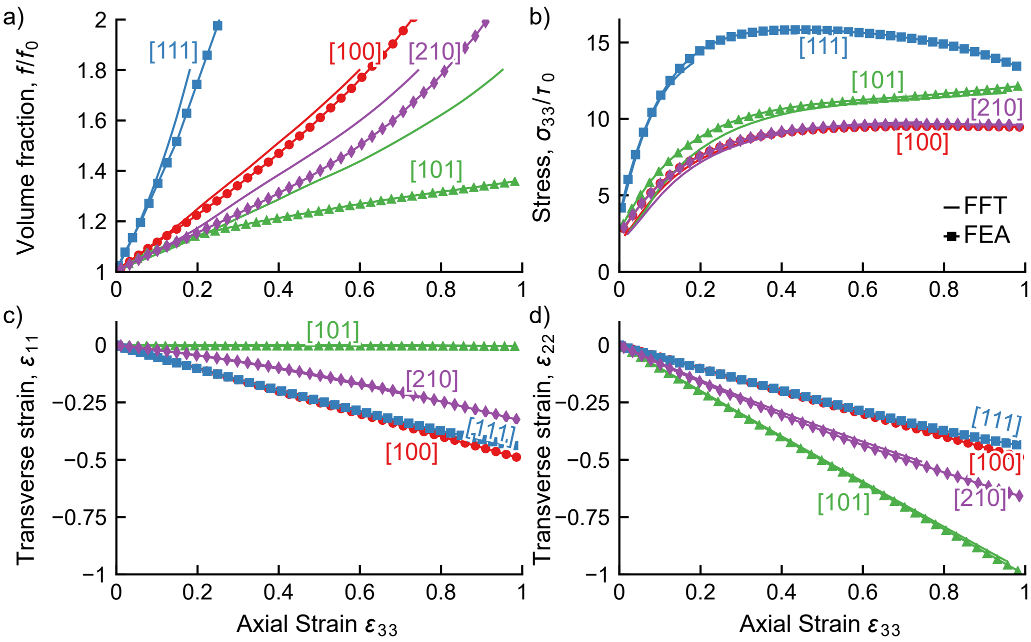

Figure 2.3: Figures comparing DVP-FFT (no symbols) and CP-FE (closed symbols) in single crystals at a low triaxiality (T_X=0.6). The figure (a) shows the volume fraction of the void, (b) axial stress, (c) transverse strains in the x direction, and (d) transverse strains in the y direction. The (b) stresses and (c, d) transverse strains in the material (to what extent the DVP-FFT completed) are within 10% of one another at strains above 20%, and the trends for the (a) volume fraction and, by extension, volume fraction rate, are consistent. At this low triaxiality, the voids in [111] and [101]-oriented crystals grow at the highest and lowest rate, respectively.

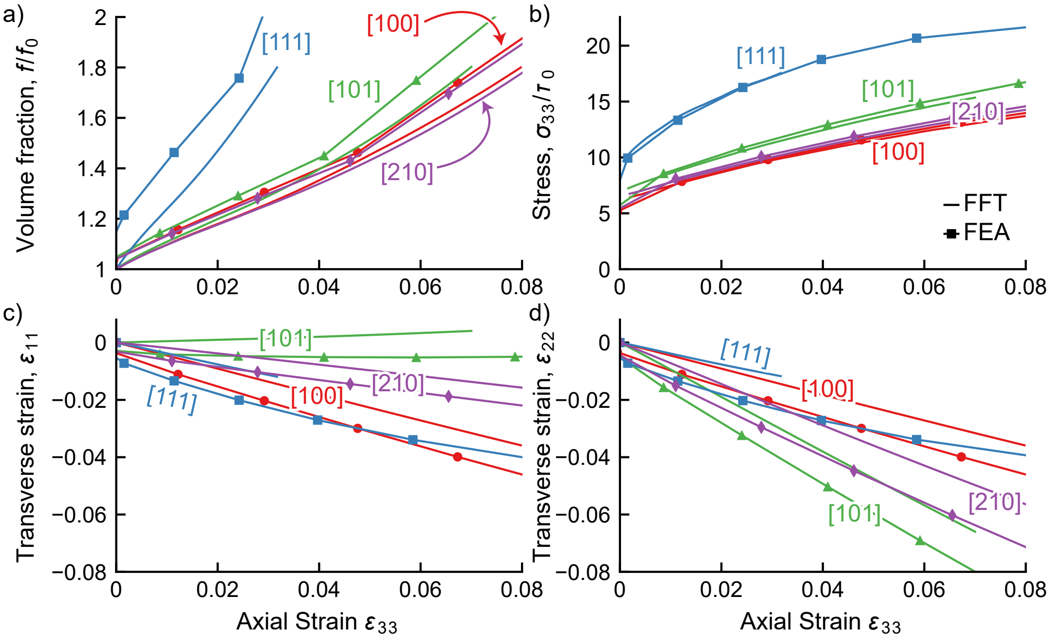

Figure 2.4: Figures comparing DVP-FFT (no symbols) and CP-FE (closed symbols) in single crystals at a high triaxiality (T_X=3). The figure (a) shows the volume fraction of the void, (b) axial stress, (c) in the x direction, and (d) transverse strains in the y direction. The DVP-FFT calculations complete a fraction of what the CP-FE completes. (a) The volume fractions are within 20% of each other between simulation types, and stresses differ by no more than 15% for each crystal orientation. Here, the (c, d) transverse strains differ significantly, but (a) both algorithms predict that the voids in the [100]-oriented grains grow the slowest, rather than the [101] grains. Both algorithms predict that the voids in the [111]-oriented grain grow fastest.

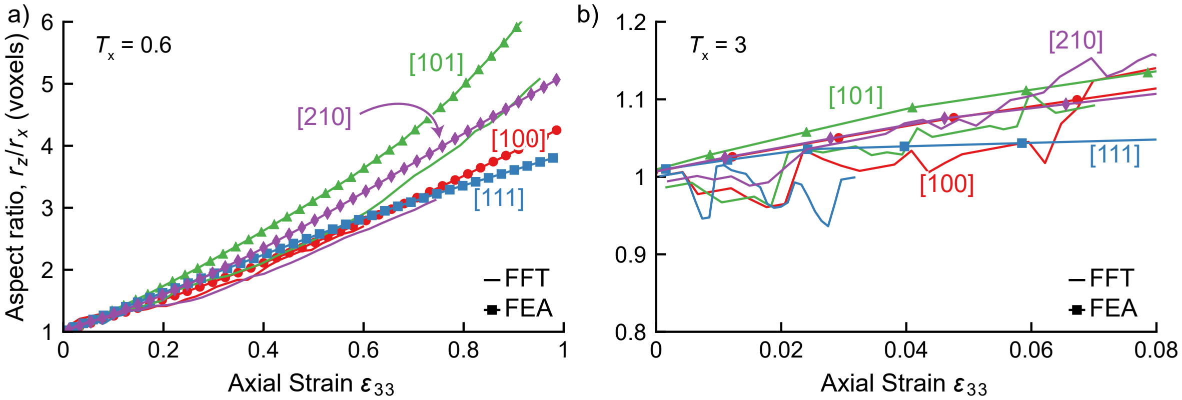

Figure 2.5: Figures showing aspect ratios vs. the plastic macroscopic axial strain for both the DVP-FFT (no symbols) and CP-FE (closed symbols) in single crystals at (a) a low triaxiality (T_X=0.6) and (b) a high triaxiality (T_X=3). At both triaxialities, the DVP-FFT aspect ratio algorithm yielded more noise than that of the CP-FE. The aspect ratio of the voids in the (b) high triaxiality case in the DVP-FFT simulations exhibited significant noise, but both aspect ratios remain within 10% of the original value during the range shown.

the [100]-oriented crystal at higher triaxialities grows at the lowest rate. The DVP-FFT algorithm does not control the total axial strain, so the simulations at higher triaxialities use a much smaller time scale and maximum axial strain, to control the strain rate most accurately. Figure 2.3.1 shows the aspect ratio, AR, as a function of plastic strain in the axial direction, ε_{33}^{p} at the lowest and highest triaxialities. The data contain some noise, since the post-processing aspect-ratio algorithm can encounter problems when the shape of the voids does not change significantly. At the higher triaxiality, with the least shape change, the noise is greatest, making comparison between the models difficult. Nonetheless, we clearly find that the aspect ratio at that triaxiality are within 20% between the corresponding CP-FE and DVP-FFT simulations. The Ling et al. [2] CP-FE results indicate the same trends in the cases of the [100], [101], and [100]-oriented crystals, but the void in the [210]-oriented crystals grew at a slower rate at both triaxialities reported [2], although they have a higher exponent (n=15) and the hardening rule differs. Other CP-FE simulations, such as those by Asim et al. [73] and Chen et al.

[51] also show that soft grains appear to have faster void growth.

In summary, voids in FCC single crystals grow most rapidly in [111]-oriented crystals under strain-rate controlled conditions. This orientation corresponds to plastically hard crystal relative to the loading direction. This is consistent across DVP-FFT and CP-FE, although slight variations between the two models exist, due to the fact that the CP-FE relies on a mesh and large-strain kinematics, while the DVP-FFT uses voxelized microstructures, as well as lacks the elastic behavior of the CP-FE. Because of the choice of a void volume fraction to both maximize observation and minimize interaction between voids, the trends seen here are expected to hold at lower porosity levels. This important conclusion of this comparison is that DVP-FFT yields comparable results with CP-FE and we can therefore rely on the more efficient DVP-FFT to investigate the relationship between crystal orientation and triaxiality on void growth with reliable statistics in polycrystals.

2.3.2 Voids in single crystals

The loading type dictate the void growth rate, as seen in Figure 2.6, which shows the results of DVP-FFT simulations for voided single crystals with orientations [100], [101], and [111] with two sets of loading types: fully-stress controlled, and axial strain-rate controlled. In both cases, the stress triaxiality is controlled. When volume is plotted against strain, the void in the hard [111]-oriented crystal always grows at the highest rate. This trend was obtained for all strain-rate controlled simulations, but in the softest [100]-oriented crystals, porosity always grows the fastest in *time* with fully-imposed stress. When stress is fully imposed, the intermediate [101] orientation has the slowest void growth in time. Thus, depending on the local loading conditions, the apparent speed of void growth may reverse, which may account for experimental observations that voids

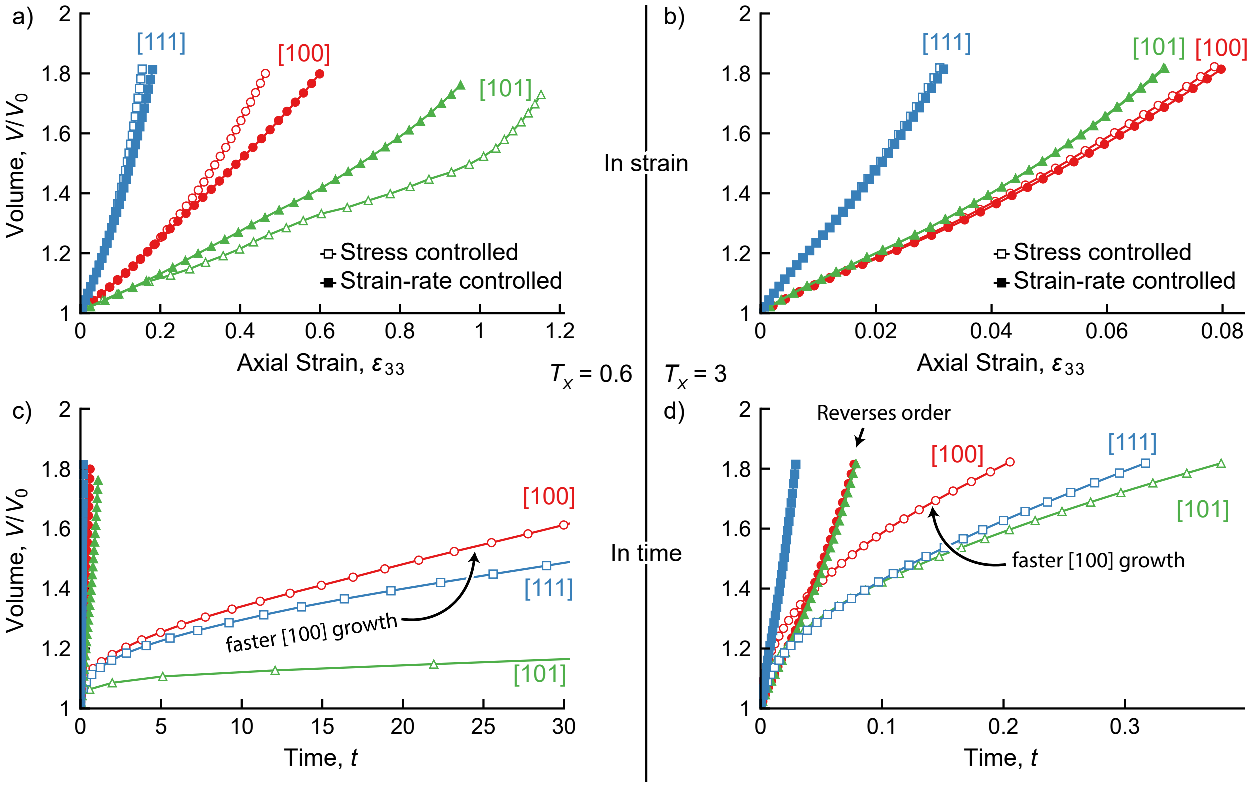

Figure 2.6: Volume vs. axial strain and volume vs. time plots for voids in single crystal voids in the DVP-FFT simulations at T_x=0.6 and T_x=3 show that loading types can reverse the order of growth rate in the single crystals. Under stress-controlled loading, the softest crystals grew fastest in *time*.

are largest in soft grains [7].

Figure 2.7 shows the inverse pole figure (IPF) with a contour of the initial void growth rate with respect to strain for each single-crystal orientation represented in the IPF. Overall, the void growth rate in single crystals varies smoothly between any two of the three symmetric orientations ([100], [101], and [111]). The voids in all crystals experience an initial reduction, followed by an increase in growth rate as the simulations progress (click here for supplemental animation).

The calculations are repeated for a range of triaxialities, although not all are shown. For all triaxialities tested, the voids in [111]-oriented crystals grow the fastest with respect to strain. They continue to grow at the fastest rate for the entire straining period, including the initial reduction in growth rate. At low triaxialities, voids in [101]-oriented crystals grow the slowest, while at higher triaxialities, voids in [001]-oriented crystals grow the fastest, as is evident in figures 2.3 and 2.4. The arrow drawn in Figure 2.7 illustrates the connection from the crystal orientation with the slowest-growing void to the orientation with the most rapidly growing void and approximately follows the path of the steepest gradient.

2.3.3 Voids in polycrystals

Next, we study void growth in fully voided polycrystals, in which every crystal has one starting intragranular void. In the 72-grain random structure, we expect that orientation effects on void growth to be highly variable and weak, in which much of the strong orientation effects on void growth seen in the isolated single crystals are diminished.

In the 72-grain random case, each void has a different size and location in its parent crystal. In the 108-regular polycrystal, each void is the same size and centered inside its parent. The chief variable lies in the orientation of the surrounding grain neighbors. Voids

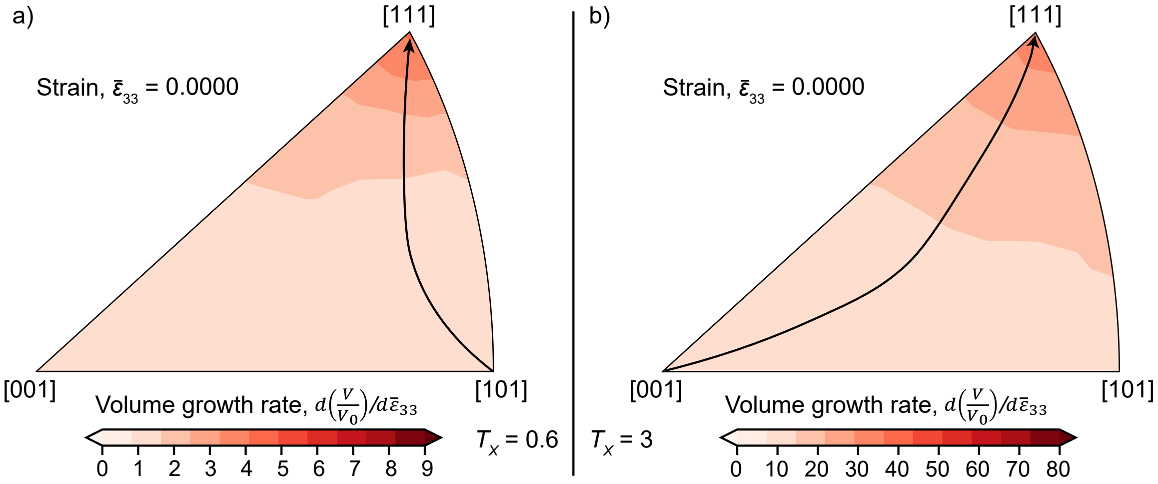

Figure 2.7: Initial volume growth rate (taken as the derivative of volume in terms of macroscopic axial plastic strain) as a function of orientation for single crystals at stress triaxiality (a) T_x=0.6 and (b) T_x=3. Each of the 72 points shown in Figure 2.2b is represented here by one individual simulation. The voids in the [111]-oriented single crystals grow fastest. At low triaxialities, the void in the [101]-oriented single crystal grows the slowest, while at higher triaxialities the void in the [100]-oriented crystal grows the slowest. The arrows are drawn to indicate the trend of fastest rate change, highlighting this shift between low and high triaxialities. The indicated trend was not numerically determined. Find link in body of text to download animation.

in all neighboring grains grow at different rates and interact with one another. With these many sources of variation, we expect void growth across the polycrystal to be distributed. The question, however, concerns whether orientation effects on intragranular void growth seen in ideal single crystal tests are still preserved in a multiply-voided polycrystal.

Figure 2.8 shows IPF contour plots for polycrystals with the random 72-grain structure and the regular 108-grain structure. The IPFs represent the average of 30 realizations at the same macrostrain, plotted as a function of void growth rate with respect to strain vs. the crystal orientation containing each void. Since in the 72-grain polycrystal, each void is not the same size, the void volume was first normalized by its starting volume before averaging. Note that each point represents one of the 72 starting orientations. The additional randomly-generated orientations that supplemented the 108-grain polycrystal are not included in these plots to reduce clutter.

The strong correlation between orientation and void growth rate seen in the single crystals is diminished in the case of polycrystals, although the growth rate near the [111]-direction still remains consistently the highest for all triaxialities. At the lower triaxiality, both polycrystalline microstructures have a few other orientations with exceptionally high growth rates. In the random 72-grain polycrystals, these orientations are [327]-, [438]-, and [538], and in the regular 108-grain polycrystal, they are [219]- and [214]. At the higher triaxialities, the orientations with the highest growth rates are still exclusively the [111]-oriented crystals.

For both the single crystals and polycrystals, the growth rate varies non-monotonically with strain in a way that does not depend on its starting orientation. An animated version of Figure 2.8 can be downloaded by clicking here. For voids in all single crystals, the growth rate varied in the same way, initially decreasing and then increasing with strain. The voids in the polycrystalline microstructures are not similar. In any individual simulation, the voids in some grains grow the fastest initially, only to slow down and be surpassed by other voids in grains with a different orientation.

To compare orientation effects with the single crystal cases, Figure 2.9 compares the volume of voids in selected starting orientations in the single crystals and the *average* volume of the voids in the corresponding crystal orientations in the polycrystalline microstructures.

The void growth in [111] grains in the polycrystals is, on average, slower than that of its single crystal counterpart. However, the orientation correlates more closely to growth at the highest triaxiality than for the lowest triaxiality, as is indicated in the Figure 2.8. It is possible that at even higher triaxialities, the voids in the [111]-oriented crystals in polycrystals would experience even greater growth.

In the 72-grain random polycrystals, for T_X=3, the voids in both the [111]- and [001]-oriented grains initially grow at similar rates to their single crystal counterpart. As the strain increases, the voids in the [001]-oriented grains in polycrystals appear to grow faster. Conversely, the voids in the [111]-oriented grains in polycrystals slow down as strain increases. This indicates that the [111] grains have reached a saturation stress, and that the [001] and [101] crystals continue to grow and compensate for this saturation. Overall, voids in [001]-oriented grains loaded with low stress triaxialities appear to grow faster, on average, in polycrystals than in a single crystal with the same orientation.

The voids loaded at low stress triaxialities appear to be the least sensitive to orientation in the 72-grain random polycrystal: the voids in the [111]-oriented grains grow at a similar average rate as the voids in the [001]-oriented grain. At high triaxialities, the voids grow faster in the [111] grains. Overall, the [101]-voids grew the slowest at all triaxialities.

The voids in the [001] grains have the most erratic behavior, having slow initial growth for T_X=1, but more moderate growth at the other triaxialities. The growth decreases to a minimum for T_X=1, and then increases towards its single crystal behavior for T_X=3.

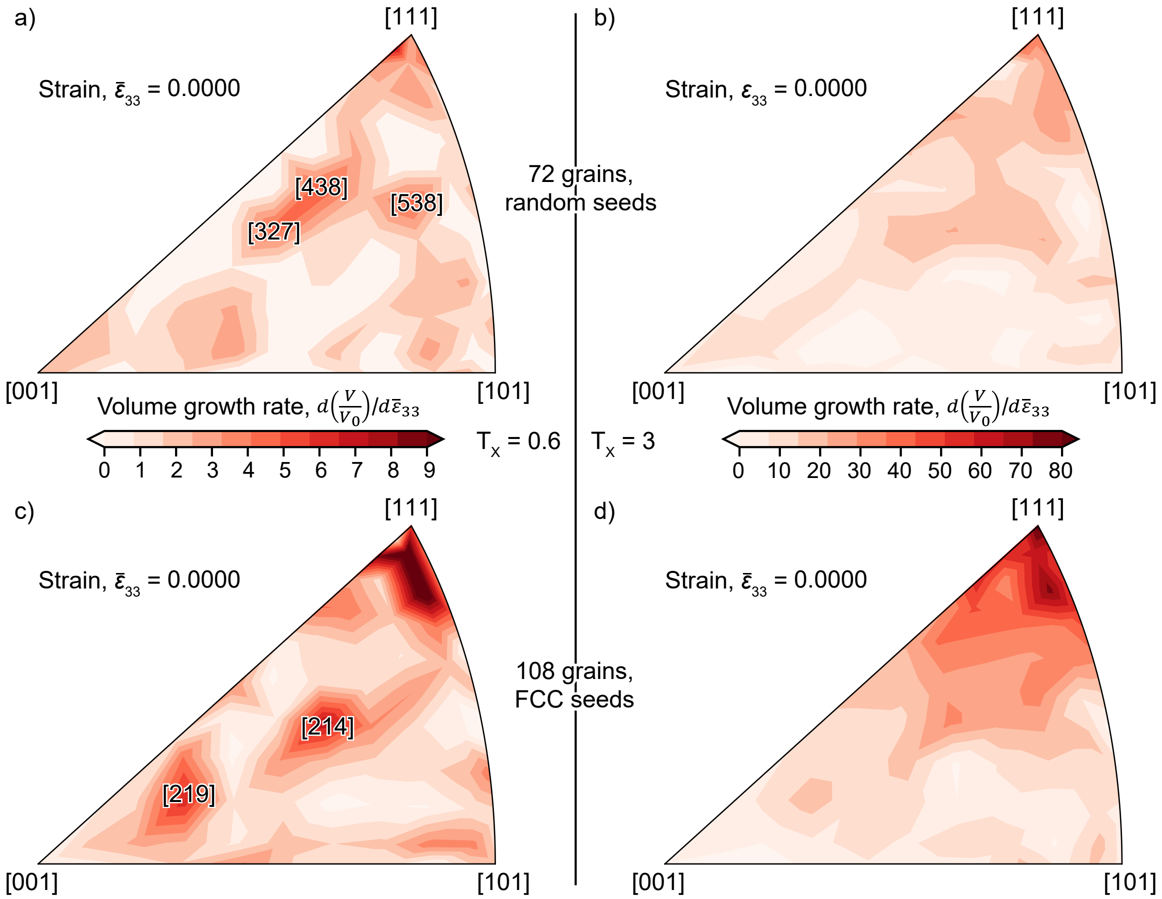

Figure 2.8: Initial volume growth rate (couched in terms of macroscopic axial plastic strain) as a function of orientation for polycrystals in the 72-grain polycrystal at a stress triaxiality of (a) T_x=0.6 and (b) T_x=3, and in the regular 108-grain polycrystal at a triaxiality of at a stress triaxiality of (c) T_x=0.6 and (d) T_x=3. The figures shown here represent the average of 30 realizations of polycrystals, plotted as a function of void growth rate vs. containing crystal orientation (relative to the primary stress axis). Each of the 72 points shown in Figure 2.2b is represented here by the average of 30 simulations. The results are noisier than in single crystals, although voids grow consistently faster in grains oriented near the [111]-direction. The still does not capture the non-monotonic growth rate of the voids. Find link in body of text to download animation.

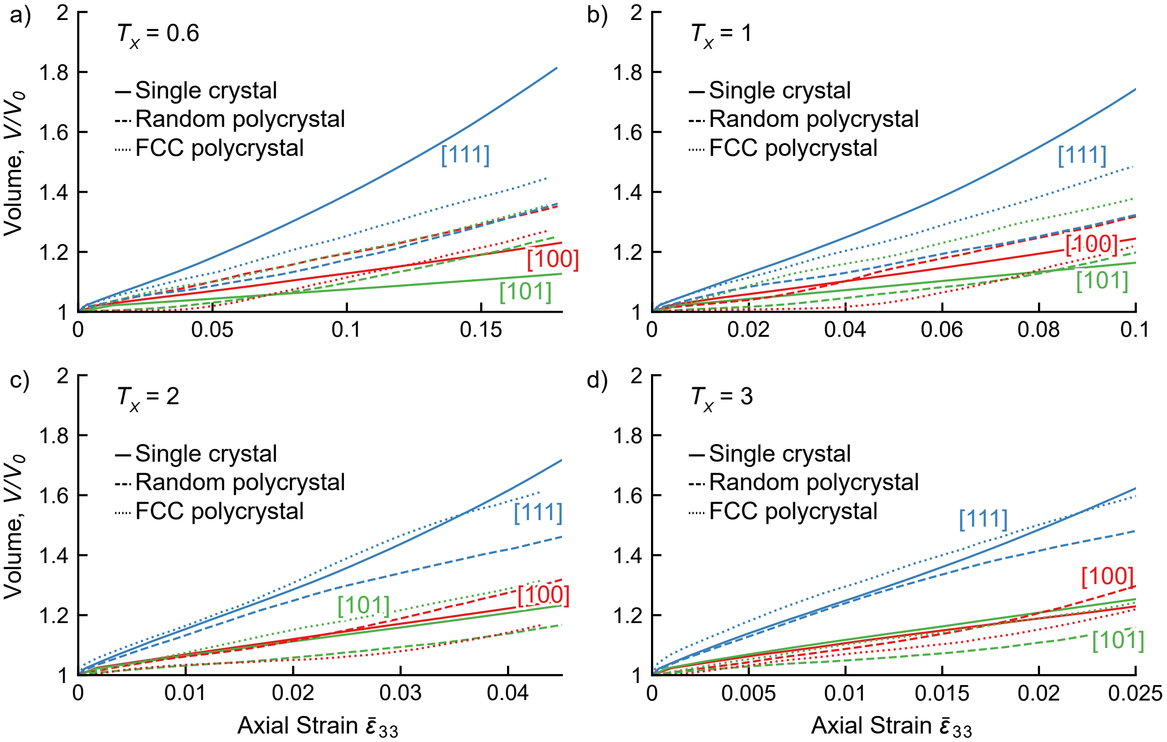

Figure 2.9: Volume vs. axial strain plot for the corners of the stereographic figures, showing data analogous to the previous figures, for stress triaxialities (a) T_x=0.6, (b) T_x =1, (c) T_x =2, and (d) T_x =3. At every triaxiality, the void in a [111]-oriented single crystal grew the fastest. At low triaxialities, the void in the [101]-single crystal grew the slowest, but at higher triaxialities, the voids in the [001]-oriented crystals grow the slowest.

On average, these voids grow slower than their single-crystal (and, by extension, the 72-grain polycrystal). The voids in [101] grains grow faster in this ordered polycrystal at every triaxiality compared to the random polycrystal, but converges to the single crystal value at the highest triaxiality.

Based on observations from Lebensohn et al. [90], it has been proposed that the relationship between the parent orientation and growth rate seen in single crystals would reverse in polycrystals. It was seen in that work that the interconnecting material between two nearby voids experienced an increased plastic strain rate if the material was soft, such as an [001]-oriented grain. Accordingly, here, we would expect to see that while the voids in [111]-oriented crystals grow the fastest, the voids in the same orientations in polycrystal would grow the slowest. This appears to be the case at low triaxialities (T_X=0.6) but not at high triaxialities (T_X=3). The results here demonstrate that despite the interaction between two neighboring growing voids, at high triaxialities, the hardest crystals (i.e., [111]-oriented ones) continued to experience the most void growth.

Taken together the results on the fully voided polycrystals show that intragranular void growth is insensitive to orientations at low triaxiality and very sensitive to orientations at high triaxiality. The strong propensity for growth in [111]-oriented crystals is reduced in polycrystals. Particularly at lower triaxialities, the material behaves more isotropically; that is, void growth is insensitive to parent orientation. In contrast, void growth correlates clearly with crystallography at high triaxialities. Like the single crystals, the parent orientations in the polycrystal that are not near the [111] orientation show reduced growth rates at higher triaxialities. The only exceptions to this are when the parent orientations have much lower growth rates than those of its immediate surrounding orientations.

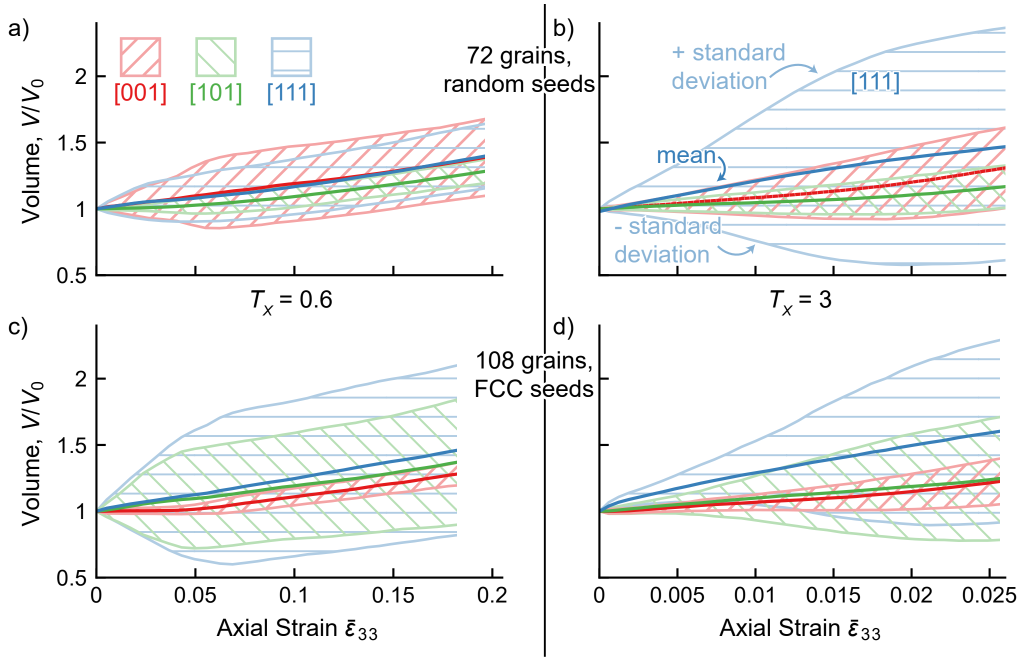

Figure 2.10: These figures show the mean (bold line) and one standard deviation bounds of void volume as a function of axial strain for the 72-grain polycrystal at a stress triaxiality of (a) T_x=0.6 and (b) T_x=3, and in the regular 108-grain polycrystal at a triaxiality of at a stress triaxiality of (c) T_x=0.6 and (d) T_x=3. What is most important to note is that the mean of the three directions falls within the standard deviation lines in every case. Note that the [111] case does have the greatest standard deviation in figures (b) and (c).

2.3.4 Data spread and statistical significance

Figure 2.10 shows the mean void volume and one standard deviation away in the [111]-, [101]-, and [001]-oriented crystals in Figure 2.8. The mean of each void tends to fall within the standard deviation of all three void types. The range of volume change is wide in polycrystals, bringing into question whether the number of realizations is sufficiently large to state that this variation is statistically significant. Yet, to date, to our knowledge, no report in the literature has completed such a study for polycrystals. Therefore, there is a need to take a closer look at the statistical significance of the differences in the obtained distributions and on the effect of grain neighborhood.

To determine the statistical significance of porosity distributions, the two-tailed p-value is determined for void volume at the same axial plastic strain between voids in [111]-, [101]-, and [001]-oriented crystals, using the mean and standard deviation from Figure 2.10. When the p-value is close to unity, the two distributions are nearly identical. Any differences between the mean likely originate from rare cases or outliers. The low triaxiality simulation for the random polycrystal shown in the top left-hand corner in Figure 2.11 is one example. This is not the case at high triaxialities, wherein the void in the hardest crystal continued to experience the most growth.

When the value is close to zero (below the standard 5% threshold), the populations are statistically distinct from one another and any differences cannot be attributed to randomness. For instance, the p-value is less than 0.05 between the voids in [111]-oriented grains and both other grain orientations for the high triaxiality case in the regular 108-grain polycrystal. In other words, the voids in the [111]-oriented grains have void growth patterns that are distinct from the voids in both [101]- and [001]-oriented grains. The orientations of the parent grains are likely the primary cause of the faster void growth.

The other cases have intermediate p-values, well above the standard 5% threshold. At the lower triaxiality, and between the voids in [101]- and [001]-oriented grains at all triaxialities, the differences between the other two void populations are not statistically distinct. We suspect that in these cases, the faster void growth in the [101]-oriented grains is due more in part to the grain neighborhood than to the parent grain orientation.

2.3.5 Neighborhood effects

The spread in data in Figure 2.8 poses two important questions: to what extent is the spread due to neighborhood, and how is void growth affected by the Taylor Factor of the grains around the main grain that surrounds each void? To this end, a set of nine microstructures were designed to understand how longer-range average geometric

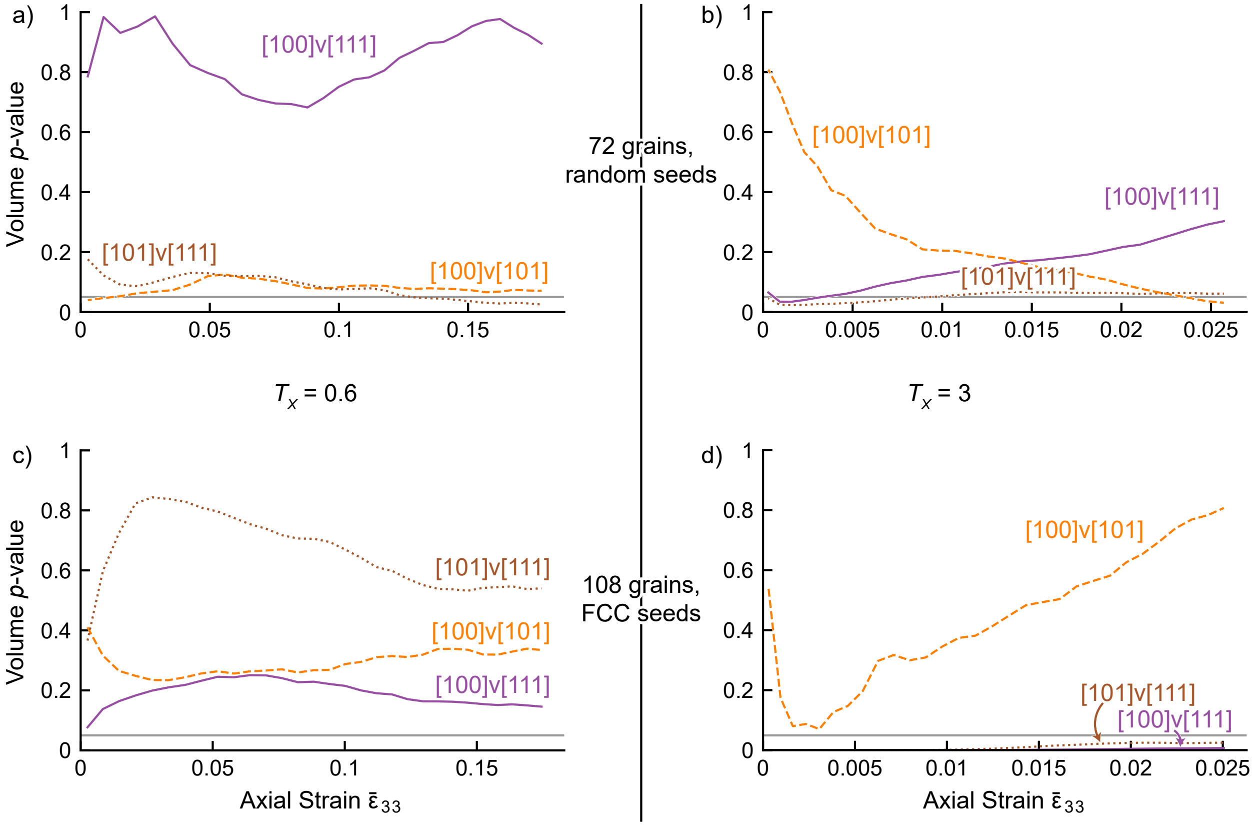

Figure 2.11: p-value plots based on the previous plots in Figure 2.10, of the distribution of the void volume in the 72-grain polycrystal at a stress triaxiality of (a) T_x=0.6 and (b) T_x=3, and in the regular 108-grain polycrystal at a triaxiality of at a stress triaxiality of (c) T_x=0.6 and (d) T_x=3. The orientations listed in the plot indicate the two grain populations compared. If a line is labeled, for example, [100]v[111], each value compares the distribution of void volumes between voids in grains in [100]-oriented grains and [111] oriented grains at each axial strain. Note that only the voids in the [111] are below a threshold of $\alpha < 0.05$ (which is a typical value) in figure (d), indicating that the [111] population is distinct from the [100] and [101]-oriented populations.

hardness of the neighborhood affects the growth of the voids. These microstructures were created from existing microstructures to cover the possible extremes of the material. Each of these microstructures changed one of two aspects: either the hardness of the grain orientation containing a void or the average hardness of all the nearest neighboring grains of a central grain. These populations are called interior grains and neighborhood grains, respectively, and in each case, only the growth of the void in the interior grain is tracked. Three interior grain orientations were chosen: soft, medium, and hard, shown as brown, green, and purple dots in Figure 2.12(b). For the neighborhood microstructures, three distinct microstructures among the 30 108-grain microstructures were randomly selected. The interior grain of interest was not touching the edges of the unit cell. The 12 neighbors were reassigned orientations lying in a similar location in orientation space, equally classified as either hard, med or soft, different from central grain. Figure 2.12 shows an example where the interior grain has a medium-hardness orientation, and the neighborhoods are either soft, medium, or hard, represented by the brown, *orange*, and purple grains, respectively. The other grains outside of this neighborhood retained their originally assigned orientations.

Figure 2.13 shows the strain evolution of the void growth in the central grain of each microstructure. Regardless of neighborhood, the hard interior grains have the fastest growth rate. For the same interior grain orientation, we observe that grains with hard neighborhoods grow faster than those with softer neighborhoods. At low triaxiality, the hardest level of the interior grain has less influence on void growth rate. We observe that both neighborhood and interior grain hardness level affect void growth rates, such that a medium hard interior grain with a medium neighborhood could grow slower than a soft interior grain with a hard neighborhood. This result identifies neighborhood as one source for the weakening influence of orientation on void growth within a polycrystal. At higher triaxiality, the effect of orientations can be more easily identified, wherein hard interior

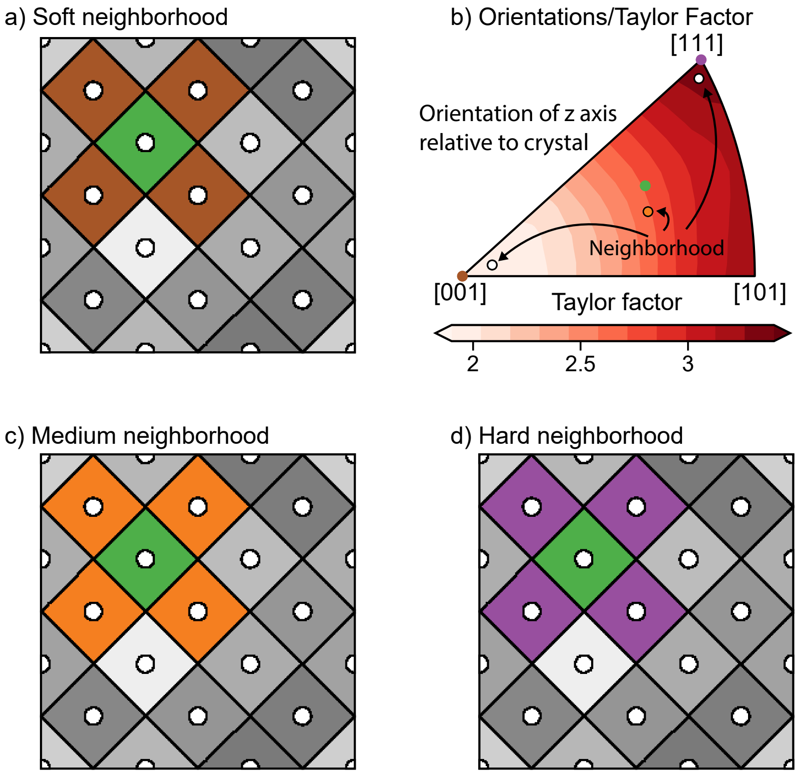

Figure 2.12: Simulations setup (a,c,d) for three of 9 of the neighborhood simulations, showing a medium interior grain (green), with a (a) soft, (c) medium, and (d) hard neighborhood. Note that there are 12 nearest neighbors in the 3D microstructure, and the medium orientation of the neighbors is not identical to the medium interior. Corresponding orientations can be seen in (b), where the additional outlined dots nearby the [100] and [111] orientation represent the orientations of the neighborhood when the interior grain has the closest orientation. In this case, the orange is closest to the green interior dot.

grains or hard neighborhoods would tend to increase growth rates. The apparent lack of growth, seen particularly in the soft grain with a soft neighborhood in Figure 2.13(b), is likely due to growth below the resolution of the voxelized Fourier grid. Faster growing grains are contributing to the macroscopic void growth, and thus the algorithm does not need to add additional void voxels to the Fourier grid. In Figure 2.13(c,d), we show the associated axial stresses versus strain curves. In all cases, the higher stresses generated in harder grains results in faster intragranular void growth rates. Neighborhood effects on stress states are not as influential as the orientation of the interior grain.

Grain neighborhoods likely made a difference in this analysis because changing 12 of the 108 grains can change the macroscopic stress. However, no major change in macroscopic stress occurred when the same orientations are simply reoriented, as in the original cases in subsection 2.3.3. However, we reveal a notable dependence of void growth on parent orientation. This implies that it is important to account for crystal orientation, particularly when the material is strongly textured or if stress concentrations tend to develop preferentially in particular orientations. Grain stress and its neighborhood Taylor factor are not strongly correlated at any triaxiality, but grain stress and its own Taylor factor is. Figure 2.14 shows the initial void growth speed of the void vs. the initial average grain stress for the original 30 108-grain simulations conducted, where each dot represents one grain in one of the 30 simulations and is colored by the Taylor factor of the grain. Again, we observe a correlation between the grain stress and its Taylor Factor at higher triaxiality, but not at low triaxiality.

The apparent insensitivity of growth rate to parent orientation seen in the lower triaxiality case was not seen in the single crystals and not seen in the polycrystal at high triaxiality. This difference points to a strong neighborhood effect. Considering that the orientation plays a smaller role when approaching hydrostatic loading, this trend is unexpected. One possibility is that the load in the grains is sufficiently directional,

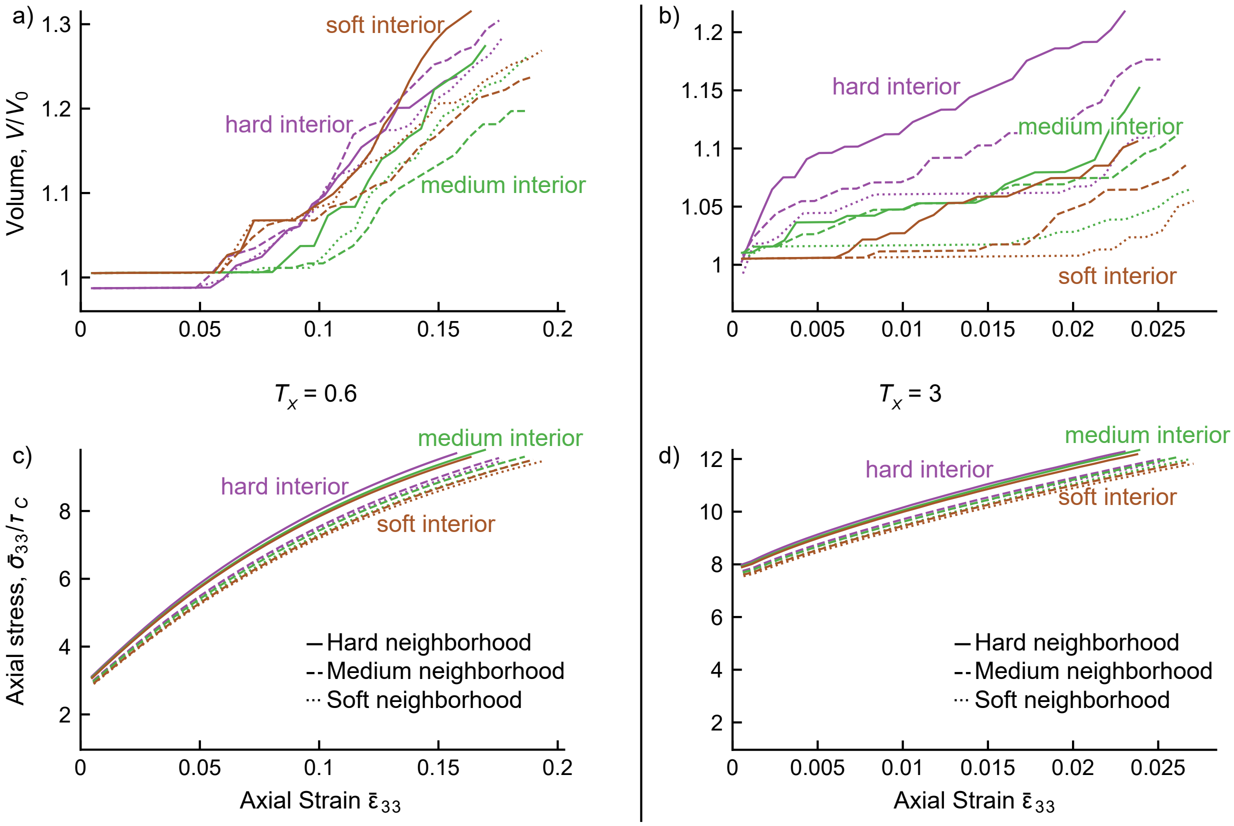

Figure 2.13: Volume vs. strain (a,b) and macroscopic stress vs. strain (c,d) plots of voids in the regular polycrystals at two triaxialities (a,c) T_x=0.6 and (b,d) T_x=3, where the voids are inside a hard, medium, or soft grain (purple, green, and brown, as labeled as the interior grain), where the grains nearest neighbors are all hard, medium, or soft (solid, dashed, or dotted). These plots correspond to microstructures detailed in Figure 2.12. The plots reveal that the hardest grains (and interiors) have the most void growth.

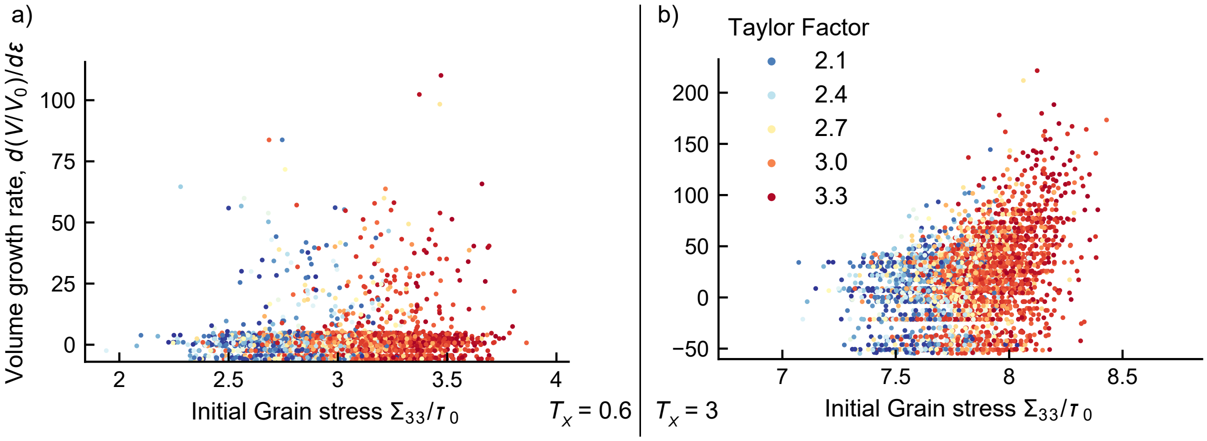

Figure 2.14: Initial void growth velocity vs. stress (with dots colored by Taylor factor) for all 30 realizations of the regular FCC super-lattice grain structure with 108 grains at stress triaxialities of (a)T_x=0.6 and (b) 3. The figures indicate that grain stress correlates with Taylor Factor, but only at the higher triaxiality is there any appreciable increase in void growth velocity with grain stress.

but the neighborhood behavior approaches an isotropic medium, reducing the neighborhood effect, and in consequence allowing the anisotropic response of each grain. On the other hand, when the grain is loaded in nearly uniaxial tension, the anisotropy of the neighborhood is amplified, which in turn may shield individual grains.

The relevance and novelty of the work in this chapter, in terms of unraveling the dependence of intragranular void growth with microstructural (e.g. grain orientation and grain neighborhood effects) and mechanical features (e.g. triaxiality), should be considered in connection with recent state-of-art in-situ characterization experiments, as well as a potential guidance for the design of forthcoming experiments of this kind. In-situ characterization of damage in engineering alloys, like the void-tracking experiments based on 3-D X-ray micro-tomography, mentioned in the introduction as motivation for the present study [96, 97], revealed a significant dispersion of void growth, qualitatively consistent with our results. However, a more quantitative comparison and cross-validation between experiments and predictions would require not one but two simultaneous in-situ characterization methods to identify void's and grain's spatial locations, as well as grain orientations. Recent multi-modal experiments with this level of fidelity have been reported in the literature, but not necessarily for the in-situ characterization of engineering alloys fabricated using standard processing techniques. For example, Lieberman et al. [112] pre-characterized ex-situ the local orientation field using 3-D High-Energy Diffraction Microscopy (HEDM) in a high-purity copper sample. The sample was then incipiently spalled and post-characterized in terms of its void distribution, providing confirmation of damage occurred primarily by voids forming at grain boundaries. With this data, the post-mortem correlation between voids, grain orientations and grain boundary types was subsequently analyzed using FFT-based methods. Pokharel et al. [113] used tomography and orientation mapping to study a 2-phase metal-metal composite, in which damage mainly occurs by debonding between phases. Naragani et al. [114] used similar characterization techniques to study damage/orientation correlations, including at the void coalescence stage, in an additively manufactured Ni superalloy, in which relatively large voids (with respect to the grain size) were printed, i.e. pre-seeded in the microstructure. These recent multi-modal experiments demonstrate that these state-of-the-art techniques are mature enough to deliver data to contrast with our model results. The predictions reported in this chapter should be provide guidance to experimentalists on where to look next.

Specifically, we envision that, depending on the loading conditions, the texture could affect the macroscopic behavior of the material, but at a microscopic level, the voids behave as if they were in a more isotropic medium. That is to say, in low-triaxialtiy simulations, we found no strong isotropy in polycrystals, where single crystal behavior differs more significantly. At higher triaxialities (and more dynamic loads), the opposite would be thus expected: macroscopically, the material would behave more isotropically, but the voids would grow heterogeneously on average, i.e. fastest/slowest in the hardest-oriented grains for displacement-rate/load controlled experiments, which could cause different coalescence behavior and thus failure. As there are no such experiments yet available that directly compared the void growth rate in polycrystals, our results suggest the design of new experiments in engineering materials to look into the average growth rate of voids of various orientations, for cross-validation with the model predictions.

2.4 Conclusions

In this chapter, using a dilatational visco-plasticity fast Fourier transform-based model, we investigated crystallographic orientation effects on the growth of intragranular voids. Without the effects of void nucleation and coalescence, three sets of simulations with different crystalline microstructures were conducted, and the orientations of the grains in these microstructures were varied over the full orientation space. The first type of microstructures were single crystals, the second type, Voronoi polycrystals where every grain had one void in its interior, and the third type, another voided polycrystal where the void centers were the centers of a FCC super-lattice with 12 nearest neighbors, and the grains filled the Wigner-Seitz cells surrounding them. In each case, the initial void volume fraction per grain is 1%. A set of 72 orientations were tested for the single crystal, and those same 72 orientations were applied to 30 random realizations of both of types of polycrystals, so that the neighborhood (and, in the case of the random polycrystal, the grain morphology) was different in each realization. Each of these microstructures were simulated at four axisymmetric triaxialities, to determine if triaxiality had an effect on the void growth. For some select cases, DVP-FFT and CP-FE models were conducted on nearly the same microstructures. The comparison demonstrated that DVP-FFT yields comparable results with CP-FE.

The trends are clear in single crystals; the voids in the [111]-oriented grains, that is in the hardest grain, grow the fastest in strain-rate-controlled simulations. At lower triaxialities, the void growth rate is slower overall, and the voids in the [101]-oriented grains grow the slowest. At higher triaxialities, the void growth is much more rapid, and the slowest growing void is the void in the [101]-oriented grain. In simulations where the stress was fully prescribed, the slowest growing voids were the [101]-oriented grains, and the softest grain had the fastest voids growth. The void growth rate with respect to strain is identical to the constant-strain-rate simulations.

In polycrystals, not only the grain orientation, but also the nearest grain neighborhood plays a large role in dictating the void growth, especially at lower triaxialities. At higher triaxialities, most notably in the regular polycrystal, the single crystal trend become more apparent and the voids in the [111]-oriented grains grow the fastest on average.

In the case of the polycrystals, it was unexpected that the fastest growing void is the intragranular void in the hardest grain. This outcome contradicted previous observations for a different configuration (i.e. intergranular porosity) that the voids would grow the fastest in the softest grain, given that soft single-crystal ligaments between intergranular voids in polycrystals can deform at higher strain rate under the same stress [90]. The expectation was that by surrounding the void with a soft material in a heterogeneous polycrystal, the soft material would deform plastically the fastest. This would result in faster void growth, since dilatational plasticity models are predicated on the idea that the deformation of the surrounding material determines void growth. The findings of the work in this chapter suggest that crystal orientation has a significant influence on the growth of voids it contains. They imply that crystal orientation needs to be considered in the response of polycrystalline materials, particularly those that have texture or in which local stress concentrations preferentially develop in certain orientations.

This study did not identify any clear trends in the role of the neighborhood in the growth of voids, neither due to void neighborhood hardness nor hardness disparity, but did suggest that neighborhood can affect the void growth if it increases or decreases the stress of the grain, particularly at high triaxialities. In addition, it would appear that the neighborhood plays a strong role in reducing the expected anisotropic behavior at low triaxialities. It appears, also, that at higher triaxialities, the neighborhood does not play as strong a role, because grain stress, Taylor factor, and void growth rate correlate more strongly. Determining to what extent the neighborhood plays a role would be an interesting and important study in the future. Given that, for example, in high-purity metals voids typically form at grain boundaries and junctions, it is also imperative to study the effect of growth at grain boundaries and triple junctions, as the neighborhood effects are expected to play a more complex role.

The polycrystalline results indicate a discrepancy in isotropic behavior between macroscopic and microscopic properties, pointing to trends that might be observable in future experiments. In low-triaxiality simulations, the texture is expected to dominate the macroscopic properties, but not the void growth rate in randomly-textured samples. At higher triaxialities, while the sample might behave more isotropically, the voids may grow at different rates in relation to containing grain's crystal orientation. New in-situ experiments on engineering materials may need to track void growth of intragranular voids and compare the void growth rate at different triaxialities and with different loading conditions.

Chapter 3

LS-EVP-FFT and modifications

3.1 Motivation for use of LS-EVP-FFT

The previous chapter discusses the growth of voids as implemented in a dilatational-viscoplastic (DVP) fast-Fourier transform (FFT) based algorithm. This model takes advantage of the use of two grids to simulate the growth of voids while ensuring that the grid remains regular and rectangular. The use of the two grids and the defining of the voids on a regular, rectangular grid has some disadvantages. Firstly, at the end of each time increment, the void volume fraction of the regular Fourier grid must be updated using the nonregular material grid. The use of two grids without a one-to-one mapping reduces the efficiency of the algorithm. Second, the growth of voids on the Fourier grid is achieved by replacing one or more voxels with crystalline properties with void voxels. Because at least one void voxel must be added to the Fourier grid each step, there is a discrete minimum by which the void must grow. This promotes discontinuous growth. Finally, the discretization of the spherical void on a rectangular grid creates a stair-step pattern, most notably at the points in the void that are closest to the corners of the simulation cell. This stair-step pattern, in turn, introduces noise at the void-material interface. While the effect of elastic anisotropy is not explored within this thesis, an additional limitation to the DVP-FFT model is that it does not include elasticity. As a result, the effects of elastic anisotropy and, more importantly, strain gradient plasticity on void growth cannot be studied using this model.

These issues have been resolved in a recently-developed large-strain (LS) elasto-viscoplastic (EVP) FFT model (abbreviated here as LS-EVP-FFT) developed by Zecevic et al. [89], and is used in the remainder of this thesis for void simulations. The next section presents relevant details of the original LS-EVP-FFT formulation of Zecevic et al. [89] and the modifications that allow predicting void growth in multicrystals with intergranular voids. Section 3.3 describes the simulation cases used to verify the model and compare it with CP-FEA and DVP-FFT, and section 3.4 shows the results of these verification simulations. Within section 3.4, subsection 3.4.1 compares LS-EVP-FFT predictions with analytical results for Eshelby's inclusion, and subsection 3.4.2 presents comparisons with CP-FE simulations for intragranular voids in single crystals. Subsection 3.4.3 presents predictions of void growth in single crystals under axisymmetric tension, with various crystal orientations aligned with the major tensile axis, from DVP-FFT and LS-EVP-FFT. Finally, section 3.5 summarizes the results and defines terms that will be used in the next two chapters.

3.2 LS-EVP-FFT basics

The void growth calculations reported here were performed adapting the LS-EVP-FFT model developed by Zecevic et al. [89] to account for the presence of initially spherical cavities. The LS-EVP-FFT formulation allows for the use of an irregular grid of material points to model finite elasto-plastic deformation of crystalline materials. Compared to the DVP-FFT formulation introduced by Lebensohn et al. [90], and used to simulate void growth by Christodoulou et al. [115], the geometry of spherical (or ellipsoidal) voids and grain boundaries can be accurately represented, which is critical for the type of study carried out in this work. Moreover, the formulation includes elasticity, and, while in this work we model isotropically elastic materials, elastic anisotropy could be easily accounted for.

The reader is pointed to the work published by Zecevic et al. [89] for a full description of the LS-EVP-FFT model. Here, we provide a summary of the key elements of the formulation in subsections 3.2.1 and 3.2.2, followed by a description of modifications to the algorithm to improve the numerical stability when a phase with zero stiffness (the void) is present in subsection 3.2.3. In terms of the adopted notation, first-order tensors (vectors) are written in boldface, while scalars, second- and fourth-order tensors are italic and not bold. Capitalized X_i and lowercase x_i are position vectors of a material point in the reference and current configurations, respectively. A hat over a field, $\hat{\cdot}$, denotes a Fourier transform of the field, $\langle\cdot\rangle$ denotes its volume average, and a tilde over a field, $\tilde{\cdot}$, denotes fluctuation of the field with respect to its mean value: $\tilde{v}{=}v{-}\langle v\rangle$.

3.2.1 Summary of LS-EVP-FFT prior to modifications

All simulations presented here correspond to periodic unit cells originally discretized by means of a regular rectangular grid of $N_1{\times}N_2{\times}N_3$ points with position vector $\mathbf{X}$. This regular *reference configuration* is transformed into the *initial configuration* using a stress-free displacement field, $\mathbf{u}^{\mathrm{c}}(\mathbf{X})$, where "c" stands for conformal, to reproduce the initial, possibly complex, internal geometry of the unit cell. A conformal deformation gradient field, $F^{\mathrm{c}}(\mathbf{X}){=}I{+}\partial\mathbf{u}^{\mathrm{c}}/\partial\mathbf{X}$, where I is the second-order identity tensor, results from the applied conformal displacement field.

When the boundary conditions are applied to the initial unit cell, the initial grid of material points is evolved into a new current configuration using a Lagrangian description, in discrete time increments Δt.

The large-strain formulation consists of a multiplicative decomposition of the total deformation gradient, F,

$$F_{il} = F^{\mathrm{e}}_{ij} F^{\mathrm{p}}_{jk} F^{\mathrm{c}}_{kl}, \tag{3.1}$$

where F^{e} and F^{p} are elastic and plastic deformation gradients. The velocity gradient tensor, L, is

$$L = L^{\mathrm{e}} + L^{\mathrm{p}}, \tag{3.2}$$

where $L_{ik}{=}\frac{\partial \dot{u}_i}{\partial x_k}{=}\dot{F}_{ij}(F^{-1})_{jk}$, $L^{\mathrm{e}}_{ik}{=}\dot{F}^{\mathrm{e}}_{ij}(F^{\mathrm{e}-1})_{jk}$, and $L^{\mathrm{p}}_{im}{=}F^{\mathrm{e}}_{ij}\dot{F}^{\mathrm{p}}_{jk}(F^{\mathrm{p}-1})_{kl}(F^{\mathrm{e}-1})_{lm}$ are the total, elastic, and plastic velocity gradients at time t in the current configuration. Strain rates are obtained symmetrizing Equation 3.2:

$$\dot{\varepsilon}(\mathbf{x}) = \dot{\varepsilon}^{\mathrm{e}}(\mathbf{x}) + \dot{\varepsilon}^{\mathrm{p}}(\mathbf{x}), \tag{3.3}$$

where $\dot{\varepsilon}$, $\dot{\varepsilon}^{\mathrm{e}}$, and $\dot{\varepsilon}^{\mathrm{p}}$ are the total, elastic, and viscoplastic Eulerian strain rates.

Zecevic et al. [89] introduced a linearly viscous heterogeneous medium in the current configuration which becomes homogeneous in the reference configuration. The use of the linear reference medium in the current configuration allows most variables to stay in this configuration. The linear viscous reference medium replaces its elastic counterpart used in Lebensohn [80] to reflect the predominance of viscoplasticity at larger strains, allowing for better convergence of the method in the majority of the deformation regime.

The constitutive equation extended from the small-strain EVP-FFT formulation [77, 83] is

$$\sigma_{ij} = L^0_{ijkl}\frac{\partial \dot{u}_k}{\partial x_l} + \sigma_{ij} - L^0_{ijkl}\frac{\partial \dot{u}_k}{\partial x_l} = L^0_{ijkl}\frac{\partial \dot{u}_k}{\partial x_l} + \phi_{ij}, \tag{3.4}$$

where L^0 is the viscous stiffness of the linear reference heterogeneous medium and the

Cauchy polarization field, ϕ, is $\phi_{ij}{=}\sigma_{ij}{-}L^0_{ijkl}\partial\dot{u}_k/\partial x_l$. In the reference configuration, the first Piola–Kirchhoff (PK1) stress, P is:

$$P_{ij}(\mathbf{X}) = L^{0,\mathrm{ref}}_{ijkl}\frac{\partial\dot{u}_k}{\partial X_l}(\mathbf{X}) + \phi^{\mathrm{PK1}}_{ij}(\mathbf{X}) \tag{3.5}$$

where $L^{0,\mathrm{ref}}_{inkm}{=}JL^0_{ijkl}(F^{-\mathrm{T}})_{jn}(F^{-\mathrm{T}})_{lm}$ is the homogeneous reference viscous stiffness in the reference configuration, $\phi^{\mathrm{PK1}}_{in}{=}J\tilde{\phi}_{ij}\left(F^{-\mathrm{T}}\right)_{jn}$ is the PK1 stress polarization field, and $J{=}\det F$. The polarization field accounts for the nonlinear and heterogeneous constitutive response, while the spatial variation of the reference stiffness in the current configuration accounts for the irregularity of the grid.

The equilibrium equation in the reference configuration is

$$\frac{\partial P_{ij}}{\partial X_j}(\mathbf{X}) = L^{0,\mathrm{ref}}_{ijkl}\frac{\partial^2\dot{u}_k}{\partial X_l\partial X_j}(\mathbf{X}) + \frac{\partial\phi^{\mathrm{PK1}}_{ij}}{\partial X_j}(\mathbf{X}) = 0. \tag{3.6}$$

Green's function method can be used to solve the periodic linear problem in the reference configuration. The fluctuation of the velocity gradient with respect to the average value in the reference configuration is [84, 85]

$$\frac{\partial\tilde{\dot{u}}_i}{\partial X_j} = -\int_{R^3}\Gamma^{\mathrm{ref}}_{ijkl}(\mathbf{X}-\mathbf{X}')\phi^{\mathrm{PK1}}_{kl}(\mathbf{X}')dV', \tag{3.7}$$

where $\Gamma^{\mathrm{ref}}(\mathbf{X}-\mathbf{X}')$ is the periodic Green's operator in the reference configuration that corresponds to the reference viscous stiffness, $L^{0,\mathrm{ref}}$. The convolution is taken over the regular reference grid and calculated efficiently in Fourier space using the equation $\widehat{\partial\tilde{\dot{u}}_i/\partial X_j}{=}\hat{\Gamma}^{\mathrm{ref}}_{ijkl}\hat{\phi}^{\mathrm{PK1}}_{kl}$. The Green's operator in Fourier space is taken to be $\hat{\Gamma}^{\mathrm{ref}}_{inkj}(\mathbf{0}){=}0$ at the origin to reflect the fact that the mean value of the fluctuation field vanishes.

The fluctuation field of the velocity gradient in the current configuration can be calculated as [89]:

$$\begin{aligned}\frac{\partial \tilde{\dot{u}}_i}{\partial x_n} &= \\ &- \left\{ \int_{R^3} \Gamma^{\text{ref}}_{ijkl}(\mathbf{X}-\mathbf{X}') \left[J(\mathbf{X}')\tilde{\phi}_{km}(\mathbf{x}') \left(F^{-1}(\mathbf{X}')\right)_{lm} \right] dV' \right\} \left(F^{-1}\right)_{jn} \\ &+ \frac{\partial \dot{U}_i}{\partial X_j} \cdot \left(F^{-1}\right)_{jn}.\end{aligned} \tag{3.8}$$

The differences between Equation 3.8 derived for an irregular grid for large strains and the analogous expression corresponding to a regular grid for small strains are minor. In the large-strain case, the polarization fluctuation in the current configuration is mapped to the reference configuration, and the convolution is mapped back to the current configuration. The remainder of the algorithm remains unchanged, and the constitutive relation still needs to evaluated in the current configuration. The expression for $\partial\tilde{\dot{\mathbf{u}}}/\partial\mathbf{x}$ in the small-strain implementation is retrieved when $F{=}I$ in Equation 3.8. For mixed boundary conditions, the unknown components of the average velocity gradient, $\langle\partial\dot{\mathbf{u}}/\partial\mathbf{x}\rangle$, are iteratively adjusted until the known and applied components of $\langle\sigma\rangle$ match, following Lebensohn et al. [83].

The fix-point Equation 3.8 and constitutive equations, which are described in following section, are solved iteratively with the augmented Lagrangian approach [79, 83]. For this, auxiliary Cauchy stress (Lagrange multiplier) and velocity gradient fields are introduced. The large-strain augmented Lagrangian algorithm of Zecevic et al. [89] is an extension of the small-strain EVP-FFT formulation of Lebensohn et al. [83].

Zecevic et al.'s [89] approach also adapted a centered difference approximation for derivatives originally proposed by Willot [116], and re-derived the expressions for the discrete Green operator. The final expression in Fourier space is

$$\hat{\Gamma}_{ijkl} = \left(L^0_{imkn} D_{mn}\right)^{-1} D_{jl} \tag{3.9}$$

where the D is the second-order centered difference operator in Fourier space defined as [117, 118]

$$D(i,j,k) = \tag{3.10}$$

$$\begin{bmatrix} 2\left(\cos\left(\frac{2\pi(i-1)}{N_1}\right)-1\right) & \text{sym} & \text{sym} \\ -\sin\left(\frac{2\pi(i-1)}{N_1}\right)\sin\left(\frac{2\pi(j-1)}{N_2}\right) & 2\left(\cos\left(\frac{2\pi(j-1)}{N_2}\right)-1\right) & \text{sym} \\ -\sin\left(\frac{2\pi(i-1)}{N_1}\right)\sin\left(\frac{2\pi(k-1)}{N_3}\right) & -\sin\left(\frac{2\pi(j-1)}{N_2}\right)\sin\left(\frac{2\pi(k-1)}{N_3}\right) & 2\left(\cos\left(\frac{2\pi(k-1)}{N_3}\right)-1\right) \end{bmatrix}. \tag{3.11}$$

where i, j and k are the indices of the grid points.

3.2.2 Constitutive equations

Under the adopted kinematics assumptions, the elastic constitutive equation in the current configuration is given by:

$$\dot{\varepsilon}^{\mathrm{e}}_{ij}(\sigma) = S_{ijkl}\sigma^{\nabla J}_{kl}, \tag{3.12}$$

where S is the elastic single crystalline compliance in the current configuration and $\sigma^{\nabla J}$ is the Jaumann rate of Cauchy stress given by

$$\sigma^{\nabla J}_{ik} = \dot{\sigma}_{ik} - \dot{\omega}^{\mathrm{e}}_{ij}\sigma_{jk} + \sigma_{ij}\dot{\omega}^{\mathrm{e}}_{jk}, \tag{3.13}$$

where $\dot{\sigma}$ is the total Cauchy stress rate, and $\dot{\omega}^{\mathrm{e}}$=asym$(\partial\dot{\mathbf{u}}/\partial\mathbf{x})-\dot{\omega}^{\mathrm{p}}$ is the elastic spin and $\dot{\omega}^{\mathrm{p}}$ is the plastic spin, given below. In this work, the viscoplastic deformation of the single crystal matrix surrounding the void is due to dislocation glide on 12 $\langle 110\rangle\{111\}$ potentially active slip systems, given by the following non-linear, incompressible, rate-sensitive equation relating the (symmetric) plastic strain rate $\dot{\varepsilon}^{\mathrm{p}}$ to the Cauchy stress at a single crystal material point $\mathbf{x}$ in the current configuration:

$$\dot{\varepsilon}^{\mathrm{p}}_{ij} = \sum_{\alpha} m^{\alpha}_{ij}\dot{\gamma}^{\alpha} = \dot{\gamma}_0 \sum_{\alpha} m^{\alpha}_{ij} \left(\frac{|m^{\alpha}_{kl}\sigma_{kl}|}{\tau^{\alpha}}\right)^{n} \operatorname{sign}\left(m^{\alpha}_{mn}\sigma_{mn}\right), \tag{3.14}$$

with $\dot{\gamma}^{\alpha}$, τ^{α}, and m^{α}_{ij}=sym($n^{\alpha}_i b^{\alpha}_j$) being, respectively, the shear rate, the critical resolved shear stress, and the symmetric part of the Schmid tensor, where $\mathbf{n}^{\alpha}$ and $\mathbf{b}^{\alpha}$ are the normal and Burgers vector direction of such slip system, $\dot{\gamma}_0$ is a reference rate, and n is the stress exponent. Correspondingly, the plastic rotation rate or plastic spin is given by the complementary anti-symmetric expression:

$$\dot{\omega}^{\mathrm{p}}_{ij} = \sum_{\alpha} \mu^{\alpha}_{ij}\dot{\gamma}^{\alpha} = \dot{\gamma}_0 \sum_{\alpha} \mu^{\alpha}_{ij} \left(\frac{|m^{\alpha}_{kl}\sigma_{kl}|}{\tau^{\alpha}}\right)^{n} \operatorname{sign}\left(m^{\alpha}_{mn}\sigma_{mn}\right), \tag{3.15}$$

where μ^{α}_{ij}=antisym($n^{\alpha}_i b^{\alpha}_j$). Elastic stretching of the lattice is ignored when accounting for the reorientation of the slip direction and normal, resulting in $b^{\alpha}_i = F^{\mathrm{e}}_{ij} b^{\alpha,\mathrm{ini}}_j \approx R^{\mathrm{e}}_{ij} b^{\alpha,\mathrm{ini}}_j$ and $n^{\alpha}_i = (F^{\mathrm{e-T}})_{ij} n^{\alpha,\mathrm{ini}}_j \approx R^{\mathrm{e}}_{ij} n^{\alpha,\mathrm{ini}}_j$, where “ini” indicates quantities in the initial configuration and R^{e} is the total lattice rotation, consisting of both material and plastic rotation. This rotation is also used to obtain the elastic compliance in the current configuration.

If the shear rates $\dot{\gamma}^{\alpha}(\mathbf{x})$ can be considered constant in a time increment Δt such that $\Delta\gamma^{\alpha}(\mathbf{x}) = \dot{\gamma}^{\alpha}(\mathbf{x})\Delta t$, the critical stresses of the deformation systems can be explicitly updated due to strain hardening. Here we use a Voce law [107], such that the evolution of the critical stress with accumulated shear strain in each grain is given by

$$\tau^{\alpha} = \tau^{\alpha}_0 + \left(\tau^{\alpha}_1 + \theta^{\alpha}_1 \sum_{\alpha} \gamma^{\alpha}\right)\left(1 - \exp\left(-\sum_{\alpha} \gamma^{\alpha} \left|\frac{\theta^{\alpha}_0}{\tau^{\alpha}_1}\right|\right)\right), \tag{3.16}$$

where τ^{α}_0, τ^{α}_1, θ^{α}_0, and θ^{α}_1 are the initial threshold stress, the initial hardening rate, the asymptotic hardening rate, and the back-extrapolated threshold stress, respectively.

3.2.3 Modifications to the LS-EVPFFT

Several modifications were introduced in the LS-EVP-FFT algorithm to allow for void growth while maintaining the desired boundary conditions.

The first modification was to maintain an axisymmetric stress triaxiality throughout the simulation while imposing a constant strain rate along the primary axis. The full axisymetric stress tensor, expressed in terms of triaxiality, σ_{tx}, and von Misses stress, σ_{vM}, with a primary axis in the z-direction, is:

$$\sigma_{ij} = \begin{bmatrix} \sigma_{\text{tx}} - 1/3 & 0 & 0 \\ 0 & \sigma_{\text{tx}} - 1/3 & 0 \\ 0 & 0 & \sigma_{\text{tx}} + 2/3 \end{bmatrix} \sigma_{\text{vM}}. \tag{3.17}$$

In the previous work by Christodoulou et al. [115] using DVP-FFT, the applied σ_{vM} was adjusted in order to satisfy the desired von Mises strain rate, $\dot{\varepsilon}_{\text{vM}}^{(\text{app,p})}$, using the following relationship derived from the homogeneity of degree n of the strain rate as a function of stress:

$$\sigma_{\text{vM}}^{(2)} = \left(\frac{\dot{\varepsilon}_{\text{vM}}^{(\text{app,p})}}{\dot{\varepsilon}_{\text{vM}}^{(1,\text{p})}} \right)^{1/n} \sigma_{\text{vM}}^{(1)}, \tag{3.18}$$

where the number in parentheses indicates the calculated (1) or target (2) stress/strain rate. This correction was applied after converging on the applied Cauchy stress.

In this work, rather than imposing the von Mises strain rate, we impose the strain rate component along the longitudinal principal axis, which mimics the CP-FE simulations of Ling et al. [2], for further comparison with the latter. The resulting largest principal stress component is in turn used to impose the stress triaxiality. At any given increment, the other components $\sigma_{jj\neq II}$ are:

$$\sigma_{jj\neq II} = \frac{\sigma_{\text{tx}} - 1/3}{\sigma_{\text{tx}} + 2/3}\sigma_{II}, \tag{3.19}$$

where σ_{II} is the largest principal stress.

Beyond this slight change in boundary conditions, it was necessary to make three additional changes to the LS-EVP-FFT to resolve numerical instabilities due to the impingement of void voxels into the surrounding material voxels as deformation evolves. Due to the infinite compliance of the void voxels, any velocity gradient field in the void satisfying the compatibility and with the correct volume average is an acceptable solution. As the void grows under the applied stress, the void voxels neighboring the matrix become closer and closer to the matrix voxels. The resulting small distances between the matrix and void voxels imply very large velocity gradients in the boundary void voxels, even for velocities similar to those of the material. Consequently, small numerical inaccuracies in the solution for the velocity gradient field in void voxels may lead to impingement of void voxels into the surrounding matrix. This instability was not as pronounced in previous LS-EVP-FFT applications Zecevic et al. [89], where internal voids were not present.

The first change was the use of adaptive time increments, with the purpose of improving the accuracy of the numerical solution and of the evolution of explicitly integrated variables (such as the deformation gradient field). If the simulation had not acceptably converged or the maximum von Mises strain at any voxel in the material exceeded 5%, the time increment was cut to Δt=5%/$\dot{\varepsilon}_{\text{vM}}$ s, and the time step was recalculated.

The second change made was to use the average velocity gradient of the previous step as the initial guess for the local velocity gradient, i.e. $(\partial\dot{\mathbf{u}}/\partial\mathbf{x})^{0,t+\Delta t}=\langle\partial\dot{\mathbf{u}}/\partial\mathbf{x}\rangle^{t}$, as opposed to using the local velocity gradient of the previous step. As noted above, due to the infinite compliance of the void phase, there are infinitely many acceptable solutions for the velocity gradient field in the void, and thus the initial guess may affect the velocity gradient solution in the void. Starting with a uniform initial guess for the velocity gradient field in the void (and material) leads to a more uniform solution for the velocity gradient field in the void that is still acceptable and results in less localization in the void. On the other hand, the velocity gradient field in the material phase is not affected by the initial guess. This change minimizes the tendency of the boundary void voxels to quickly approach the surrounding material, which appears to be the root cause of numerical convergence issues.

Even with two previous changes in place, it was still necessary to artificially correct the velocity field in the critical void voxels to achieve large distortions of the void. After each time step, before the position of the voxels is updated, the velocity of certain void voxels is interpolated to be similar to that of the neighboring material voxels. Only the void voxels at the corners and edges of the cube in the reference configuration were adjusted. First, a displacement vector, Δx was calculated as the displacement between the neighboring voxel and the void voxel:

$$\Delta\mathbf{x}\{\ \mathbf{x}^{\mathrm{V}}\} = \mathbf{x} - \mathbf{x}^{\mathrm{V}} \tag{3.20}$$

Then, the interpolated velocity of the material points was taken to be

$$\mathbf{v}\{\mathbf{x}^{\mathrm{V}}\} = \frac{\sum_{M} \mathbf{v}\{\mathbf{x}\}\left|\Delta\mathbf{x}\{\mathbf{x}^{\mathrm{V}}\}\right|^{-3}}{\sum_{M} \left|\Delta\mathbf{x}\{\mathbf{x}^{\mathrm{V}}\}\right|^{-3}} \tag{3.21}$$

where M indicates that only neighboring *material* points are considered. This interpolated velocity is adjusted to be 1% faster if the velocity and average displacement vector were antiparallel, and 1% slower if they were parallel (i.e., the velocity was adjusted to be 1% greater away from the material). The void voxel was then assigned this adjusted interpolation.

The velocity gradient in the entire volume was then calculated using the corrected velocity field, and used for updating of deformation gradient for next time increment. It was during this re-calculation of the velocity gradient that the discrete Green's operator is used, to avoid adding additional spurious numerical oscillations. Apart from this, the algorithm used the continuous Green's operator.

Even with these changes implemented, there were some levels of strain when the void voxels would impinge upon the surrounding material and convergence was not achieved. These non-converged cases are not included in the results that follow.

3.3 Simulation setup for verification

The unit cell discretization used in this work follows Appendix B of Zecevic et al. [89], which provides the mapping of a 2D square inclusion (or heterogeneity) in the reference configuration to a circular inclusion/heterogeneity in the initial configuration, optimizing the position of the centers of each voxel to improve the accuracy of the representation of the void's circular shape. The algorithm was extended to a third dimension, mapping a cube to a sphere, and optimizing the location of the surface area of the void-material boundary. Positions of the remaining voxels in the unit cell were interpolated using the optimized locations of boundary voxels. The relevant equations to transform the cubic void region in the reference configuration with position vector $\mathbf{X}$ to a spherical void in the initial configuration with position vector $\mathbf{x}$ are

$$x_1 = X_1\sqrt{1 - \frac{X_2^2 + X_3^2}{2} + \frac{X_2^2 X_3^2}{3}} \tag{3.22}$$

$$x_2 = X_2\sqrt{1 - \frac{X_1^2 + X_3^2}{2} + \frac{X_1^2 X_3^2}{3}} \tag{3.23}$$

$$x_3 = X_3\sqrt{1 - \frac{X_1^2 + X_2^2}{2} + \frac{X_1^2 X_2^2}{3}}. \tag{3.24}$$

First, for verification of our implementation, single-step simulations were performed to ensure that the stress in the material surrounding the void agrees with available analytical solutions obtained from Eshelby's inclusion theory. Then, cases of void growth in single crystals are compared with available CP-FE and DVP-FFT simulations. In particular, we present comparisons with Ling et al. [2]'s CP-FE simulations to ensure that the void shapes and fields are consistent with a different large-strain formulation, and with DVP-FFT simulations, in terms of macroscopic quantities. While we expected differences due to elasticity in the current formulation, it was useful to confirm that both FFT-based models give similar, although not identical, results.

Three types of unit cells were used in this work. All cases contained one void at the center of the simulation cell with these characteristics:

- a 2D single crystal with 1.2% initial porosity, for a single loading step (i.e. no void growth), to compare with Eshelby's solution for the stress field at the void/matrix boundary;
- a 3D single crystal with 0.8% initial porosity, for a single loading step, (i.e. no void growth), to compare with Eshelby's solution for the stress field at the void/matrix boundary; and
- 3D single crystals with initial 1% porosity, to compare with CP-FE simulations.

The first two cases were intended to verify the initial step of the LS-EVP-FFT simulations by comparing numerical results with analytical solutions from Eshelby's theory,

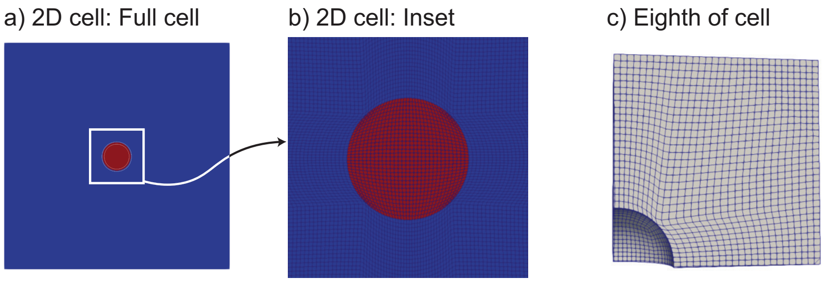

Figure 3.1: Simulation cells used in this work. (a-b) 2D simulation cells, where (a) shows the entire cell without the cell boundaries marked, and (b) shows the void (in red) more closely with the cell boundaries marked. (c) Eighth cell of the 3D cell that was used for the single crystal simulations.

and are discussed in subsection 3.4.1. The first simulation consisted of a 2D 256×256 simulation cell with a circular (cylindrical) void in the center that was 31 voxels in diameter (Figure 3.1(a-b) shows the full cell, and an inset image focusing on the void). The second case consisted of a 3D 64×64×64 unit cell with a void in the center with 16 voxels in diameter (Figure 3.1(c) shows an eighth-cell corresponding to that geometry. These 3D simulations allow further comparison with analytical stress fields obtained from Eshelby's theory. Note that the diameter of the 3D cell was chosen to place voxel centers directly on the xy-, yz-, and zy-planes that passed through the center of the void.

The third set of simulations consisted of 3D single crystals, with dimensions of 64×64×64 and a void placed at the center with diameter 17 voxels (corresponding directly to the eighth-cell shown in Figure 3.1(c)), resulting in 1% volume fraction of the void. This choice allowed a reasonable resolution while avoiding void interaction with periodic repetitions of the unit cell. The purpose of these simulations was to compare the LS-EVP-FFT to DVP-FFT in terms of macroscopic response and to the CP-FE simulations of Ling et al. [2] in terms of local fields and void shape.

Most simulations were conducted imposing a stress triaxiality σ_{tx}=3.0, a constant axial strain rate $\dot{\varepsilon}_{33} = 1.0s^{-1}$, and an initial time step, Δt=2×10^{-3}s. The 2D simulations were performed for plane stress that was equal in the x- and y-axes, and the constant axial strain rate was applied in the x-axis ($\dot{\varepsilon}_{11}$=1.0s^{-1}). Both single-step simulations, discussed in subsection 3.4.1, use an initial time step Δt=1×10^{-3}s. For the comparison with CP-FE results (3rd set of simulations) additional cases with stress triaxiality σ_{tx}=1 and initial time step Δt=6×10^{-3}s are also reported. In all cases, the FCC crystals deform plastically by $\langle 110\rangle\{111\}$ slip, with a reference slip rate $\dot{\gamma}_0$=1.0/s, and, in most cases, a stress exponent n=5 (see Equation 3.14). Notable exceptions to the adoption of this non-linear viscoplastic behavior is the use of a linear viscosity, n=1, to consider a linear viscoelastic material for comparison with Eshelby's analytical stress fields, which are available for linear material behavior. The adopted Voce hardening parameters from Equation 3.16 were τ_0=1.0 MPa, τ_1=3.0 MPa, θ_0=8.0 MPa, and θ_1=0.0 MPa. For the isotropic elasticity constants, Young's modulus and Poison's ratio, ν, were adopted to be 1000 MPa, and 0.3, reflecting the constants used in the FEM in Christodoulou et al. [115].

3.4 Verification

3.4.1 Comparison with analytical solutions

The results of the first two sets of simulations, intended to verify the LS-EVP-FFT extension to the case of a spherical void in a single crystal, are compared with analytical expressions for the stress field at the rim of the void, obtained using Eshelby's equivalent inclusion method. For this, we use the analytical solution in the case of a linear (viscoelastic) material, for comparison with LS-EVP-FFT calculations with stress exponent n=1.

The equivalent eigen-strain-rate, $\dot{\varepsilon}^{**}_{mn}$, in the case of an anisotropic viscoelastic material containing an ellipsoidal heterogeneity, under an applied stress, σ^0_{mn}, can be calculated from the expression [119]:

$$[(L^{\mathrm{I}}_{ijkl} - L^{\mathrm{M}}_{ijkl})S_{klmn} + L^{\mathrm{M}}_{ijmn}]\dot{\varepsilon}^{**}_{mn} = -(L^{\mathrm{I}}_{ijkl} - L^{\mathrm{M}}_{ijkl})\left(L^{\mathrm{M}}_{klmn}\right)^{-1}\sigma^{0}_{mn} \tag{3.25}$$

where L^{M} and L^{I} are the viscoelastic stiffness tensors of the matrix and the inhomogeneity, respectively, and S is the Eshelby tensor. Conveniently, when the heterogeneity is a void, $L^{\mathrm{I}} = 0$, and $\dot{\varepsilon}^{**}_{mn}$ can be written as:

$$\dot{\varepsilon}^{**}_{ij} = (L^{\mathrm{M}}_{ijmn} - L^{\mathrm{M}}_{ijkl}S_{klmn})^{-1}\sigma^{0}_{mn} \tag{3.26}$$

The stress at the boundary of an inclusion σ^{b} is:

$$\sigma^{b} = \sigma^{0} + \sigma^{\mathrm{in}} + [\sigma] \tag{3.27}$$

where σ^{in} and $[\sigma]$ are the stress inside the inclusion and the stress jump across the boundary, respectively. Since the stress in the void, $\sigma^{\mathrm{in}}+\sigma^{0}$, is zero, the stress at the boundary is the discontinuity of stress, given by [119]:

$$[\sigma]_{ij} = L^{\mathrm{M}}_{ijkl}\left(-L^{\mathrm{M}}_{pqmn}\dot{\varepsilon}^{**}_{mn}n_q n_l K^{-1}_{kp} + \dot{\varepsilon}^{**}\right), \tag{3.28}$$

where $K_{ik}=L^{\mathrm{M}}_{ijkl}n_j n_l$, and $\mathbf{n}$ is the normal to the boundary.

In the case of a viscoelastic material, the constitutive behavior of the matrix is given by: $\sigma_{ij}=L^{\mathrm{M}}_{ijkl}\dot{\varepsilon}_{kl}$. To obtain L^{M}_{ijkl}, it is convenient to add the elastic and viscous parts of the strain rate to give:

$$\dot{\varepsilon}_{ij} = M_{ijkl}\sigma_{kl} + \left(\frac{C^{-1}}{\Delta t}\right)_{ijkl}\sigma_{kl} = (L^{\mathrm{M}}_{ijkl})^{-1}\sigma_{kl} \tag{3.29}$$

where M and C^{-1} are the viscous and elastic compliances of the material, respectively. Evaluating Equation 3.14 for n=1, results in:

$$(L^{\mathrm{M}}_{ijkl})^{-1} = \dot{\gamma}_0 \sum_{\alpha} \frac{m^{\alpha}_{ij} m^{\alpha}_{kl}}{\tau^{\alpha}} + \left(\frac{C^{-1}}{\Delta t}\right)_{ijkl} \tag{3.30}$$

In the case of [100]−[010]−[001]-oriented crystal with isotropic elastic properties, the stiffness tensor maintains cubic symmetry.

It is important to note that the chosen Δt impacts the value of L^{M}. For small values of Δt, the elastic stiffness tensor, which is readily invertible, dominates. However, this does not capture the viscoelastic nature of the desired solution. For very large values of Δt, the incompressible viscous compliance dominates, leading to stiffness that would be orders of magnitude larger. Therefore, Δt=$10^{-3}s$ was chosen, to allow for a reasonable balance between the elastic and viscous compliances.

Using both cylindrical and spherical voids results in the following comparisons: Figure 3.2 shows the stress in the material at the void boundary given by the 2D FFT-based method (dots) and corresponding analytical results based on Eshelby's theory (solid lines), using the same macroscopic stress ($0.716\tau_0$ in the x- and y-axes, zero out of plane, dotted lines). The figure shows each component of the stress as a function of angle, θ, measured in polar coordinates with r=0 at the center of the void. As is visible in the figure, the matching is good in general, except out of the plane, where the normal stress σ_{33} given by FFT-based calculations in Figure 3.2c exceeds the predicted values, at the corners (in the reference configuration), at θ=$\pi/4+n\pi$. This deviation is likely due to the large conformal deformation in those regions, and is partially countered using the average velocity gradient as an initial guess in the multi-step simulations. Additionally, it is in these regions that void velocity is greater than in the material, for the same reasons.

Figure 3.3 shows the stress in the material at the void boundary calculated with the

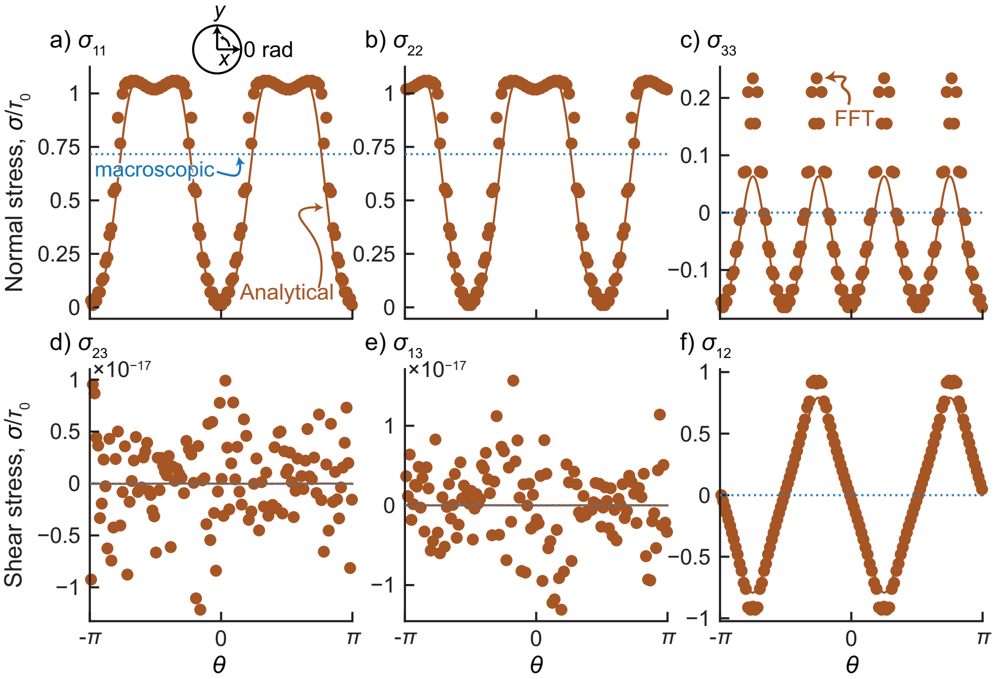

Figure 3.2: Stress at the void boundary of a circular/cylindrical void in a [100]-oriented grain with a constant strain rate with equal stresses applied in the xy-plane, where θ is the signed angle in radians between the vectors that start at the void center and pass through the material point with the highest x-value and the material point in question. Dots correspond to the voxels in the FFT-based calculation, and lines are analytical results based on Eshelby's theory.

3D FFT-based model (dots), and corresponding analytical results based on Eshelby's theory (solid lines), using the same macroscopic stress (σ_{33}=1.0646τ_0, σ_{tx}=3.0, dotted lines). The figure shows each component of the stress as a function of angle, θ, measured in polar coordinates with r=0 at the center of the void, along the three great circles that pass through the origin and lie in the xy-, yz-, and zx-planes, where θ=0 at the highest value of x, y, and z, respectively, as indicated in Figure 3.3. The match is good, except, once again, at the corners of the void in the reference configuration (θ=$\pi/4+n\pi$), where the values in the FFT-based predictions exceed the analytical results, for the same reason as in the 2D case.

3.4.2 Comparison with CP-FE

For comparison of the proposed extension of LS-EVP-FFT with the CP-FE simulations of Ling et al. [2], three voided single crystal unit cells were considered, with orientations [100]-[010]-[001], [111]-[$\bar{2}$11]-[0$\bar{1}$1], and [$\bar{1}$25]-[$\bar{2}$11]-[210] aligned with the axes of the cell. The applied boundary conditions also matched [2], with the primary stress axis (direction of the largest principal stress) aligned with the x-axis. The three cases are labeled according to the crystal orientation of the primary axis: [100], [111], and [$\bar{1}$25]. Ling et al. [2]'s cases with stress triaxialities 1.0 and 3.0, and a constant axial strain rate $\dot{\varepsilon}_{11}$=1s^{-1} were simulated and compared with the CP-FE results.

Figure 3.4 and Figure 3.5 show contour plots of total cumulative plastic slip, $\gamma_{\text{cum}} \equiv \sum_\alpha \gamma^\alpha$, comparable with Figures 7 and 8 of Ling et al. [2]. Figure 3.4 shows the contour plots of γ_{cum} at 10% axial strain for stress triaxiality σ_{tx}=1. There is only a small amount of void growth, but the strain fields are qualitatively similar to the γ_{cum} in Figure 7 of Ling et al.'s, shown at left. The shapes of the simulation cells and voids are also similar. Relative minor quantitative differences can be attributed to the differences in material

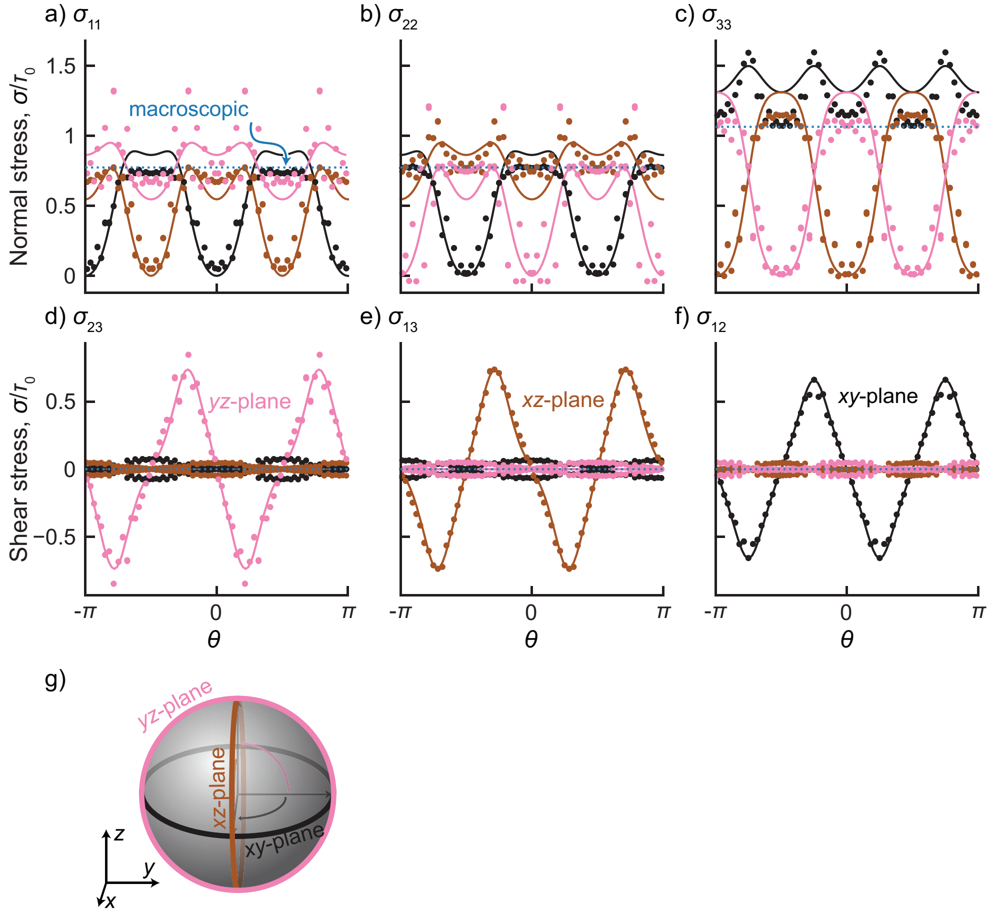

Figure 3.3: Stress along great circles with plane normal in each Cartesian direction at the void boundary of a spherical void in a [100]-oriented grain with a constant $\dot{\varepsilon}_{33}$ strain rate and a stress triaxiality σ_{tx}=3, where θ is the signed angle in radians between the vectors that start at the void center and pass through the material point with the highest x, y, and z value and the material point in question for the xy-, yz-, and xz-planes, respectively (shown in g). Dots correspond to the voxels in the FFT-based calculation, and lines are analytical results based on Eshelby's theory.

parameters and hardening law, as well as to the use of different micromechanical solvers (CP-FE vs. LS-EVP-FFT).

Figure 3.5 shows the contour plots of γ_{cum} at 10% axial strain for stress triaxiality σ_{tx}=3, except for the [111]-oriented crystal, which is shown at 5.8% axial strain due to numerical instabilities for that case. There is more accumulated deformation than in the previous cases, and the fields are qualitatively similar to accumulated plastic slip from Figure 8 of Ling et al.'s, shown at left.

3.4.3 Comparison with DVP-FFT

We now compare void growth predictions in single crystals, previously performed with DVP-FFT in chapter 2, and with the new LS-EVP-FFT implementation. Five crystal orientations were simulated: [100]-[010]-[001], [100]-[01$\bar{1}$]-[011], [1$\bar{1}$0]-[11$\bar{2}$]-[111], [210]-[1$\bar{2}$1]-[$\bar{1}$25], [100]-[01$\bar{2}$]-[021], all loaded primarily along the z-axis. For convenience, these cases will be identified by the crystallographic orientation aligned with the primary axis, i.e., [001], [011], [111], [$\bar{1}$25], and [021]. The Taylor factors for these five orientations, for exponent n=5, are: 1.933, 3.187, 3.331, 2.482 and 1.933. In what follows, the use of the terms "hard" and "soft" will refer to high and low values of Taylor factor, respectively. These orientations, used for the majority of the single crystal and bicrystal simulations, were the ones chosen by Han et al. [48], and Ling et al. [2].

Figure 3.6 shows the DVP-FFT and LS-EVP-FFT predictions of: (a) volume fraction of the void, (b) axial stress, and (c-d) transverse plastic strains, as a function of axial plastic strain for cases [021], [001], [$\bar{1}$25], [011], and [111], ordered here by void growth rate, from slowest to fastest. All indicators show similar trends, as predicted by both models. The case of [111]-oriented crystal, i.e. the orientation with the largest Taylor factor, showed the highest stresses, and, as a result, experienced the fastest increase in

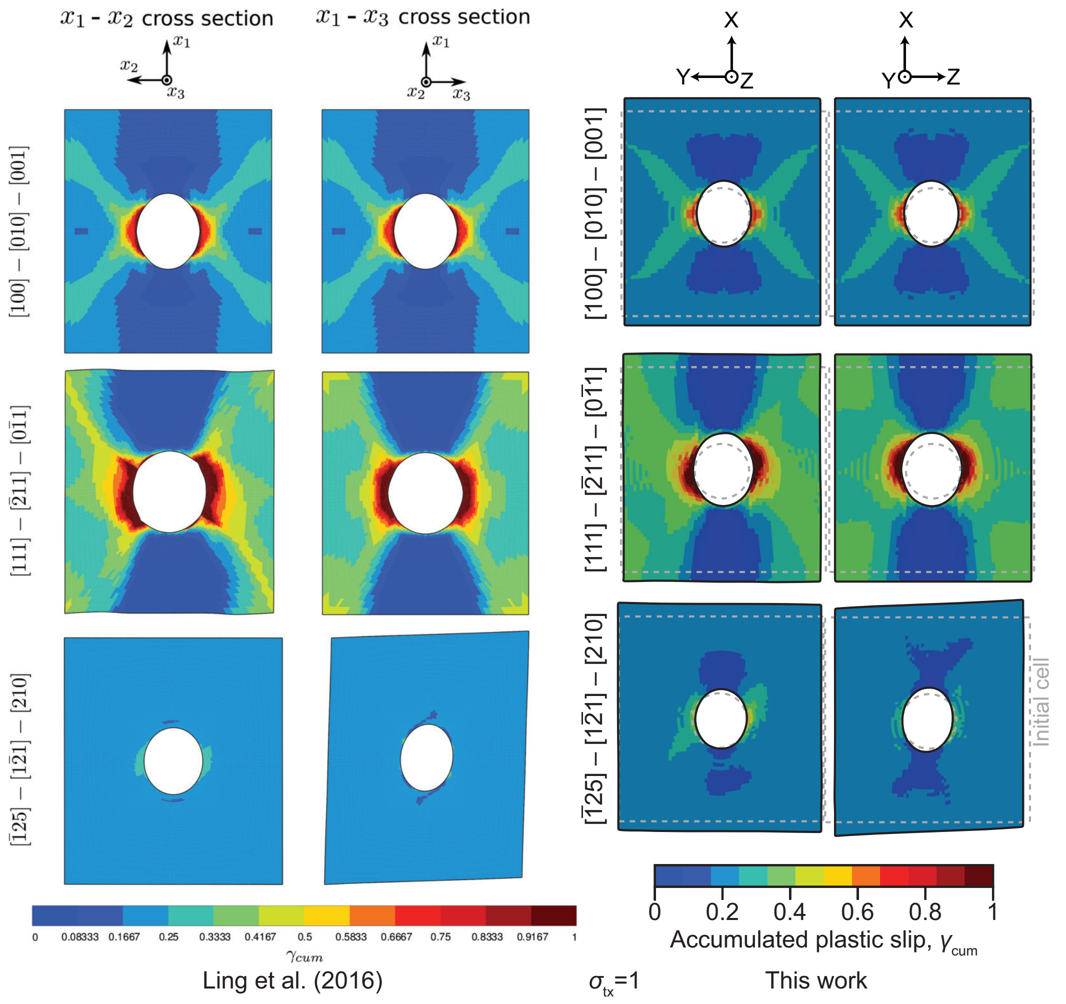

Figure 3.4: Right two columns: contour plots of LS-EVP-FFT predictions of accumulated plastic slip, γ_{cum}, in the x-y (left) and x-z (right) cross sections, for the three indicated crystallographic orientations and for stress triaxiality σ_{tx}=1 at 10% axial strain. Note that the final shape of the unit cells, void shapes, and total cumulative plastic slip fields are similar to the CP-FE predictions of Ling et al. [2], shown in the left two columns.

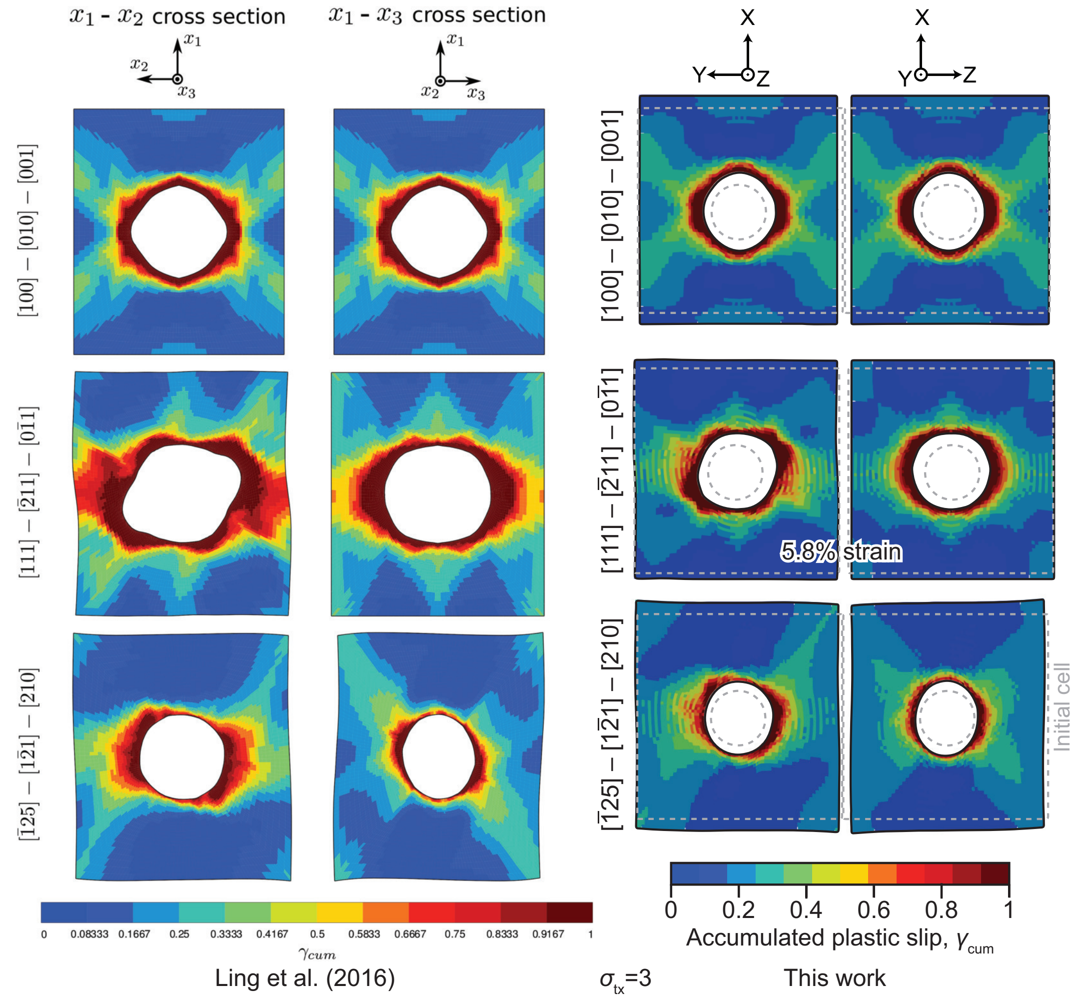

Figure 3.5: Right two columns: contour plots of LS-EVP-FFT predictions of accumulated plastic slip, $\gamma_{\rm cum}$, in the x-y (left) and x-z (right) cross sections, for the three indicated crystallographic orientations and for stress triaxiality $\sigma_{\rm tx}$=3 at 10% axial strain, except for the [111]-oriented crystal in the LS-EVP-FFT case, shown at 5.8%, due numerical instabilities beyond that strain. The final shape of the unit cells, void shapes, and total cumulative plastic slip fields are similar to the CP-FE predictions of Ling et al. [2], shown in the left two columns.

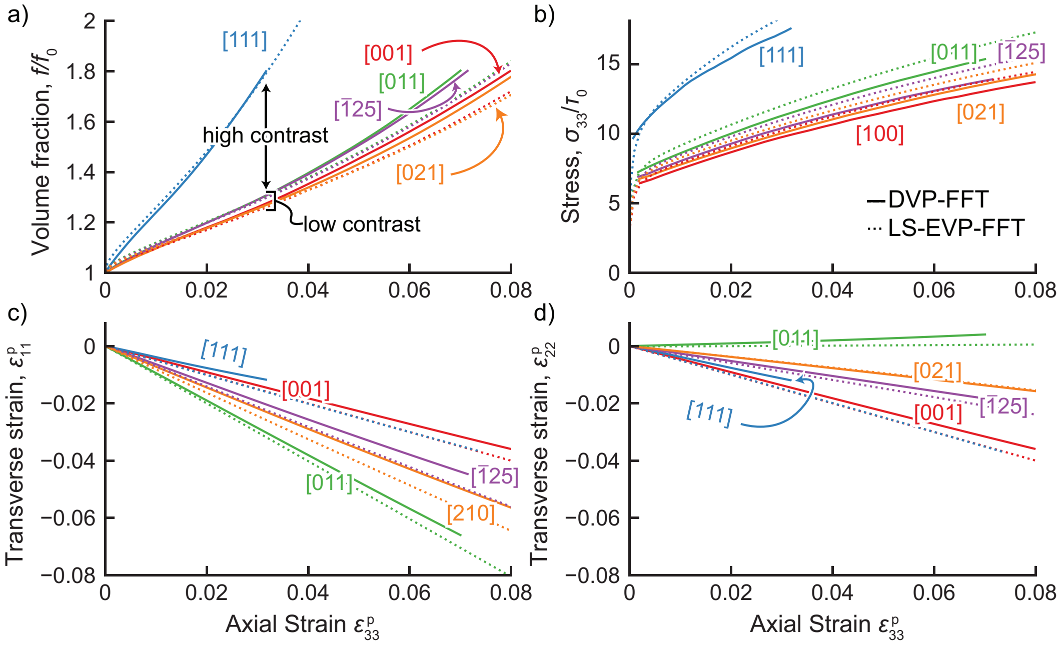

Figure 3.6: Comparison between DVP-FFT (solid lines) and LS-EVP-FFT (dotted lines) predictions in single crystals for triaxiality σ_{tx}=3. (a) Volume fraction of the void (porosity), (b) axial stress, (c) and (d) transverse strains in the x- and y-directions, as a function of axial plastic strain, ε^p_{33}. (a) The relative differences in porosity are less than 6% between models, and the stresses differ by no more than 9% for each crystal orientation. The labels of high and low contrast are used later and are described in the text.

porosity. For the other single crystal orientations, both models predict slightly different overall porosity rates, but in the same order, from slowest to fastest, as noted above. In general, Taylor factor dictates the growth rate, and harder crystals in strain-rate-controlled simulations generally exhibit a faster void growth, because the stress at any given strain is higher under these loading conditions. It is important to note that in stress-controlled simulations, Christodoulou et al. [115] showed the opposite relationship with Taylor factor, with voids growing fastest in soft single crystals, i.e. with low Taylor factors, and slowest in hard single crystals, with high Taylor factors. This reversal is important for the analysis of the results that follow.

A note on void growth contrast in single crystals

Both models show a significant contrast between porosity evolution and stress between the [111] case and all other cases. For the remainder of this work, we will use the terms "high-contrast" and "low-contrast" when referring to grain boundaries. These designations refer to the contrast in the growth rate of the voids in the single crystals forming the grain boundary. All bicrystal simulations involving a [111] grain combined with any of the four other orientations are considered to be "high-contrast," due to the fact that voids in this single crystal grew quickly relative to the other single crystals. Also, the stress in the [111] case was much higher than in the other cases. All other GB simulations would be considered "low-contrast" (as indicated in Figure 3.6(a)), given that the void volume fraction vary no more than about 20% during the corresponding single crystal simulations. The stress in these simulations do not differ by much as well. Other grain boundaries can be categorized in terms of contrast, as in the following chapter, which also uses this term to describe low-energy coherent grain boundaries, which do not use these five orientations.

3.5 Summary

This chapter provides an overview of the large-strain (LS) elasto-viscoplastic (EVP) fast-Fourier transform (FFT) algorithm that was developed by Zecevic et al. [89] and modified to accommodate void growth. This version of the LS-EVP-FFT will be used in the next two chapters to explore void growth in single and biphase metals.

The LS-EVP-FFT model builds upon the small-strain EVP-FFT model developed by Lebensohn et al. [83], and incorporates two novel elements: The first is the use of a stress-free deformation "conformal" gradient, which is applied to the regular, rectangular *reference* configuration before the first step to produce the *current* configuration. This conformal gradient allows for the accurate geometric representation of a spherical void, avoiding the stairstep pattern that results when modeling circular or spherical inclusion on regular, rectangular grids, and the noise in the mechanical fields that results from this stair-step pattern. The second is the use of a linearly viscous heterogeneous medium in the current configuration that is homogeneous in the reference configuration. The use of a linear viscous reference in place of an elastic reference medium allows better convergence during the plastic deformation regime. The transformation of the heterogeneous medium into a homogeneous medium in the reference configuration using the conformal gradient allows the use of the small-strain EVP-FFT algorithm, with only minor modifications, to solve large-strain calculations.

For this thesis work, additional steps were taken to improve the numerical stability of the algorithm when an infinitely compliant void was introduced. First, the time increment, Δt, was reduced to avoid excessively large plastic strains in one time step, to improve the accuracy of the overall solution and of the evolution of explicitly integrated variables. Second, the average velocity gradient of the entire unit cell of the previous step was used as the initial guess of each step, as opposed to the local average velocity gradient of the previous step, to reduce the tendency of the boundary void voxels to rapidly approach the material voxels. Finally, the velocity of certain voxels in the void was interpolated to be that of the surrounding material, to avoid void voxels impinging into the material.

Several simulations were conducted for verification of the model. In these simulations, the void is modeled as a square or cube in the reference configuration in 2D or 3D simulations, which mapped to a circle or sphere in the initial configuration. For the first set of simulations, we compared 2D and 3D simulations with Eshelby solution for a void in a matrix with cubic symmetry. The agreement was generally very good, but the model did overpredict the stress and strain in the regions with the greatest “conformal” deformation, which are the corners of the void in the reference configuration. These are the voxels whose velocities were interpolated at the end of each step, alleviating the overprediction in multistep simulations.

Qualitative agreement was achieved between the LS-EVP-FFT and the CP-FE simulations of Ling et al. [2]. However, the LS-EVP-FFT model has a limit on the maximum strain that can be accommodated by the voids that is not present in the CP-FE method. This limit is due to the impingement of void voxels past the material boundary, resulting in negative values of the Jacobian of deformation. However, the fields are smoother than would be possible with the dilatational viscoplastic (DVP) FFT used in the previous chapter.

Based on a selection of simulations of single crystals with voids, there is very good agreement between the macroscopic response of the DVP-FFT and the LS-EVP-FFT. These simulations, as in the previous chapter, show that stress and the rate of void growth under strain-rate controlled loading are highest in the [111]-oriented crystals in FCC. The five orientations used in these simulations will be used in future chapters.

Finally, the concept of "contrast" was introduced, which is the difference in void volume fraction at a given strain between two single crystals with different crystallographic orientations. "High-contrast" refers to a large difference in the volume fraction of the void between two single crystal simulations (such as between a [111]-oriented crystal and any of the four other orientations), and "low contrast " refers to a small difference. This concept is based solely on knowledge of void growth within the individual single crystals. As such, it can be considered a characteristic of void growth at the junction of any combination of grains without further calculation.

Chapter 4

Voids at grain boundaries

4.1 Introduction

The role of microstructure on void growth in metallic, polycrystalline materials that deform plastically by dislocation glide is not well understood. A number of ex-situ studies showed the formation of voids in these materials [1, 6, 19, 30, 120], but they did not allow for the observation of the directionality of growth. In spallation experiments, relevant information on void nucleation and growth is mostly lost, as voids coalesce and span multiple grains [1, 8, 30, 114]. Because void growth is difficult to capture in in-situ experiments with crystallographic information, microstructural effects on void nucleation and growth is mostly understood via computational modelling or analytical results.

Ex-situ studies in high-purity metals have indicated that voids form at grain boundaries and that the inclination angle with respect to the largest principal stress direction plays a role in nucleation [7, 30], both of which have been confirmed by Molecular Dynamics (MD) simulations [55, 64]. The study of nucleation is critical and an appropriate problem for MD, but not as suitable at higher length-scales. In the continuum-level approach used in this chapter, simulations start with a void already nucleated at grain boundaries or triple junctions. In polycrystalline metals, voids tend to nucleate at defects like grain boundaries, after which the rate of void growth is of interest to correlate microstructural features and damage resistance. Recent studies have shown that voids often appear to grow or exist more in one grain over another, while still located at grain boundaries, triple junction lines, or quadruple points. Francis et al. [7] showed that in spalled Ta, voids at grain boundaries tended to be larger in key crystal orientations, beyond reaffirming that frequent sites for incipient void formation were grain boundaries and triple junctions.

A number of micromechanical/crystal plasticity (CP) simulations in the literature have sought to understand void growth in crystalline metals. These simulations have indicated that crystallography plays a key role in the growth of voids in grain interiors [2, 50, 52, 121–123]. In chapter 2 the dilatational viscoplastic fast Fourier transform (DVP-FFT) model of Lebensohn et al. [90] was used to show that in strain-rate controlled simulations with axisymmetric loading, voids grew fastest in FCC single crystals that had the higher Taylor Factors, a value that is typically associated with how geometrically "hard" or "soft" an orientation is. It was also noted that in stress-controlled simulations, the opposite was true: the voids grew faster in single crystals with lower Taylor factor.

Other works aimed at understanding void growth at grain boundaries, phase boundaries, and triple junctions. Starting with the most simple configuration, given by a void at the intersection of a FCC bicrystal with a given inclination angle, Dakshinamurthy et al. [72] used CP Finite Elements (CP-FE) focusing on void shape in the two grains on either side of the grain boundary. They found that at high triaxialities, voids grew faster into the softer grain compared to its harder neighbor. The micromechanical fields at remote locations from the void converged to that of the single crystal for the same loading state. This study did not vary the grain boundary inclination relative to the loading direction.

While several experimental and modelling works mentioned earlier found the importance of grain boundary inclination angle on nucleation of voids, only a few studies have focused on how this variable affects void growth. Liu et al. [124, 125] built upon their CP-FE single-crystal FCC void growth work and simulated bicrystal configurations, looking at intra- and inter-granular fracture with grain boundary inclinations at 0/45/90°. In [124], they found that unit cells with 0°-inclined grain boundaries failed by transgranular fracture, while the tilted grain boundary (45°) failed by intergranular fracture. In [125], they extended their study to coalescence, a topic which will not be discussed here. Wen and Yue [126] performed a CP-FE study of inclination angle and focused on stresses at the grain boundary in Ni superalloys. They found that, in anisotropic bicrystals, high stresses, including high stress gradients, were apparent near the grain boundary, especially close to the void. They also noted that the crystallographic orientation of grains and the loading direction dictated the extent of these elevated values.

Misorientation is an additional common quantity used to describe grain boundaries, and there are several studies that attempted to understand how void growth is affected by this variable. Chen et al. [51] used misorientation and tilt/twist character to describe void growth/slip activation in CP-FE simulations of Ni-based superalloys. They found that twist boundaries, relative to a [001] single crystal, promoted void growth, while tilt boundaries strongly reduced the void growth in stress-controlled simulations. They also observed asymmetric growth on either side of the grain boundary. Asim et al. [73] studied phase boundary inclination, and its effect on void growth at the interface of FCC-HCP bicrystals using CP-FE. It is important to note that they maintained the HCP crystal orientation to the grain boundary inclination, thus conflating certain results of the phase boundary inclination study with crystal orientation. They found that inclination angle in this context strongly affected total void growth.

Other studies have also looked at voids at triple junctions. Jeong et al. [74] used

CP-FE to investigate voids at grain boundaries and triple junctions in BCC using displacement boundary conditions. In their study, the bicrystal simulation cells consisted of voids at a grain boundary whose normal was parallel to the primary axis of loading. For their triple junction study, they introduced a new grain boundary whose normal was perpendicular to the loading direction. They found that the rate of void growth in bicrystals contradicted that of their single crystal counterparts, in that the voids grew fastest to slowest in the [110], [111], and [100]-oriented single crystals, but when in a bicrystal or tri-crystal, the voids grew fastest in the [100] grain and slowest in the [110] grain. The orientation dependence on void growth rate was attributed to relative strength differentials in the bicrystals, and stress in the single crystals. They also noted that the activation pattern of multi-slip is similar in single crystals and bicrystals, but the shear strains differ. Zhang et al. [66] used MD to study voids at triple junctions in a Ni film, and found that simply swapping grain locations without changing the orientations themselves, resulted in different growth, both in morphology and volume fraction.

All the aforementioned works identified either misorientation, grain boundary inclination, or grain orientation as the dominant variable and studied the trends that resulted from their variation. However, the combined effect of all three descriptors has been rarely investigated. Few studies have analyzed the extent to which growth occurs into one grain or another, despite the evidence, both in experiments and simulations, that void growth is not generally equal on both sides of a grain boundary. There is an additional question as to why voids might grow faster into harder grains (grains with a high Taylor Factor, and a lower propensity for plastic slip at the same stress), as in Francis et al. [7], given there is strong evidence from the literature suggesting that voids should always grow into the softest grain. Perhaps voids form in a harder grain, rather than right at the grain boundary, and grow toward the boundary. It is also worth noting that the choice of strain- or stress-controlled boundary conditions have a strong influence on which grain voids grow most quickly into.

The work in this chapter seeks to identify the role of grain boundary inclination and adjoining crystal orientations on the growth of already nucleated voids in FCC metals. We consider an isolated void at a grain boundary or a triple junction, far from any other neighboring grains. To that end, we adapted a recently developed large-strain elasto-viscoplastic fast-Fourier transform-based (LS-EVP-FFT) formulation [89] to model void growth, and used it to simulate the growth of voids at grain boundaries with varying grain boundary inclination, misorientation, and crystallographic orientation of both grains. The first case is concerned with low-energy coherent grain boundary orientation relationships, followed by a larger study of grain boundary inclination and grain orientation. The initial void location relative to the grain boundary is also studied. Finally, we study cases of voids at triple junctions. These simulations demonstrate that the orientations of the crystals on both sides of the grain boundary, relative to the main axis of loading, have the strongest influence on void growth at grain boundaries, larger than either misorientation or grain boundary inclination. For most grain orientations the void growth in bicrystal follows the rule of mixtures of single crystalline void growth. However, for a subset of bi-crystal orientations, we observed that there exists a subset of bicrystal orientations at which voids grow faster in the bicrystal than within the individual single crystals, but only in cases where void growth is similar — but not equal — in the constituent single crystals.

The plan of this chapter is as follows: In section 4.2 we present the simulations conducted to probe the effect of crystallography on intergranular void growth. The results of a comprehensive study of crystallographic effects on intergranular void growth using LS-EVP-FFT are presented and discussed in section 4.3. Finally, key takeaways of this study and outstanding questions are discussed in section 4.4.

4.2 Simulation setup

The simulations in this chapter were all performed using the large-strain elasto-viscoplastic fast-Fourier transform (LS-EVP-FFT) described in chapter 3. The unit cell with a void is discretized by mapping a cube inclusion to a sphere, as in section 3.3.

To create unit cells with grain boundaries, one or more planes were introduced to split the unit cell into two or three parts. After the spherical void was created, one or more planes were placed through the center of the unit cell at varying angles, and the matrix was split along those planes into grains.

Here we present LS-EVP-FFT simulations intended to probe the growth of voids at and near grain boundaries and triple junctions, to elucidate some of the open questions detailed in the introduction.

Five types of unit cells were used in this work. All cases contained one void at the center of the simulation cell (unless otherwise noted), with these characteristics:

- 3D single crystals with initial 1% porosity, to compare with bicrystal and tricrystal simulations;
- 3D bicrystals, with 1% initial porosity, with the grain boundary passing through the center of the void at varying angles, assigning a selection of orientations to the crystals corresponding to low-energy coherent grain boundaries in FCC systems;
- 3D bicrystals with 1% initial porosity, with a general (non-coherent) grain boundary passing through the center of the void at varying angles;
- 3D bicrystals with 1% initial porosity, with a general grain boundary passing off-center of, or completely missing the void; and
- 3D tricrystals with 1% porosity, with different permutations of a selection of orientations.

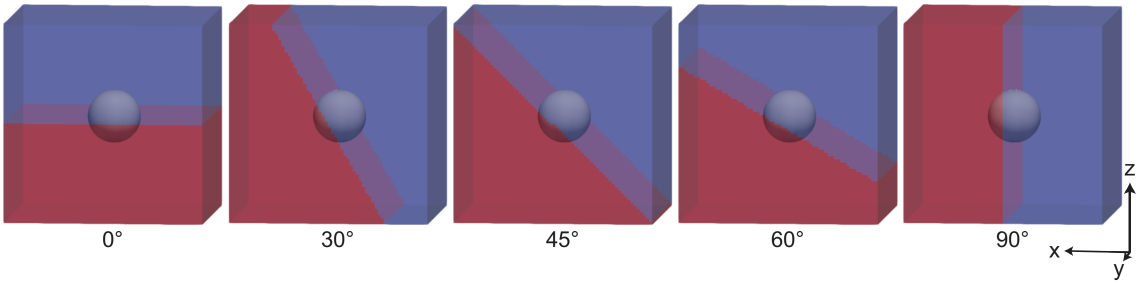

Figure 4.1: The cells for the grain boundary inclination study, with the angles marked below. Here, the void is shown in white, and the first and second grains are shown in blue and red, respectively.

The first set of simulations consisted of 3D single crystals, with dimensions of 64×64×64 and a void placed at the center with diameter 17 voxels (corresponding to the eighth-cell shown in Figure 3.1(c)), resulting in 1% volume fraction of the void. This choice allowed a reasonable resolution while avoiding void interaction with periodic repetitions of the unit cell. The purpose of these simulations was to compare grain boundary results to that of the single crystals

The second set of simulations consisted of 3D bicrystals, with voxel dimensions as in the previous single crystal cases. In these simulations, the material portion of the unit cells were split in half through the center of the void at one of three inclination angles: 0°, 45°, and 90°, where the angle is measured between the plane normal and the z-axis; the plane normal was always perpendicular to the y-axis, and the normal was rotated in the xz-plane (as indicated in Figure 4.1). The orientations were chosen to mimic those of low-energy coherent grain boundaries. The intention of these simulations was to keep misorientation fixed, allowing individual grain crystallography and grain boundary inclination to be isolated.

The third set of simulations consisted of 3D bicrystals identical to the previous set of simulations, but with one of five inclination angles: 0°, 30°, 45°, 60°, and 90°, shown in Figure 4.1. In contrast to the previous simulations, the orientation of the grains were

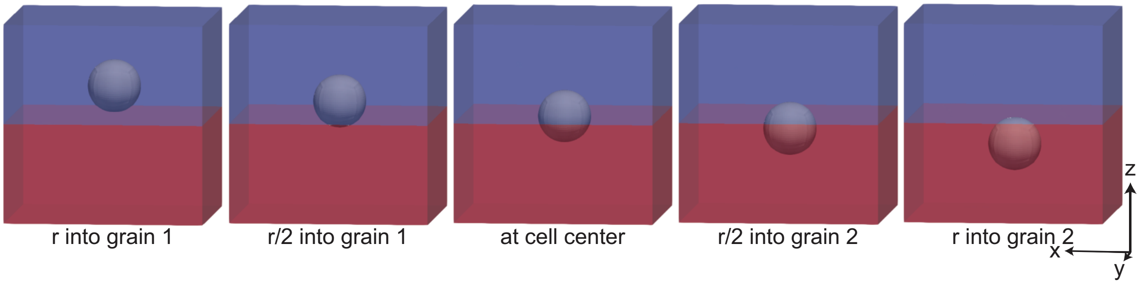

Figure 4.2: The simulation cells for the offset void study. Here, the void is shown in white, and the first and second grains are shown in blue and red, respectively.

fixed to the primary axis of loading. These cases were devised to further probe the effect of grain misorientation and grain boundary inclination on void growth.

The fourth set of simulations were bicrystals identical to the previous cases, but with the void displaced from the center of the cell (while the grain boundary remained coincident with the center of the cell) by $r/2$ or r in the direction of the grain boundary normal, in both positive and negative directions, shifting the initial void position to lie primarily in one grain. Simulations were limited to those with grain boundary normals at 0° (the full combination of offsets shown in Figure 4.2) or 90° to the principal axes (essentially (001) and (100) planes). The intent of these cases was to see if void growth can effectively propagate from one grain to the other, even if the void is formed primarily in the interior of one of the grains forming the grain boundary.

The fifth and final set of simulations was of tri-crystals with identical unit cell dimensions to the previous cases. In these simulations, the material portion of the unit cells were split into three parts along the 30°, 120°, and 90° planes, moving clockwise, from one edge of the unit cell to the center of the void, with plane normals perpendicular to the y-axis (Figure 4.3). The intention of these simulations were to probe non-symmetric combinations of grain orientations, similar to Zhang et al. [66].

All simulations were conducted imposing a stress triaxiality σ_{tx}=3.0, a constant axial strain rate $\dot{\varepsilon}_{33} = 1.0s^{-1}$, and an initial time step, Δt=2×10^{-3}s. In all cases, the FCC

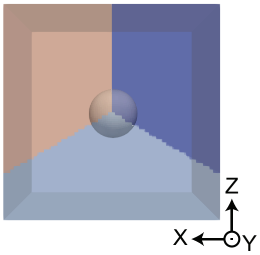

Figure 4.3: The grain structure for the triple junction simulations, with the three grains in light red, light blue and blue.

crystals deform plastically by ⟨110⟩{111} slip, with a reference slip rate $\dot{\gamma}_0$=1.0/s, and, in most cases, a stress exponent n=5 (see Equation 3.14). Notable exceptions to the adoption of this non-linear viscoplastic behavior is the use of a linear viscosity, n=1, to consider a linear viscoelastic material for comparison with Eshelby's analytical stress fields, which are available for linear material behavior. The adopted Voce hardening parameters from Equation 3.16 were τ_0=1.0 MPa, τ_1=3.0 MPa, θ_0=8.0 MPa, and θ_1=0.0 MPa. For the isotropic elasticity constants, Young's modulus and Poison's ratio, ν, were adopted to be 1000 MPa, and 0.3, reflecting the constants used in the FEM in chapter 2.

The overall void volume fraction in the simulation is taken to be the sum of the Jacobian of the deformation of the void voxels divided by the corresponding sum over the entire unit cell, $\sum_{\mathrm{V}} J(\mathbf{x}) / \sum_{\mathrm{M+V}} \mathbf{J}(\mathbf{x})$. To determine the void volume fraction pertaining to each grain in bicrystal or tri-crystal simulations, the 3D coordinates of the nodes in the surface of the void in contact with each grain were extracted and the resulting volume was calculated using a convex hull algorithm (specifically, python's scipy.spatial.ConvexHull package), similar to Jeong et al. [74], which was then divided by the volume of the convex hull of the grain itself. If, for any reason, the sum of volume of the convex hulls did not equate to the total volume of the void, the remaining volume was split in portions (two or three) and added to all of the volumes. In practice, this difference accounted for a small portion of the volume of the bi- or tri-crystals.

Boundary	Tilt/Twist	Misorientation angle	r
$\Sigma3\{111\}\{111\}$	tilt	70.5°	$\langle 110\rangle$
$\Sigma11\{113\}\{113\}$	tilt	129.5°	$\langle 110\rangle$
$\Sigma3\{110\}\{110\}$	twist	70.5°	$\langle 100\rangle$
$\Sigma5\{100\}\{100\}$	twist	36.9°	$\langle 100\rangle$
$\Sigma13\{100\}\{100\}$	twist	22.6°	$\langle 100\rangle$
$\Sigma17\{100\}\{100\}$	twist	28.1°	$\langle 100\rangle$

Table 4.1: Low-energy coherent grain boundaries in the 0-45-90° simulations.

4.3 Results and Discussion

4.3.1 Voids at coherent grain boundaries

We begin our study of voids at grain boundaries with several cases of low-energy coherent grain boundaries in FCC materials. These simulations consisted of a bicrystal with a void in the center of the cell, with the void center coincident with the grain boundary plane at 0°, 45°, and 90°, corresponding to the angle between the plane normal and the z-axis rotated in the xz-plane. The orientations were selected to correspond to one of six low-energy coherent grain boundaries listed in Table 4.1, which is a subset of the relationships reported in Sutton and Balluffi [127]. The orientations of the grains were set to coincide with the normal to the grain boundary (drawn schematically in Figure 4.4 for the $\Sigma5\{100\}\{100\}$ twist boundary). For comparison, single crystal simulations for each of the individual grain orientations were also performed.

Figure 5.5 shows an example of void volume fraction evolution for the $\Sigma5\{100\}\{100\}$ twist grain boundary case. Figure 5.5(a) shows the void volume fraction normalized by its initial value, f/f_0, of the two single crystals (brown solid line and pink dashed line for single crystal 1 and 2) rotated 45° around the y-axis, the entire void in the bicrystal with a 45° grain boundary (black solid line), and the portion of the void in the bicrystal corresponding to one grain or another (brown dotted line for the first grain, pink dot-dashed line for the second), as a function of axial strain, ε_{33}. The vertical

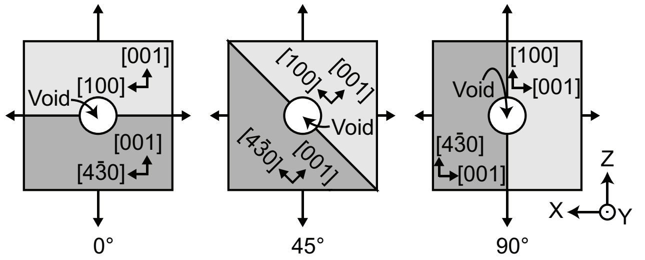

Figure 4.4: A schematic representation of an xz cross-section for the low-energy grain boundary simulations, showing how the $\Sigma5\{100\}\{100\}$ twist boundary rotates with the grain boundary inclination angle. The cells themselves are identical to those shown in Figure 4.1.

dotted line shows the strain (7.26%) at which several important micromechanical field variables are taken from in Figures 5.5(b) and 4.6. Figure 5.5(b) shows the void volume fraction normalized by its initial value, f/f_0, for the single crystals (brown solid line and pink dashed line), entire bicrystals (small black dots), and within each grain in the bicrystal (larger colored dots, filled corresponding to the first grain, open corresponding to the second grain), as a function of grain boundary inclination, θ_{GB}, at the same strain (7.26%). Note that the total volume fraction (black dots) in the bicrystal should be an average of the volume fraction pertaining to each grain in the bicrystal (colored dots), but due to the different calculation methods between the partial and total void volume fraction (detailed at the end of section 4.2), this is not always the case.

Figure 5.5(b) (which is repeated in Figure 4.6(c)) shows one interesting behavior, which is not immediately intuitive. For the 45° bicrystal set, the void appears to grow faster into grain 2, which shows slower growth in the single crystal case. This occurs when the contrast between the single crystals is high. The void is also growing slightly faster in the bicrystal than in either constituent single crystal in the 90° bicrystal set. Contrast in both 0° and 90° bicrystal sets is low.

Figure 4.6 shows the normalized void volume fraction of the single crystal and bicrystal pairs for all of the orientations listed in Table 4.1. The symbols and lines are consis-

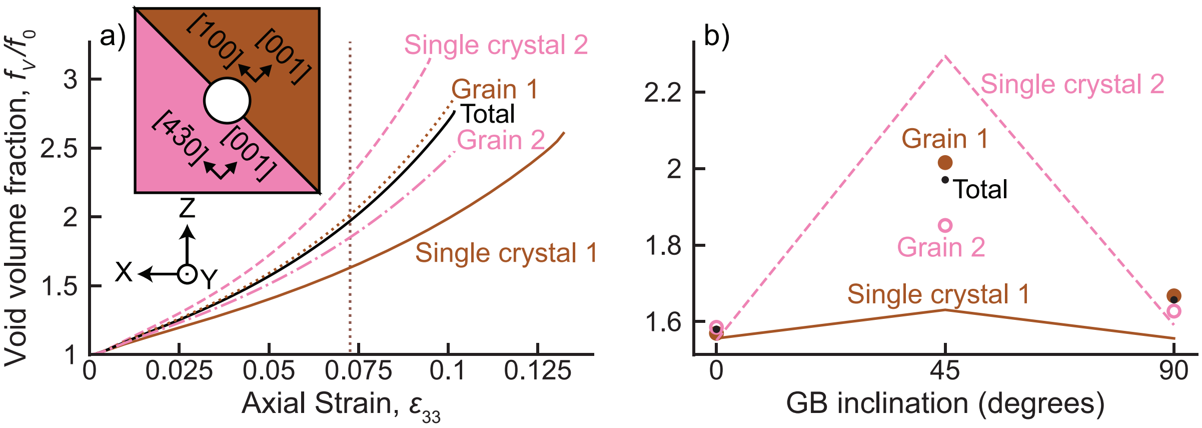

Figure 4.5: Plots of normalized void volume fraction, f/f_0, at $\Sigma5\{100\}\{100\}$ twist grain boundaries grain pairs and in single crystals with the same crystal orientations. (a) shows f/f_0 versus axial strain, ε_{33} for the single crystals (brown solid line for the first grain, dashed pink line for the second grain) rotated 45° around the y-axis and the 45° grain boundary, showing the total void volume fraction (solid black line) of the unit cell as well as the void volume fraction within each grain (dotted and dot-dashed colored lines). The vertical dotted line in (a) indicates the strain at which the values in (b) show the void volume fractions for the single crystals (again, solid and dashed colored lines), the entire unit cell (small black dots), and the individual grains (larger colored dots, filled and open), as a function of grain boundary inclination, where the data points at 45° in (b) correspond to the values taken from (a).

tent with Figure 5.5(b), which is reproduced in Figure 4.6(c). A few trends immediately emerge: First, the voids in the twin boundary (Figure 4.6(a)) essentially behave as single crystals, with very little deviation in void growth in the bicrystal from that of the single crystal. In general, in all other cases of zero contrast, again referring to the difference in void volume fraction between the single crystals, the void growth in the bicrystal is nearly identical to their single crystal counterparts. There are two notable exceptions: The bicrystals in Figure 4.6(b) with the 45° grain boundary and (f) with the 0° grain boundary show much faster growth in the bicrystal than in either single crystal. The second observation is that where there is contrast in the single crystals (typically in the 45° bicrystal sets), the void grows at a rate that is between that of either single crystal. There also appears to be a slight anisotropy in growth in the grains in the bicrystal (c-e, colored dots), and the void grows faster into the grain that showed slower growth as a single crystal. This reversal in growth is not true, however, in the 90° bicrystal in (f), which shows faster growth in the second grain in the bicrystal and faster growth in single crystal form.

While studies with these orientation relationships may prove important from the perspective of creating a database, they do not reveal many underlying trends about grain boundary inclination angle or misorientation. As such, further study of the effects of crystallography is necessary to reveal the relationship. In the following sections, we consider a greater range of orientation relationships and return to the five orientations discussed in the previous chapter in subsection 3.4.3.

4.3.2 Voids at bicrystal grain boundaries

In order to more generally probe the effect of crystal orientation and grain boundary inclination on void growth, we used a variety of grain orientations to simulate bicrystals

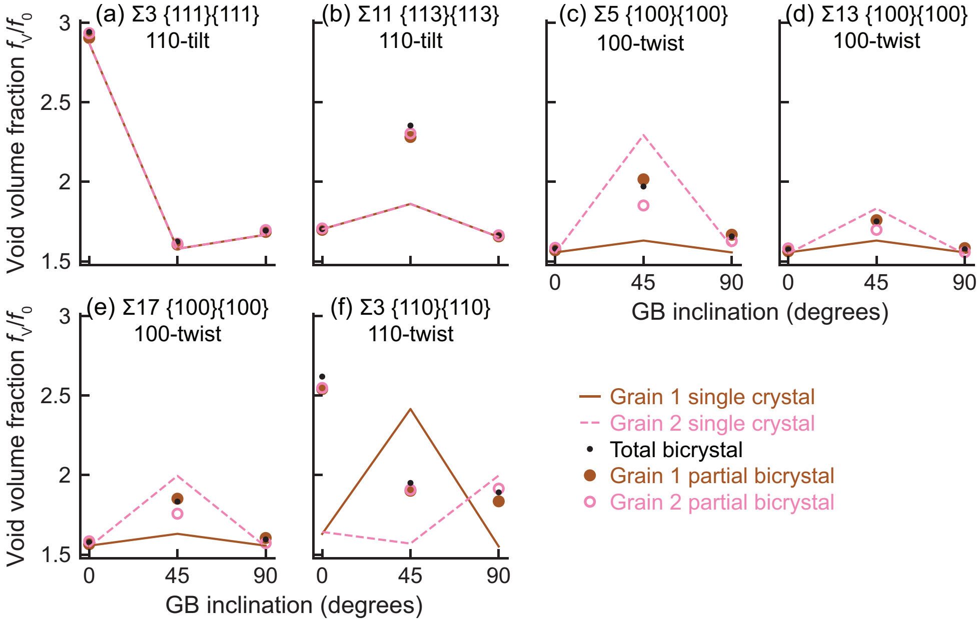

Figure 4.6: Volume fraction at 7.26% axial strain for all single crystals and bicrystals with voids at the center of the unit cell as a function of grain boundary inclination. Each individual plot (a-f) represents a different coherent grain boundary, with the grain boundary designation listed at the top. Colored lines represent single crystal data, and dots represent bicrystal data. Black dots are the total volume fraction in the cell, while colored dots are the volume fraction within each grain. The brown solid lines (single crystals) correspond to the grain orientation of the solid brown circles, while the dashed pink lines correspond to the grain orientation of the open pink circles. The volume fraction is normalized by the initial volume fraction of each population (i.e. 1%). Except for 45° and 0° grain boundaries in (b) and (f), when the voids in the single crystals show no growth contrast, the voids in the bicrystals similarly show nearly identical growth. When there is contrast, as in (c-f), the total void volume fraction in the bicrystal (black) is in between that of the single crystal (lines). At 45° in (c-e), the void in the bicrystal grows slightly faster into the softer grain (filled brown dots).

orientations	letter	Misorientation angle	r
[001]-[011]	(a)	45°	[100]
[001]-[021]	(b)	63.43°	[100]
[011]-[$\bar{1}$25]	(c)	33.69°	$[-0.68, -0.16, -0.86]$
[011]-[021]	(d)	18.43°	[100]
[001]-[111]	(e)	69.73°	$[1.39, -0.58, 1.12]$
[011]-[111]	(f)	45.99°	$[0.29, -0.12, 1.40]$
[111]-[$\bar{1}$25]	(g)	77.04°	$[-0.82, 0.13, -1.76]$
[111]-[021]	(h)	45.79°	$[0.26, -0.11, -1.41]$
[001]-[$\bar{1}$25]	(i)	35.72°	$[0.77, 0.18, -0.86]$
[$\bar{1}$25]-[021]	(j)	47.17°	$[1.20, 0.28, 0.79]$

Table 4.2: Grain pairs studied in the fourth-sixth set of simulations, listing the pair, the Misorientation angle, and the axis of rotation, r.

with a void in the center of the cell, with the grain boundary plane at 0°, 30°, 45°, 60°, and 90°, measuring the angle between the plane normal and the z-axis and rotated in the xz-plane. The simulations were assigned the five previous crystallographic orientations used in subsection 3.4.3, in all possible combinations of grain pairs, with the orientations always fixed relative to the z-axis, in contrast to the previous subsection. The combinations and misorientations are summarized in Table 4.2. The letter designation indicates the order in Figures 4.7-4.10.

Figure 4.7 shows the void volume fraction of voids in single crystals and bicrystals, as a function of grain boundary inclination. Each plot shows the total normalized volume fraction of the void in single crystals, grain-boundary pairs, and individual grains (colored lines, black dots, larger colored dots, respectively), at 8.53% axial strain.

There are several noteworthy observations: First, void volume fraction at this strain generally (the exceptions are discussed shortly) can be described using a reductionist viewpoint: that is, the total void growth in the bicrystal is given by an average of the single crystal growth rates of the constituent grains. Second, the total void growth is insensitive to the grain boundary inclination. Third, in contrast to the total void growth, the individual growth within each grain in the bicrystal is sensitive to grain boundary inclination, which is most notable in high-contrast growth involving the [111]-oriented grains, as in Figure 4.7(e-h).

To further discuss the points made above, we use the terms “emergent” and “anisotropic” growth, which may occur simultaneously. Emergent growth refers to higher total void volume fractions in the bicrystalline unit cells, compared to the volume fractions in each constituent single crystal unit cells at the same strain. This trend is the exception to the previous viewpoint. Emergent growth occurs in some of the low-contrast GBs, namely Figure 4.7(a-d), but not in others, as in Figure 4.7(i-j), regardless of the GB inclination angle. Anisotropic growth refers to unequal growth in grain pairs. An example of this is in Figure 4.7(e), where the void in the bicrystal grows fastest into the [001] grain, whereas the void grew faster in the [111] single crystal. This behavior is always apparent at 0° GBs, and infrequently in 90° GBs, and the void growth in bicrystals with inclined grain boundaries lies between these two states. The void always grows fastest into (colored dots) the grain in the bicrystal that showed slower void growth in the single crystal (line with the same color) when the grain boundary is at 0°-inclination.

One explanation for the anisotropic growth, alluded to in the discussion of the single crystal behavior in Figure 3.6, is the stress state at this strain. Figure 4.8 shows the average stress of the single crystals, grain-boundary pairs, and individual grains (colored lines, black dots, larger colored dots, respectively) at the same strain as in Figure 4.7. The trend observed in the previous figure, where the void grew faster into one grain at one inclination and another grain at another inclination angle is explained to be primarily due to the stress/strain loading state, where the 0° simulation cell can be described as “isostress” and transition to an “isostrain” loading state in the 90° simulation cell, which would resemble the strain-controlled simulations in single crystals in the previous two chapters. This tendency is most apparent in the cells containing [111]-oriented grains, Figure 4.8(e-h). If the grains are subjected to isostress, the voids grow fastest

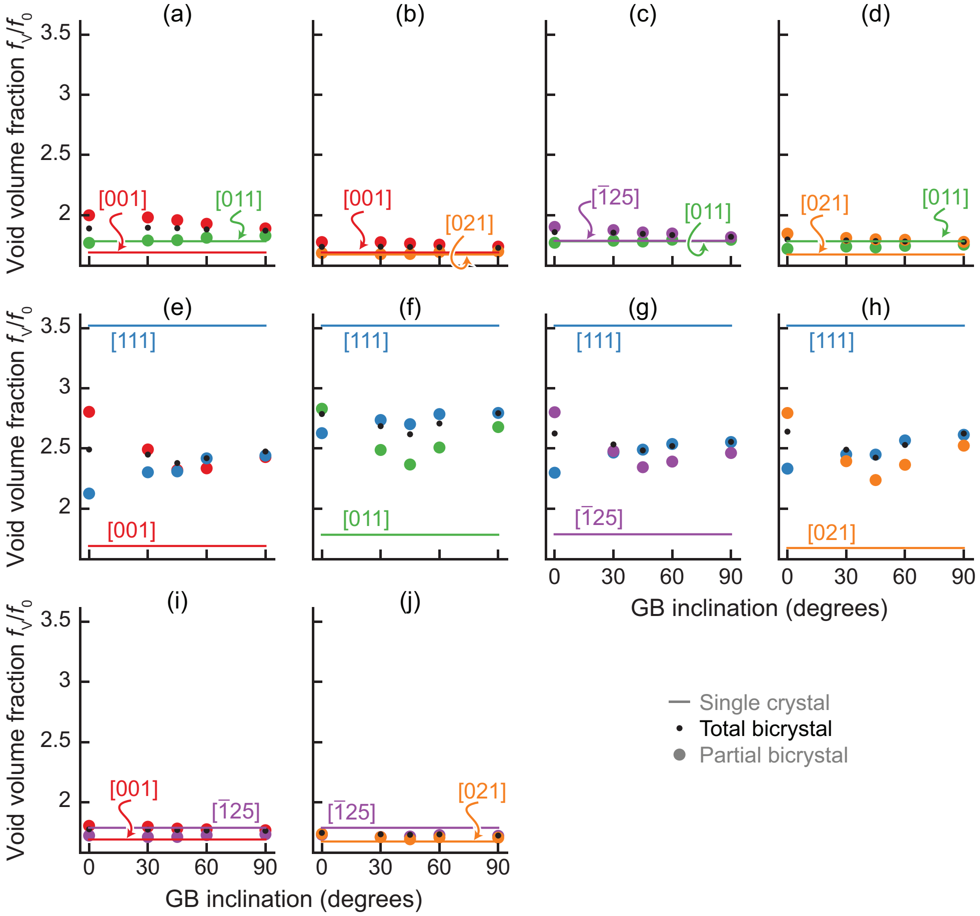

Figure 4.7: Volume fraction at 8.53% axial strain for all single crystals and bicrystals with voids at the center of the unit cell as a function of grain boundary inclination. Each individual plots (a-j) represents a different bicrystal pair, with the two orientations noted in each plot. Colored lines represent single crystal data, and dots represent bicrystal data. Black dots are the total volume fraction in the cell, while colored dots are the volume fraction within each grain. The volume fraction is normalized by the initial volume fraction of each population (i.e. 1%). Figures (a-d) show "emergent" growth, where the total void volume fraction exceeds that of both constituent single crystals. When the grain boundary inclination (GBI) is 0°, voids in bicrystals always have a higher void volume fraction in the grain that showed *less* growth as a single crystal (e.g. in (a), the void volume fraction in the [001] grain is greater than in the [011] grain, while the void grew faster in the [011] single crystal). As the GBI increases, this distinction is diminished, and in some cases (Figures (e-h), all which involve the [111] grain), the void grows fastest in the hardest grain (the [111]-oriented grain).

in the “softer” grain, while the opposite is true in the cases of isostrain, in which the grains that have different average stresses, but similar components of axial strain rate. This trend reflects the observations seen in single crystals with voids; the isostress and isostrain simulations resemble the stress- and strain-rate controlled conditions simulated in chapter 2.

A simplification of this idea is that voids grow fastest with greatest plastic strain. Taylor Factor is typically associated with elevated stresses at the same level of strain, but in reality, the counter-intuitive response is related to the plastic strain: when in isostress loading conditions, the crystal with the softest loading condition experiences the most plasticity, while in isostrain loading conditions, the increased stress necessary to achieve the same strain rate leads to a greater portion of plastic strain near the void.

In addition to the stress, the average maximum slip rate was calculated. The slip rate of each slip system at each voxel was ordered (first, second, third, etc.) and the slip rate at each ordinal position was averaged over the material (excluding the void) and within each individual grain (for the bicrystal simulations). These are now compared, as in previous figures, to see if there are any trends. Figures 4.9 and 4.10 show the averages of the slip rate in the first and second most active slip systems, respectively, at 8.53% axial strain. Focusing on Figure 4.9, the emergent cases (a-d) show a shared trend between the grain-averaged slip rate (colored dots) in the bicrystal compared to its single crystal counterpart: at least one of the grains shows greater slip activity and the second grain shows equal or greater activity. The other cases (e-j) do not consistently show this trend, with one or more grains generally showing reduced slip rates. However, Figure 4.9(f) and (j), which are not emergent cases, show the same increase in maximum strain rate on both halves that is present in the emergent cases, which leads us to look at Figure 4.10 and the second most active slip rate for a pattern.

Figure 4.10 shows the average slip rate in the second-most active slip systems, which

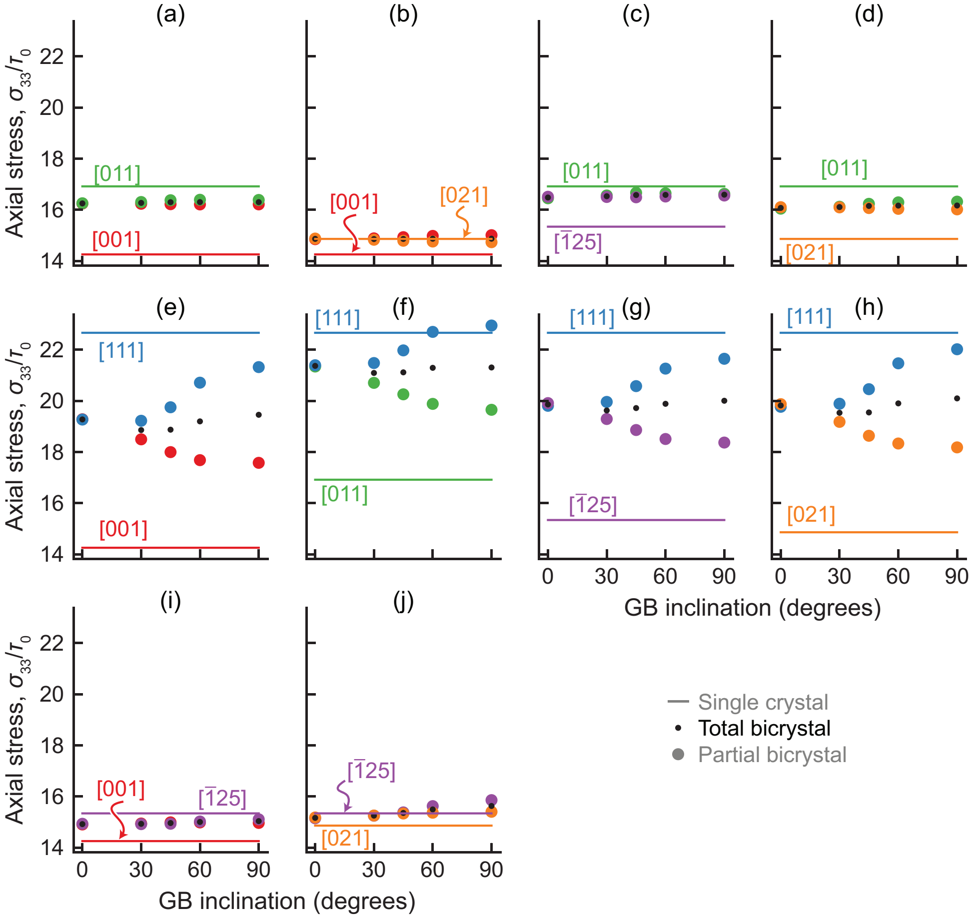

Figure 4.8: Axial stress at 8.53% axial strain for all single crystals and bicrystals with voids at the center of the unit cell as a function of grain boundary inclination. Each individual plots (a-j) represents a different bicrystal, with the two orientations noted in each plot. Colored lines represent single crystal data, and dots represent bicrystal data. Black dots are the total stress in the cell, while colored dots are the stress within each grain (excluding the void, which sustains no stress). It is clear from the figures (e-h), those which involve the [111]-oriented grains, that the 0° and 90° simulations, where stress are equal and most distinct respectively, serve as bounds for all simulations. These two bounds, in essence, mirror stress-controlled and strain-controlled simulations, thus explaining why the growth is fastest in the softer grain for the 0° inclined simulations. Based on stress alone, no figures indicate "emergent" growth, except figure (j), where the stress in the bicrystal simulations in cases with a grain boundary inclination above 45°, the axial stress, and thus von Mises stress, exceeds that of the single crystal constituents.

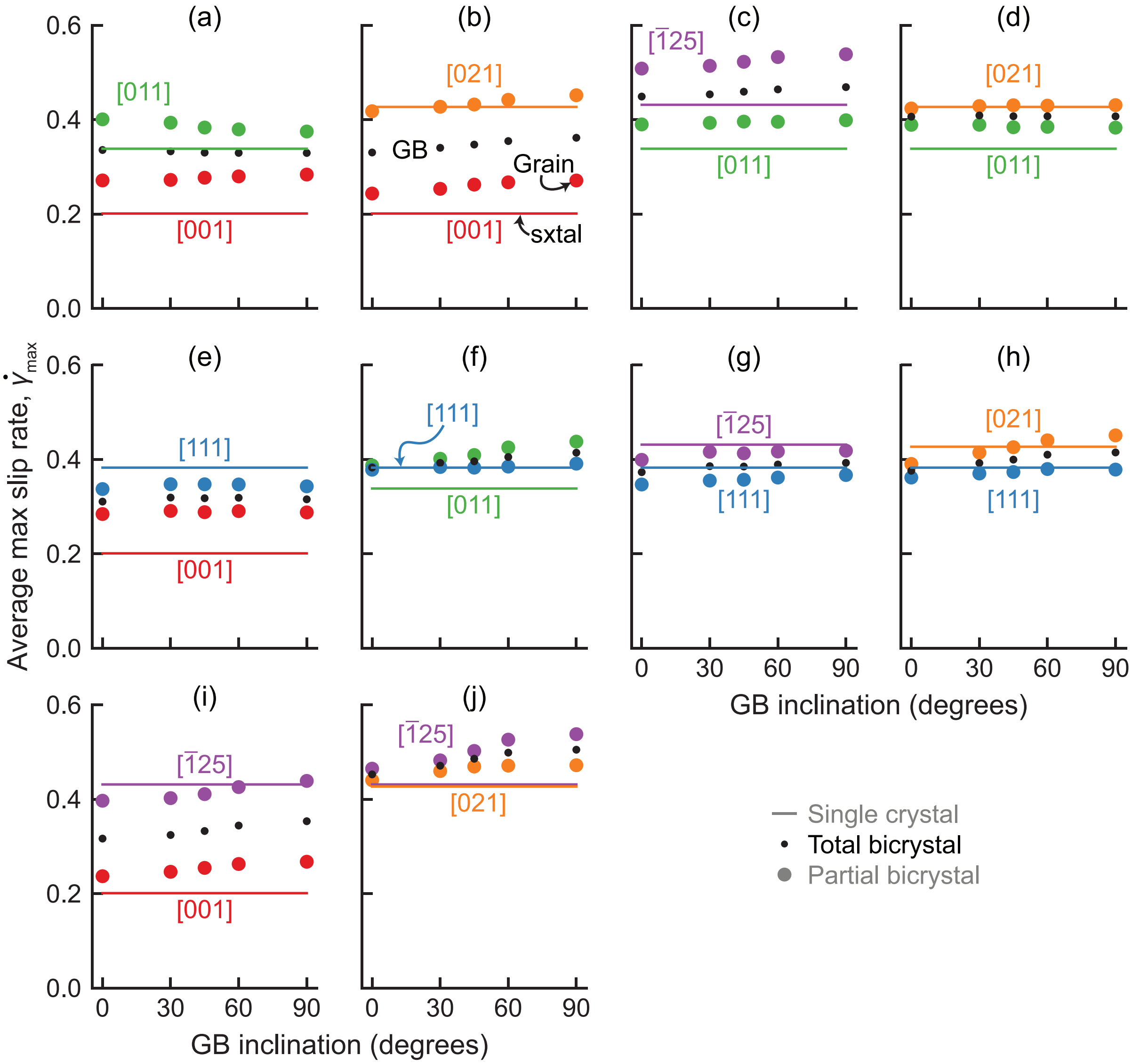

Figure 4.9: Average slip rate of the slip system experiencing largest slip rate at 8.53% axial strain for all single crystals and bicrystals with voids at the center of the unit cell as a function of grain boundary inclination. Each individual plots (a-j) represents a different bicrystal, with the two orientations noted in each plot. Colored lines represent single crystal data, and dots represent bicrystal data. Black dots are the average over all of the material in bicrystal cells, while colored dots are the averages over each grain. In (a-d), the emergent cases, the grains show greater slip than their single crystal counterparts on at least one half, and never show less slip on either half of the bicrystal. The other cases (e-j) do not show this behavior, although (f) and (j) appear to follow the same trend, despite not exhibiting emergent behavior.

provides an additional hint at whether slip is active in multiple slip systems. The single crystal data from Figure 4.9 is shown as dashed lines, to highlight the difference between the most active and second-most active slip systems. Starting from the high-contrast grain cases (e-h), the second-most active slip system shows a slower slip rate (by > 0.15), and the slip rate in the grains is less than that of the single crystal in at least one grain. The bicrystals can be categorized into three groups, where the slip rate is 1) equal or greater in both grain halves, 2) equal or greater in one grain only, or 3) less on both halves. Of the cases that showed an increased slip rate on both halves — shown in Figure 4.9(a-d) and (f) and (j) — the true emergent bicrystals fell into the first two categories in Figure 4.10, while Figure 4.9(f) and (j) fell into the third category where the slip rate is overall decreased in both halves. This indicates that while slip activity may increase in one slip system, plasticity is not enhanced overall. Enhanced slip in multiple slip systems appears to be connected with emergent behavior.

Neither the total stress nor the average stress of the grain halves in the bicrystals indicate that emergent growth would occur; there is no significant elevation of average total stress or an elevation of stress in one grain that would cause the total growth to exceed the growth of both single crystals. However, it is possible that emergent growth is due to a local value near the void. Figure 4.11 shows the axial stress fields, $\sigma_{33}(\mathbf{x})$, at the same strain (8%), in the xz-plane for: (a) emergent [001]−[011], (b) high-contrast [001]−[111], and (c) low-contrast [001]−[$\bar{1}$25] grain pairs. The top row shows the axial stress field in single crystals, the middle row shows the axial stress field in bicrystals with 0/90° grain boundaries, and the bottom row shows the difference between the stress field in the bicrystal and the corresponding single crystalline fields. Compared to the other two grain pairs, the (a) emergent [001]−[011] grain pair shows an increase in axial stress on both halves of the bicrystal, while both the (b) high-contrast and (c) low-contrast pairs show an elevation in stress in the [100] grain, while the [111], and [$\bar{1}$25] grains show

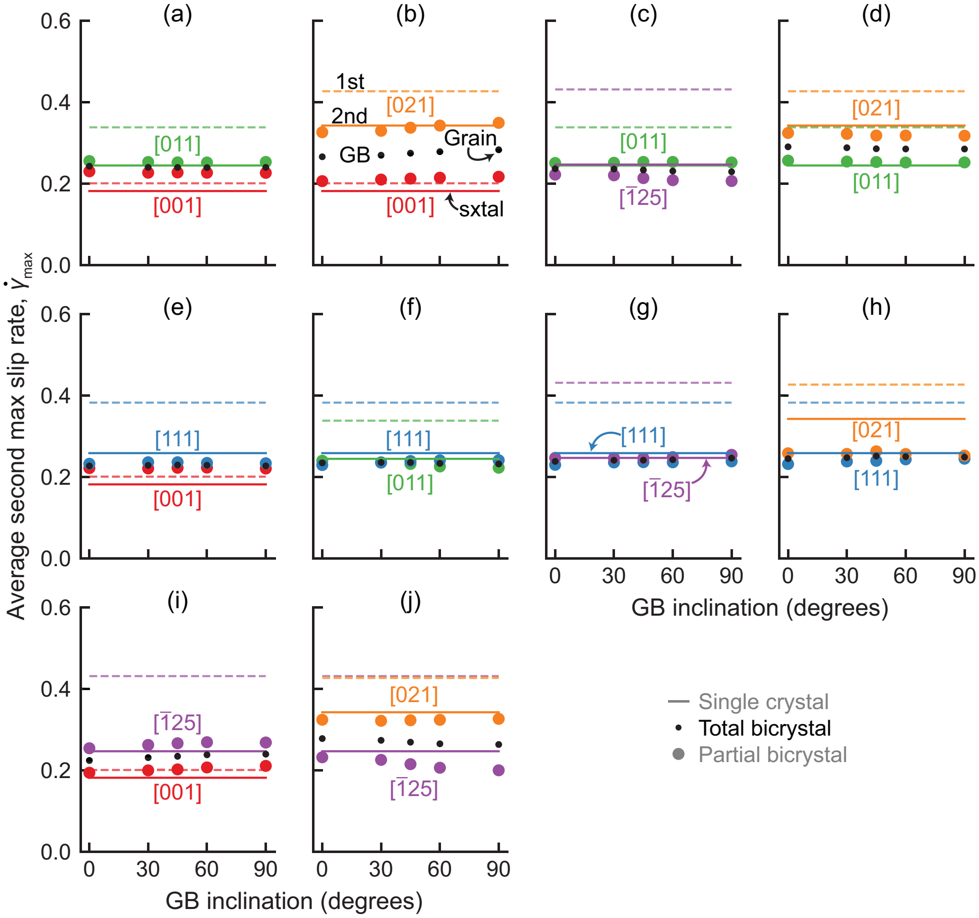

Figure 4.10: Average slip rate of the slip system experiencing the second largest slip rate at 8.53% axial strain for all single crystals and bicrystals with voids at the center of the unit cell as a function of grain boundary inclination. Each individual plots (a-j) represents a different bicrystal, with the two orientations noted in each plot. Colored lines represent single crystal data, and dots represent bicrystal data. The single crystal lines from the previous plot (Figure 4.9) are shown as lighter dashed lines in this plot. Black dots are the average over all of the material in bicrystal cells, while colored dots are the averages over each grain.

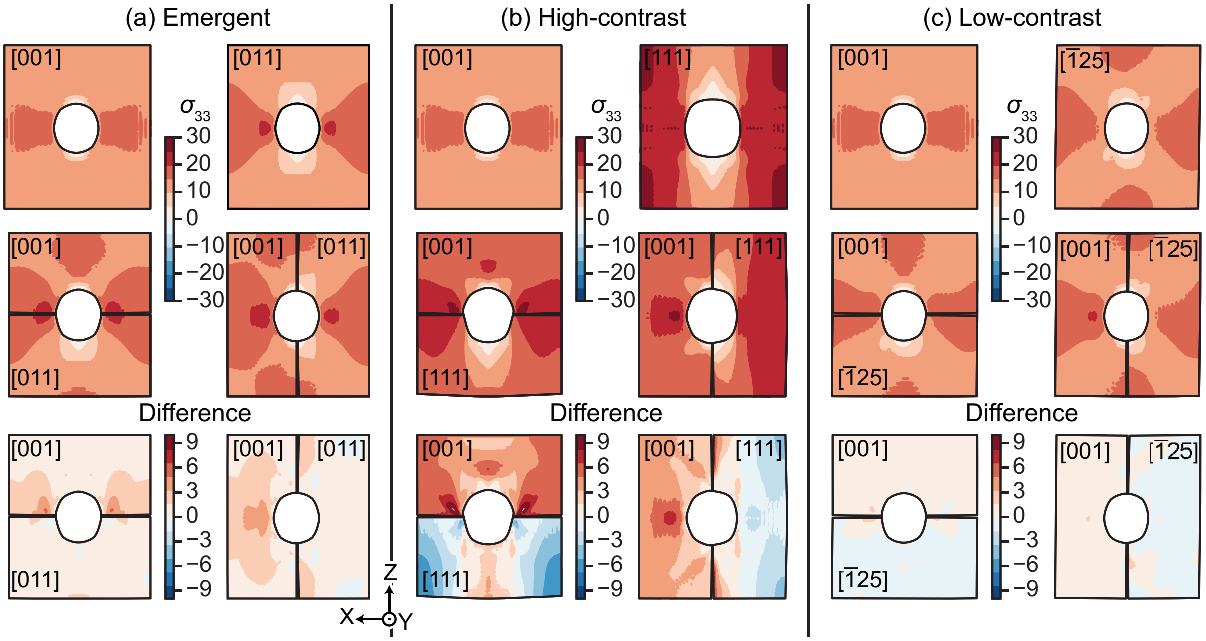

Figure 4.11: Contour plots of axial stress field, $\sigma_{33}(\mathbf{x})$, in various single crystals (top row), bicrystals (middle row), and the difference between the single crystal simulations and bicrystal cells of the same orientation (bottom row). The three orientation pairs are (a) [001]−[011] (left two columns), (b) [001]−[011] (middle two columns), and (c) [001]−[$\bar{1}$25] (right two columns), which represent emergent, high-contrast, and low-contrast simulations, respectively. It is visible from the difference contour plots that the stress on both halves of the bicrystal increase overall in the emergent case, while they increase on the [001] half and decrease on the other half in the reductionist high- and low-contrast cases.

suppressed stress values. The stress elevation is the likely reason for emergent growth, but it remains unclear why that pairing leads to this elevation.

Overall, the effect of crystal orientation on void growth overshadows grain boundary inclination or misorientation from a purely mechanical perspective. It is important, however, to note that with a different Lode parameter or boundary condition the trends may be completely different. From the perspective of growth within a grain (partial growth), grain boundary inclination and misorientation play larger roles. Ultimately, it is plasticity that dictates void growth, as expected. It is possible that with anisotropic elasticity, orientations that are stiffer might behave like materials that are plastically soft, or plasticity may initiate at the same stress and no discernible difference may result.

It was expected that the grains would behave like composite systems as a whole. The anisotropic growth, especially in the iso-strain conditions, where void growth is sometimes faster in the harder crystal, indicates one possible reason that voids may be found primarily in those grains in ex-situ studies. It is also important to note that void growth (and thus coalescence) may occur at a greater rate, due to the emergent void behavior that causes the areas around the void to have elevated stresses relative to their single crystal counterparts. It still remains unclear why some grains show this behavior.

4.3.3 Voids near bicrystal grain boundaries

In this section, the bicrystal was modified to see if the location of the void relative to the grain boundary affects void growth. In these simulations, the void was displaced from the center of the cell by $r/2$ or r in the direction of the grain boundary normal, in both positive and negative directions. Simulations were limited to those with grain boundary normals at 0° (our "isostress" case) or 90° to the principal axes (the "isostrain" loading condition), and only with grain pair combinations of the [001], [011], or [111] orientations.

Figure 4.12 shows the void volume fraction at the single crystals and bicrystals in this study. As in the previous section, colors are consistent among orientations, and the diagrams indicate the initial location of the void, as well as the orientation of the grain boundary. Whether the void lies partially or fully within one grain or another, the total void growth differs only slightly, while the void continues to grow fastest in the grain it is placed.

These simulations can be thought of as a "preview" of future void growth from the simulations where there is no offset: If the void grows most quickly into one grain, it will continue to grow into that grain. If it is fully embedded in one grain, the void does not grow into the soft grain. Thus, if ex-situ results indicate that voids exist more in one grain, it is possible that there was either a micromechanical impulse (based on loading state) into that grain after forming evenly on both sides of the grain boundary, or that the void started in that grain, but close to the grain boundary. Macroscopic loading conditions may affect this impetus.

4.3.4 Voids at triple junctions

To see if the observations and principles of the bicrystal cases apply to more complicated grain junctions, tri-crystals with grains split evenly into three parts were also studied. Every possible permutation of the five orientations were simulated.

Figure 4.13 shows the void volume fraction for the tri-crystals consisting of a (a) [001]−[011]−[111] tri-crystal and [001]−[011]−[$\bar{1}$25] crystal. The figures show the single crystal void response (solid colored lines) and the total (black x's) and partial (colored dots) void volume fraction in the tri-crystals. Here, we see more variation in total void growth, which is dependent on the grain in the horizontal-most position at the bottom of the cell, as shown in (c). While individual grain void volume fraction varies with the location of the other two grains, it is the grain that occupies this position that dictates the stress in the lower half - since it most resembles the 0° isostress grain boundary. The void shows emergent growth at the low-contrast triple junction. The presented tri-crystal simulations reinforce the notion that these behaviors of anisotropic growth, emergent growth, and grain orientation dictating the total void growth extend to more complex grain configurations.

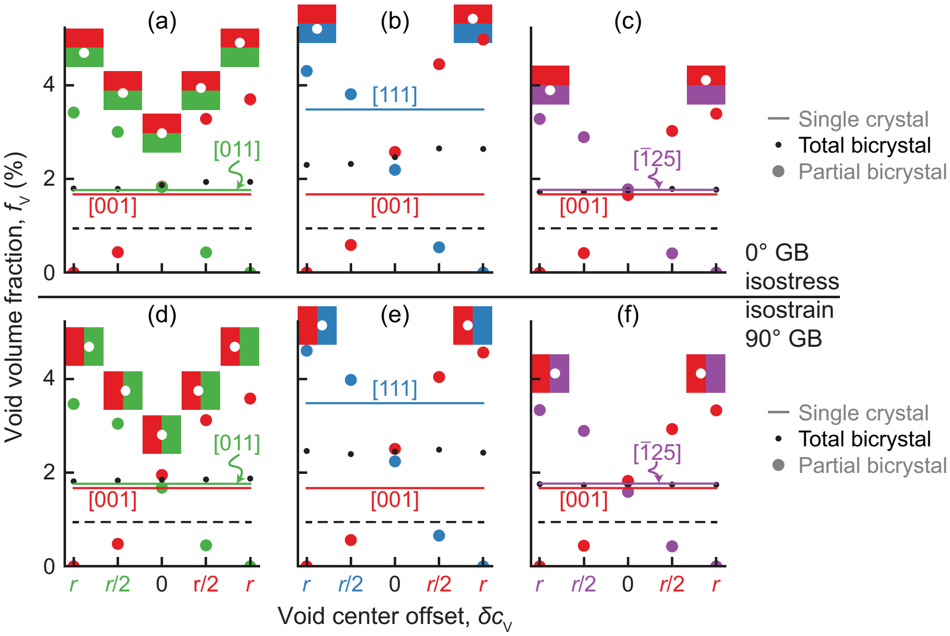

Figure 4.12: Void volume fraction at 8.53% axial strain for all single crystals and bicrystals as a function of the initial distance of the void center from the grain boundary plane. Each column represents a different bicrystal pair, with the two orientations noted in each plot. The top row (a-c) correspond to bicrystals with 0° grain boundaries, while the bottom row (d-f) correspond to bicrystals with 90° grain boundaries. Colored lines represent single crystal data, and dots represent bicrystal data. Black dots are the total void volume fraction in the cell, while colored dots are the void volume fraction within each grain. Colored text indicates the grain the void has been shifted into. The void volume fraction is *not* normalized by the initial volume fraction of each population, but the initial void volume fraction of the total cell (1%) is indicated in the dashed line. In general, voids placed in one grain over another, regardless of the primary loading state (0/90° grain boundary inclination angle) continue to grow fastest in the grain it was placed, although the growth rate is slightly faster when the void is placed in the soft crystals. Figure (a) indicates that the emergent grains continue to be emergent, even in the movement of the void center.

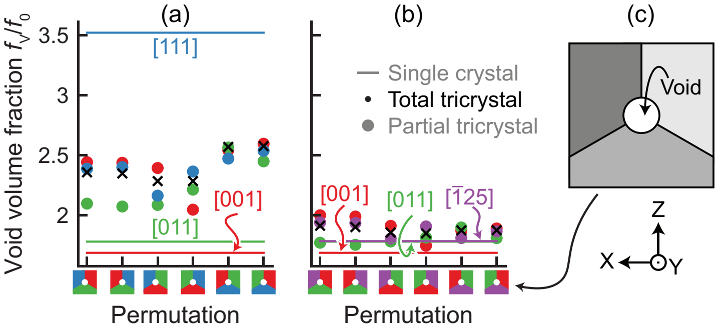

Figure 4.13: Volume fraction at 8.53% axial strain for all single crystals and tri-crystals with voids at the center of the unit cell as a function of grain orientation permutation (depicted as labels on the x-axis, based on the cross section shown in (c)). (a) and (b) show a different grain trio, with the orientations noted in each plot. Colored lines represent single crystal data, and x's and dots represent tri-crystal data; black x's are the total volume fraction in the cell, and colored dots are the volume fraction within each grain. The volume fraction is normalized by the initial volume fraction of each population (i.e. 1%). The total void volume fraction is highly dependent on which grain is in the bottom horizontal position, with negligible variations (as expected) for changes in the other two positions.

4.4 Summary and Conclusions

In this chapter, we used the large-strain elasto-viscoplastic fast Fourier transform-based formulation described in the previous chapter to investigate crystallographic effects on the growth of voids at or near grain boundaries and triple junctions. Neglecting void nucleation and coalescence, several sets of simulations were conducted on a generic FCC metal as a model material, with various combinations and permutations of crystal orientation and grain boundary inclination. Bicrystals with 1% initial void volume fraction and various crystal orientations, corresponding to low-energy coherent grain boundaries in FCC metals, and several grain boundary inclinations were simulated and compared to single crystal void volume fractions with the same subset of orientations. Also, bicrystals with fixed orientations relative to the primary loading axis were simulated, to understand the effect of individual grain orientation, and to probe certain patterns apparent in the previous simulations. Next, bicrystals with voids at different locations relative to the grain boundary were studied. The study that followed focused on voids at triple junctions, with different permutations of the original orientations studied.

From these studies, several trends emerged. First, voids at grain boundaries grow anisotropically: Voids always prefer "softer" (low Taylor factor) orientations for stress-controlled/isostress loading conditions, but in some cases prefer "harder" grains when the grain boundary inclination leaves the grains in strain-rate-controlled/isostrain loading. In this work, the isostress and isostrain conditions were achieved when the grain boundary plane normal was aligned and perpendicular with the loading direction. Thus if voids exist at the grain boundary but primarily in a "hard" grain, then what is likely happening is that the grain boundary inclination is promoting stress-bearing in the "hard" grain.

Secondly, the crystallographic orientation of constituent grains relative to the loading axis, not the misorientation or grain boundary inclination angle, is the most significant variable in promoting or suppressing total void growth at grain boundaries.

Additionally, there are a set of orientations that result in "emergent" behavior, where the total void growth in the bicrystalline unit cells is faster than void growth of constituent single crystal unit cells. Emergent behavior is due to local stress/strain enhancements on both halves of the bicrystal relative to the single crystal constituents.

If voids grow anisotropically, we find that they continue to grow faster in those grains. Similarly, if voids initiate primarily in one grain but near the grain boundary, it is likely they will remain in that grain.

Chapter 5

Voids at phase boundaries

5.1 Introduction

The crystal orientation of each grain in a polycrystal plays a role in plastic deformation, since plastic slip occurs on discrete planes in crystallographic directions [128]. Behaviors that are plastically mediated are, thus, dependent on crystal orientation. One such plastically mediated failure mechanism is ductile failure, wherein voids nucleate, grow, and coalesce [34, 38]. Study in the role of crystallographic aspects, such as crystallographic orientation, grain boundary or phase boundary plane, on each stage of ductile failure are areas of intense research. Ex situ studies have demonstrated that voids form at grain boundaries in high-purity FCC and BCC polycrystalline metals and that the GB inclination angle plays a role in void nucleation [7, 30]. Certain studies have suggested that voids tend to appear near grain boundaries with normals parallel to the loading direction [6]. Francis et al. [7] observed that in spalled Ta, the voids at the grain boundaries tended to lie in one grain over another, but the voids preferred to form at the grain boundaries, triple junctions, or quadruple points. Voids in biphase metals tend to form near the phase boundaries, although voids may not form directly or evenly at the phase interface in most cases [8, 129].

However, studies demonstrating the locations of voids [6, 19, 30, 120, 130] often do not monitor the stages of nucleation, growth, and coalescence of voids. Valuable information is lost in ex situ studies with respect to the location of the initial nucleation and growth of the void because coalesced voids often span multiple grains [8, 30, 34, 114, 130]. In situ studies remain difficult to conduct, due to either the extremely high rate of deformation rate which exceeds the monitoring capabilities of methods that are able to track full 3D data sets with both void morphology and crystal orientation information, or due to the specialized equipment to carry out such monitoring [96, 97]. This difficulty has led to extensive research on the progress of ductile damage through analytical or computational methods.

Molecular dynamics (MD) simulations have also demonstrated that voids form at grain boundaries in high-purity polycrystalline metals and that the GB inclination angle plays a role in void nucleation [30, 55, 64]. Nucleation of voids has been found to favor grain boundaries with normals parallel to the loading direction [64]. MD also indicates the formation of voids within each phase, in regions with a high number of defects, as well as at the phase boundaries [131, 132]. While MD as a computational technique is important and appropriate for understanding void nucleation, it is not appropriate for larger length scales, and is generally not used to understand the crystallographic effects of void growth. A notable example of a void growth study (as opposed to a nucleation study) was that of Zhang et al. [66], who used MD to study already nucleated voids at triple junctions in a Ni film. They used only three crystal orientations and swapped the location of those three grains, and found that changing the location of the grains had an impact on both morphology and void growth rate. To the authors' knowledge, there are no MD studies focusing on the growth of already nucleated voids at phase boundaries.

Several micromechanical and crystal plasticity (CP) simulations in the literature have sought to understand the growth of voids in crystalline metals. These studies have shown that crystallography plays a key role in the growth of intragranular voids [2, 50, 52, 121–123]. A smaller number of crystal plasticity finite element (CP-FE) simulations have focused on intergranular voids [51, 72, 74, 124, 126]. Dakshinamurthy et al. [72] simulated voids in bicrystals and found that the voids grew faster into the softer grain, particularly at high triaxialities. Liu et al. [124] showed that voids in bicrystals with a grain boundary direction parallel to the tensile axis are likely to fail by transgranular fracture, while those with tilted (45° from the loading axis) grain boundaries are likely to fail by intergranular fracture. Wen and Yue [126] found that high stresses and high stress gradients were apparent near the grain boundary in Ni superalloys, particularly near the void, depending on the orientation of the crystal relative to the primary axis of loading. Chen et al. [51] investigated how misorientation and the character of the grain boundary affected the growth of the void in Ni-based superalloys and found that when paired with a [001] single crystal, the twist boundaries promoted the growth of the void, while the tilt boundaries had the opposite effect in stress-controlled simulations. Jeong et al. [74] simulated bicrystals and tricrystals, showing that the growth rate of voids at the grain boundaries contradicted the order of growth rate in single crystals, related to the differences in stress in each grain. The growth of voids at phase boundaries remains mostly unexplored by CP studies. To the author's knowledge, only Asim et al. [73] have completed simulations of void growth at phase boundaries using CP-FE. In their work, they studied void growth in FCC-hexagonal close-packed (HCP) bicrystals using CP-FE, varying the PB inclination, while keeping the HCP crystal orientation fixed to the normal of the PB. This then conflated certain results of the study of PB inclination with those of crystal orientation.

There are few studies that track void growth using CP fast-Fourier transform models [90], which has the advantage of being more computationally efficient than its CP-FE counterpart, but only recently had the ability to accurately represent the geometry of initially spherical voids. In chapter 2 the dilitational viscoplastic fast-Fourier transform (DVP-FFT) model of Lebensohn et al. [90] was used to study voids fully embedded in single crystals and grains in a polycrystal to the effect of crystal orientation on void growth. It was demonstrated that the loading condition affected the interaction between the growth of the void and the orientation of the crystal. In strain-rate controlled simulations with axisymmetric loading and fixed stress triaxialities, voids grew more quickly in the interiors of the FCC single crystal with the highest Taylor factor, a value that is associated with how plastically "hard" or "soft" a crystal is oriented relative to its primary loading axis. The opposite was true for stress-controlled simulations: The voids grew more quickly in the crystal with the lowest Taylor factor. In this context, "soft" refers to a plastically soft orientation, either due to a lower initial flow stress or due to its orientation showing greater slip at equivalent stresses. Moving to void growth at grain boundaries, chapter 4 used a modified version of the large-strain elastic-viscoplastic fast-Fourier transform (LS-EVP-FFT) model of Zecevic et al. [89], which incorporates elasticity and allows for the geometrically accurate representation of a spherical void, to simulate voids at the GB of FCC bicrystals and tricrystals, and showed that the apparent reversal of void growth rates when placed at the GB observed by Jeong et al. [74] was due to the simulation cell mimicking the stress-controlled simulation of the DVP-FFT study. Specifically, it was observed that in biphase cells where both grains were under the same stress ("isostress"), the void showed anisotropic growth and preferred to grow into the grain that was softer. In biphase cells where both grains experienced the same strain rate ("isostrain"), either no anisotropy of void growth was apparent or the void slightly preferred to grow into the harder grain. These states were achieved by rotating the GB without changing the grain orientation relative to the primary loading axis. Furthermore, some voids showed emergent growth, which was the label given when the voids at the bicrystal grew faster than within either constituent crystal, due to elevated slip on both sides of the GB. This behavior occurred independent of the GB inclination, which weakly affected the total growth of the void in the bicrystal.

The work in this chapter aims to elucidate the crystallographic effects of crystal orientation, PB orientation relationship, and PB boundary inclination on void growth. This work is a continuum-level approach that is interested in voids already nucleated at phase boundaries. A secondary goal is to expand on the work completed on the growth of voids in single-phase bicrystals completed int the previous chapter and understand how the introduction of new slip modes and material differences in hardening affect the behavior of voids. There are two underlying questions motivating this work, particularly in comparison to void growth single-phase bicrystal: Firstly, is there a subset of bicrystal orientations at which voids grow faster in the PB than within the individual single crystals, breaking the void growth expected and observed for most grain orientations, which generally lies between that in the constituent single crystals? Second, given a void formed at the PB, are there some crystal orientations, PB inclinations, or orientation relationships that foster growth, either overall or within one grain?

To answer these questions, we consider an isolated void at a PB, far from any other neighboring grains, phases, or voids. We use a LS-EVP-FFT formulation [89] to simulate the growth of voids in bicrystals with varying PB inclination, orientation relationship, and crystallography. Two material systems are explored: A model FCC/BCC material with identical properties besides the slip modes available, and a biphase FCC Cu/BCC Ta metal. The first case deals with two common orientation relationships in FCC/BCC metals, namely the K–S and N–W orientation relationships, followed by a larger study of grain orientation, similar to that of the previous chapter, to see how the voids in the two material systems compare with those at simple grain boundaries. The simulations presented here demonstrate that the choice of slip mode availability in BCC metals, whether by the 12 ⟨111⟩{110} slip systems, the 12 ⟨111⟩{112} systems, or all 24 slip systems combined, does not significantly affect the behavior of voids at PBs. However, the distinct hardening characteristics exhibited by actual BCC and FCC metals profoundly influence the observed patterns of void growth. Similarly to the single-phase bicrystals in previous work, there exists a subset of bicrystal orientations at which voids grow faster in the PB than within the individual single crystals, breaking the rule of mixture growth. However, the subset of orientations in biphase materials is not necessarily the same as in single-phase FCC bicrystals and differs between the model and specific material systems. By varying both PB inclination and crystal orientation separately, we were able to show that the PB inclination may affect how quickly the voids grow into one grain or another, but does not impact the overall growth of a void to the same extent the crystal orientation does.

The plan of this chapter is as follows: In section 5.2, we describe the simulations conducted to probe the effect of crystallography on interphasic void growth using the modified LS-EVP-FFT numerical method described in chapter 3. The results of a comprehensive study of crystallographic effects on void growth in generic FCC/BCC bicrystals and Cu/Ta bicrystals are given in section 5.3. The implications of these results are discussed in section 5.4, and the concluding remarks and remaining questions are presented in section 5.5.

5.2 Simulation setup

The simulations in this chapter were all performed using the large-strain elasto-viscoplastic fast-Fourier transform (LS-EVP-FFT) described in chapter 3.

Three types of simulation setups were used to understand the growth of voids at phase boundaries. The first set of simulations was a single crystal without voids with voxel dimensions of 4×4×4 and no applied conformal gradient, used to demonstrate the behavior of the phases and material systems prior to the introduction of a void.

All remaining simulations contained a void in the center of the simulation cell. They can be split into two categories, 3D single crystals and bicrystals. The discretization of the voided unit cells in this work follows the algorithm described in Appendix B of Zecevic et al. [89], using the equations to map a 3D cube inclusion or heterogeneity in the reference configuration to a spherical inclusion/heterogeneity in the initial configuration in section 3.3. The algorithm optimizes the position of the centers of each voxel on the surface of the void to improve the representational accuracy of the shape of the void. The positions of the remaining voxels in the unit cell were interpolated using the optimized locations of the boundary voxels.

All void simulations were performed with an initial 1% volume fraction of the void, which balanced resolution while avoiding void interaction across periodic repetitions of the unit cell.

The first type of simulation with a void consisted of 3D single crystals, with dimensions of 64×64×64 and the void placed in the center with a diameter of 17 voxels, shown as an eighth cell in Figure 5.1 (a). These simulations serve as a basis for comparison to the bicrystalline simulations.

The second type of void simulation consisted of 3D bicrystals, with voxel dimensions as in the previous single-crystals. For these simulations, after creating the spherical void, a plane was placed through the center of the unit cell at one of three orientation angles (0°, 45°, and 90°), and the matrix was split along those planes into grains. The angle of inclination of the phase boundary is indicated by the angle between the plane normal and the z-axis; the plane normal was always perpendicular to the y-axis, and the normal was rotated in the xz-plane (as indicated in Figure 5.1).

Two sets of orientations were used for these two voided unit cells. The first set of

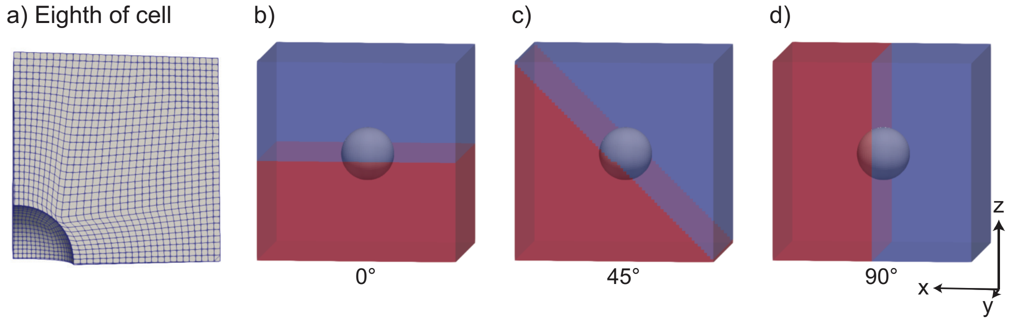

Figure 5.1: (a) Eighth cell of the 3D unit cell that was used for single crystal and bicrystal simulations, and (b-d) the cells for the GB inclination study, with the inclination angles of (b) 0°, (c) 45°, and (d) 90°. In these three cases, the void is shown in white, and the FCC and BCC phases are shown in blue and red. The initial volume fraction of the void was 1%.

OR	Planes	Directions
K–S	$\{111\}_{\text{FCC}} \parallel \{011\}_{\text{BCC}}$	$\langle\bar{1}01\rangle_{\text{FCC}} \parallel \langle 1\bar{1}1\rangle_{\text{BCC}}$
N–W	$\{111\}_{\text{FCC}} \parallel \{011\}_{\text{BCC}}$	$\langle 1\bar{1}0\rangle_{\text{FCC}} \parallel \langle 100\rangle_{\text{BCC}}$

Table 5.1: Orientation relationships for FCC/BCC used in biphase simulations. The single crystal orientations corresponding to these orientations were also simulated, for completeness.

orientations correspond to K–S and N–W orientation relationships, chosen to keep the misorientation fixed, allowing individual grain crystallography and GB inclination to be studied, and are summarized in Table 5.1. For these simulations, the three PB angles 0°, 45°, and 90°, were used. The orientation of the grains was set to coincide with the normal to the PB (drawn schematically in Figure 5.2). Single-crystal simulations with each of the individual phase orientations relative to the primary loading axis in the z direction were also simulated.

The second set of orientations used combinations of five orientations used in the previous two chapters to decouple the effects of crystal orientation and PB inclination on void growth in FCC/BCC bicrystals. The orientations chosen are as follows: [100]-[010]-[001], [100]-[01$\bar{1}$]-[011], [1$\bar{1}$0]-[11$\bar{2}$]-[111], [210]-[1$\bar{2}$1]-[$\bar{1}$25], [100]-[01$\bar{2}$]-[021], all strained primarily in the z axis (the third direction). From this point on, only the orientation

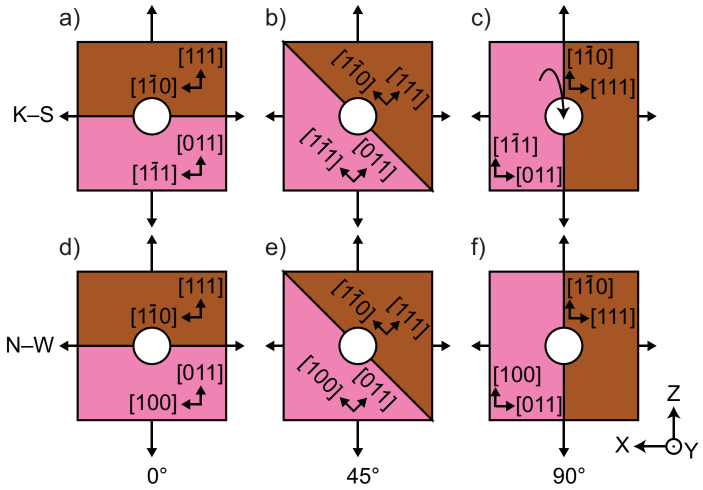

Figure 5.2: A schematic representation of an xz cross-section for the orientation relationship simulations. (a-c) The orientations for the Kurdjumov–Sach (K–S)-orientation relationship, and (d-f) the orientations for the Nishiyama–Wassermann (N–W)-orientation relationship simulations. Brown is used for the FCC half of the bicrystal, and pink represents the BCC half. The cells themselves are identical to those shown in Figure 5.1.

relative to the primary z axis will be listed to indicate the crystal orientation, i.e. [001], [011], [111], [$\bar{1}$25], and [021], respectively. Single-crystal, single-phase simulations with these same five orientations were also conducted as a basis for comparison. For this second set of orientations, only the 0° and 90° PB inclination angles were used, since in the previous study of grain boundaries, these served as bounding cases between the loading states of isostress and isostrain in each grain.

Throughout this work, for every bicrystal simulation run, two single crystal calculations were run. In cases where the unit cell is referenced, the word "crystal" is used, either for the bicrystal or isolated single crystal unit cell. For clarity, if the variable pertains to one of the two grains in a bicrystal simulation, the word "grain" is used. In no instance does "crystal" refer to one of the halves of the bicrystal simulation.

All simulations were conducted imposing a constant axial strain rate $\dot{\varepsilon}_{33} = 1.0s^{-1}$, and an initial time step, Δt=2×10^{-3}s. The imposed stress triaxiality, σ_{tx}, of the void-free single-crystal simulations was 1/3, corresponding to the uniaxial stress. For the voided simulations, σ_{tx}=3.0.

Two sets of BCC-FCC materials were used: The first, a model FCC/BCC pair was used to probe the effect of slip mode selection on void growth at phase boundaries, and a Cu/Ta pair which more accurately captures the distinct hardening behavior of the two phases. The FCC crystals deform plastically on the 12 $\langle 110\rangle\{111\}$ slip systems, while the BCC crystals deform plastically on the 12 $\langle 111\rangle\{110\}$ slip systems, the 12 $\langle 111\rangle\{112\}$ slip systems, or by both modes of slip (24 slip systems). For simulations of the model FCC/BCC, the reference slip rate and stress exponent in Equation 3.14, are $\dot{\gamma}_0$=1.0 and n=5, respectively. The Voce hardening parameters adopted from Equation 3.16 were τ_0=1.0 MPa, τ_1=3.0 MPa, θ_0=8.0 MPa, and θ_1=0.0 MPa. For the isotropic elasticity constants, Young's modulus and Poison's ratio, ν, were 1000 MPa and 0.3, reflecting the constants used in CP-FE in chapter 2 and LS-EVP-FFT in chapter 3 and chapter 4. The self- and latent hardening coefficients, $h^{\alpha\alpha}$ and $h^{\alpha\alpha'}$, were both unity. For Cu and Ta simulations, constants were taken from Chockalingam et al. [133] and Feng et al. [134], and are listed in Table 5.2, next to the model FCC and BCC constants in the first column. The mechanical response of Ta with the three slip mode options are shown for single crystals without voids in subsection 5.3.1, but all simulations of Ta with voids use the combined $\langle 111\rangle\{110\}$ and $\langle 111\rangle\{112\}$ slip systems.

Figure 5.3 shows the flow stress in each slip system as a function of the total slip, $\sum_\alpha \gamma^\alpha$, normalized by the FCC and Cu initial flow stress, τ_0^α, for the FCC and Cu materials for the FCC/BCC and Cu/Ta systems, respectively. The BCC and FCC systems have the same Voce hardening parameters, and as such the flow stress curve is identical. The Cu curve may have a lower initial value, but it hardens very quickly, surpassing the flow stress of the Ta. A well known distinction between FCC and BCC metals is that FCC undergoes strain hardening, and BCC does not. The Cu/Ta system is a classic case

Parameter	model FCC and BCC	Cu	Ta
C_{11} (GPa)	1.346	168.4	268.5
C_{12} (GPa)	0.577	121.4	159.9
C_{44} (GPa)	0.385	75.4	87.1
n	5	10	14
$\dot{\gamma}_0$	1.0	0.001	0.001
τ_0	1.0	60.8	115.0
τ_1	3.0	109.8	50.0
θ_0	8.0	541.5	120.0
θ_1	0.0	0.0	5.0
$h^{\alpha\alpha}$	1.0	1.0	1.0
$h^{\alpha\alpha'}$	1.0	1.0	1.2

Table 5.2: Constants used in FCC/BCC simulations

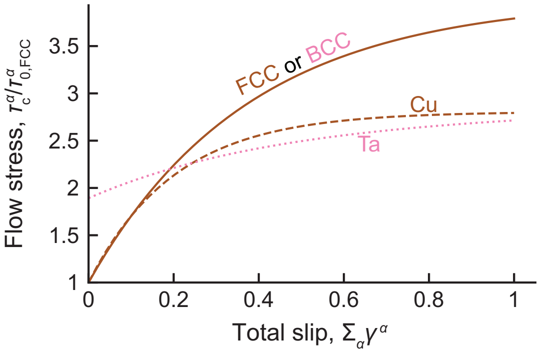

Figure 5.3: Plot of flow stress, τ^α, as a function of the total slip, $\sum_\alpha \gamma^\alpha$. The solid line shows the Voce hardening for the model FCC and BCC phases, the brown dashed line shows the Cu Voce hardening, and the dotted pink line shows the Ta Voce hardening. Note that the values have been normalized by the initial flow stress, τ_0^α, of the FCC and Cu for the FCC/BCC and Cu/Ta systems, respectively.

in which Cu exhibits typical FCC hardening and Ta exhibits a typical lack of hardening.

The total fraction of void volume in the simulation is taken to be the sum of the Jacobian of the deformation of the void voxels divided by the corresponding sum over the whole unit cell, $\sum_{\mathrm{V}} J(\mathbf{x})/\sum_{\mathrm{M+V}} \mathbf{J}(\mathbf{x})$. To determine the volume fraction of the void pertaining to each grain in the bicrystal simulations, the 3D coordinates of the nodes on the surface of the void in contact with each grain were extracted and the resulting volumes were calculated using a convex hull algorithm (specifically, Python's package scipy.spatial.ConvexHull), similar to Jeong et al. [74], which was then divided by the volume of the convex hull of the grain itself. If the sum of the two volumes of partial voids did not equal the volume of the convex hull of the entire void, the remaining volume was split in half and added to both partial volumes. In practice, this difference represented a small portion of the volume of the void.

5.3 Results

5.3.1 Properties of void-free single crystals

To highlight the sources of variation between the two material systems, several uniaxial simulations of void-free single crystals of both the model FCC, model BCC, Cu, and Ta were conducted. Figure 5.4 shows the axial stress-strain response in [001] and [111]-oriented crystals. The figure shows that the model FCC is indistinguishable from the model BCC material with $\langle 111\rangle\{110\}$ slip, which is expected given the identical properties otherwise. Figure 5.4(a) and (c) show that, compared to the BCC material with $\langle 111\rangle\{110\}$ slip alone, the BCC material with $\langle 111\rangle\{112\}$ slip was softer, and the combined case softer still. The latter part is likely due to the high number of slip systems, which promotes slip, thus reducing the stress needed to initiate slip in the material. This reduction in softness for the $\langle 111\rangle\{110\}$, $\langle 111\rangle\{112\}$, and combined slip modes is true in the Ta material in Figure 5.4(b) and (d), but there is not as much difference between the two cases where the $\langle 111\rangle\{112\}$ slip system is used alone and in combination with $\langle 111\rangle\{110\}$ slip. Because Ta has a higher yield stress but lower hardening rate than Cu, Ta is initially harder but is overtaken by the Cu single crystal at $\varepsilon_{33}\approx 2.5\%$. This crossover point is important for the results later.

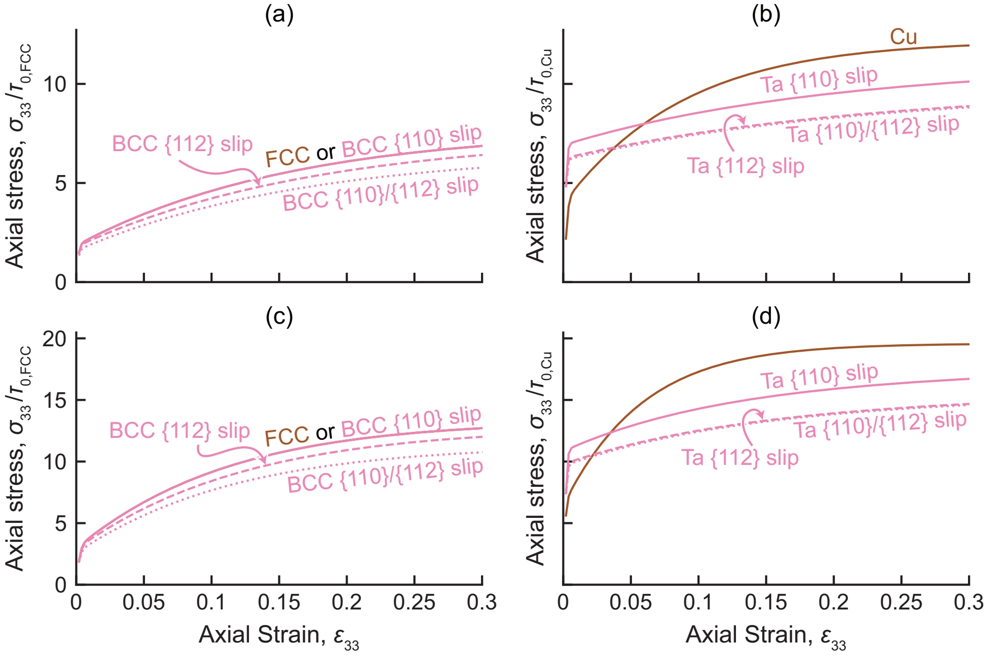

Figure 5.4: Stress-strain curves for void-free single crystals. (left, a and c) Show model FCC and acbcc single crystals and (right, b and d) show Cu ant Ta. The stress is applied uniaxially, with a fixed strain rate along the [001] (top row, a-b) and [111] (bottom row, c-d) directions, representing a soft and hard crystal orientation, respectively. As can be seen in this figure, the model FCC is indistinguishable from the BCC material allowed to only slip on the $\langle 111\rangle\{110\}$ crystal slip modes. The material is softer throughout deformation in the case of the BCC material with $\langle 111\rangle\{112\}$ slip and even more so when both slip modes are able to activate. This graded softness is true in the Ta, but there is not much difference between the case with just $\langle 111\rangle\{112\}$ slip and the case with both slip planes active. In the Cu and Ta, the differences in elastic and plastic properties results in a Ta that is initially harder, that is eventually surpassed by the Cu before 10% strain is achieved.

5.3.2 Voids at phase boundaries with special orientation relationships

We begin our study of voids at phase boundaries with a study of well-documented orientation relationships at FCC/BCC phase interfaces. These simulations comprise a bicrystal with a void in the center of the cell, with the void center coincident with the PB plane at 0°, 45°, and 90°, measuring the angle between the plane normal and the z axis and rotated in the xz plane. The use of a variety of PB inclination angles is that most materials have the two phases intertwined and the interface plane does vary, which in a previous study had implications on the loading state of the grains. The inclination angles are selected to span the range of what might be encountered. The orientations were selected to correspond to the Kurdjumov–Sach (K–S) and Nishiyama–Wassermann (N–W) orientation relationship, summarized in Table 5.1. Single crystal simulations, with each of the individual phase orientations relative to the primary loading axis in the z-direction, and with the same initial void fraction f_0=0.1, were also simulated for reference.

We begin by analyzing void growth in a bicrystal and within single crystals with the same crystallographic orientations, as an example for how data is extracted in further figures, so that we may compare void growth as a function of phase boundary inclination. Figure 5.5(a) shows the volume fraction of the void at the 0° K–S boundary of the model FCC/BCC material, where only slip on the $\langle 111\rangle\{110\}$ slip mode was allowed. Specifically Figure 5.5(a) shows the void volume fraction normalized by its initial value, f/f_0, as a function of axial strain, ε_{33}. This figure shows the results of three separate simulations: one bicrystal simulation and two single crystal simulations (one each of FCC and BCC) with the same crystal orientations relative to the primary loading axis as the bicrystal simulations. The total f/f_0 of the bicrystal simulation is plotted as a solid black line, while the partial f/f_0 for FCC and BCC in the bicrystal are plotted with a brown dotted line and pink dot-dashed line, respectively. Two additional simulations of voided single crystals with the same orientations as those comprising the bicrystal systems are plotted, where the brown solid line shows f/f_0 for the FCC [111]-oriented single crystal and the pink dashed line shows f/f_0 for the BCC [011]-oriented single crystal, as indicated in the figure. The vertical dotted line shows the axial strain (8.4%) at which the volume fractions are taken for Figure 5.5(b). This strain was chosen because it was the maximum axial strain that all of the model FCC/BCC single crystal and bicrystal simulations with the K–S and N–W orientations were able to achieve before numerical convergence was no longer possible. Figure 5.5(b) shows f/f_0 as a function of PB inclination, θ_{PB}. In this plot, the total bicrystal f/f_0 is shown with small black dots, the partial FCC and BCC bicrystal values are shown with closed brown circles and open pink triangles, and the single crystal f/f_0 with the corresponding orientations are once again a brown solid line for FCC and pink dashed line for BCC. Note that for volume fraction, the total value (black dots) in the bicrystal should be a volume average of the volume fraction pertaining to each phase of the bicrystal (colored circles and triangles), but due to the different calculation methods between the partial and total volume fraction of the void (detailed in section 5.2), this is not always the case.

Some important features to note in Figure 5.5(b) are as follows: in the 0° and 90° simulations, there is a large difference between the volume fraction of the voids in FCC and BCC single crystal simulations. "Contrast" describes the difference in the volume fraction of the voids in the two single crystals with the same orientations as in the bicrystal. The high contrast cases are the 0° and 90° cases, and the low contrast is the 45° case. Among the former, the void grew faster in the BCC grain in the bicrystal. This possibly non-intuitive result can be attributed to two factors: First, the 0° boundary induces a state of equal axial stress in the two grains, and in that case the softer grain shows

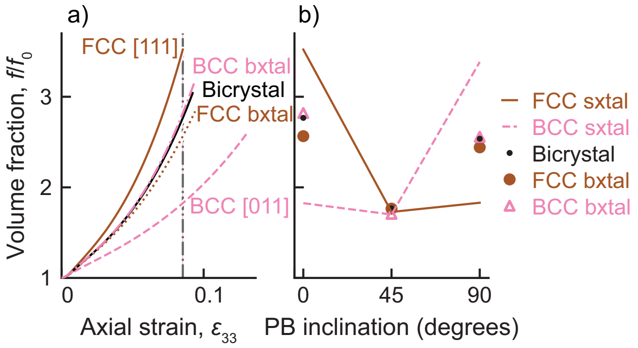

Figure 5.5: Plots of normalized void volume fraction, f/f_0, at the 0° K–S PB (shown in Figure 5.2(a)) and in single crystals with the same crystal orientations, using the model FCC/BCC properties listed in the first column of Table 5.2. (a) shows f/f_0 versus axial strain, ε_{33} for two simulations of voids in single crystals (brown solid line for FCC, dashed pink line for BCC) and one bicrystal simulation, showing the total void volume fraction (solid black line) of the bicrystal unit cell as well as the void volume fraction within each phase in the bicrystal (dotted and dot-dashed colored lines). The vertical dotted line in (a) indicates the strain at which the values in (b) show the void volume fractions for the entire bicrystal cell (small black dots), the individual phases in the bicrystal (closed large circles and open triangles), and the single crystals with the same two orientations as the bicrystal (solid and dashed colored lines), as a function of PB inclination, where the data points at 0° in (b) correspond to the values taken from (a).

faster growth; the 90° boundary induces a state of equal axial strain rate in the two halves, which typically favors growth in the harder grain, as seen in the previous chapters. Second, the BCC is oriented to be softer in the 0° case, which is evidenced by the slower growth in the single crystal compared to the FCC single crystal, and harder in the 90° case, where the void grew faster in the BCC single crystal than the FCC single crystal. The low-contrast case does not show any apparent preference due to the low contrast.

We can then look at the relationship between void growth and PB inclination angle for both of the orientation relationships and all materials, building on the previous example. Figure 5.6 presents the normalized void volume fraction of the bicrystals with K–S and N–W orientation relationships and the constituent single crystals with the same orientations, in the model FCC/BCC material (left three columns, a-c and e-g) at 8.4% strain and Cu/Ta (rightmost column, d and h) at 5.8% axial strain. These strains are the maximum strains achieved by each phase pair for all orientations before numerical convergence was no longer possible. Note that the strains that the simulations in the Cu/Ta material were able to achieve are lower, but the amount of void growth is comparable. For all K–S bicrystals, the void shows the slowest growth when the PB inclination angle is 45°, and the fastest growth when the inclination angle is 0°. The total volume fraction of the voids in the N–W bicrystals at this strain decreases with the PB inclination. The total volume fraction of the voids in all bicrystals at these strains is close to an average of the void volume fraction in the single crystals with the same orientations, or falls in between the two constituent crystals. The selection of slip mode(s) does not appear to have a strong effect on the response for the model FCC/BCC material. However, there is a larger anisotropy in growth between the volume fraction of the void of each phase in the 0° bicrystal when both the $\langle 111\rangle\{110\}$ and $\langle 111\rangle\{112\}$ slip modes could be activated for both orientation relationships. The anisotropy is more pronounced in the Cu/Ta

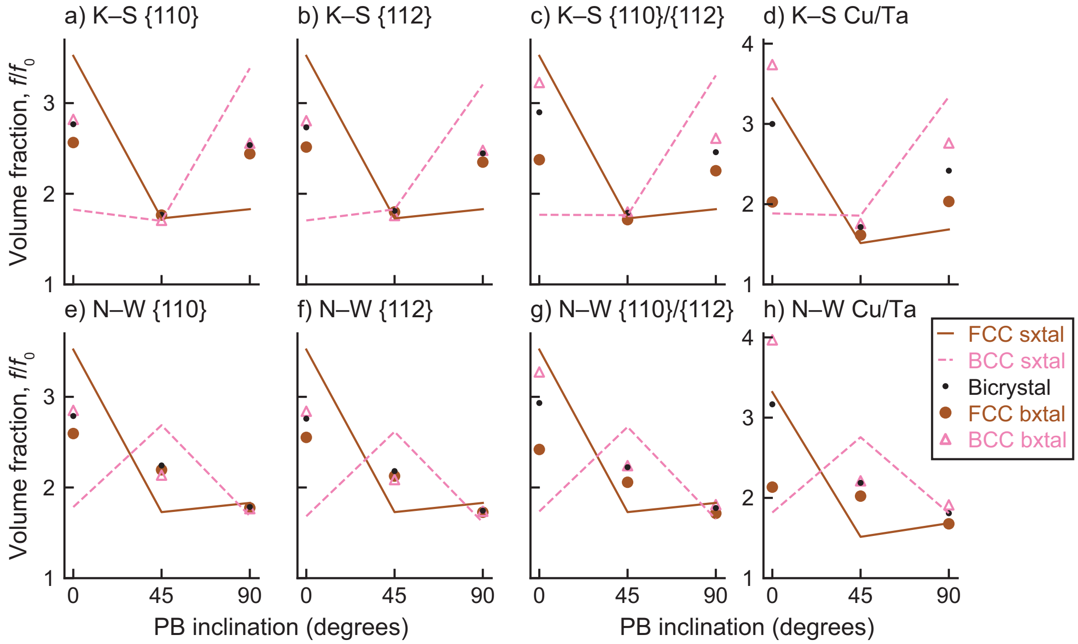

Figure 5.6: The normalized void volume fraction, f/f_0, in the bicrystals and single crystals with (a-d) the K–S orientation relationship and (e-h) N–W orientation relationship. The first three columns (a-c, e-g) show the model FCC/BCC material with a different slip system selection for the BCC phase, as noted above the figure, at 8.4% axial strain, and the last column (d, g) shows the Cu/Ta pair at 5.8% axial strain. Solid brown lines and filled brown circles correspond to single crystal and (partial) bicrystal FCC volume fractions, the dashed pink lines and open triangles are single and bicrystal values for BCC, and the black dot is the void volume fraction in the total bicrystal cell. In this configuration, the K–S bicrystals show the slowest growth when the PB inclination angle is 45°, and similar growth at the other two orientations. The total void volume fraction in the N–W bicrystal decreases with the PB inclination. The slip system selection only minorly affects void growth.

material, which allows both slip mode activation. This anisotropy in growth between the two phases in the bicrystal is expected in the 0° bicrystal, as noted in chapter 4, and is likely due to the stress state, which is shown in the next figure. However, it is notable that there is more anisotropy when more slip modes are permitted in the BCC phase. There is also more anisotropy in the K–S bicrystals with the 90° inclination angle for this slip mode selection. The voids in these more anisotropic cases prefer to grow into the BCC portion of the bicrystal, which is again likely due to whether the grains have the same axial strain rate or axial stress.

Figure 5.7 shows the normalized axial stress, $\sigma_{33}/\tau_{0,\mathrm{FCC}}$, of the bicrystal with both K–S and N–W orientation relationships in the model FCC/BCC material (left 3 columns) at 8.4% strain and Cu/Ta (far right) at 5.8% axial strain, as well as the single crystal pairs with the same crystal orientations. Note that the stresses are normalized by the initial resolved flow stress of the corresponding FCC metal (1 MPa in the case of the model FCC/BCC and 60.8 MPa, corresponding to that of Cu, for Cu/Ta) so that the two material systems can be compared. Similarly to the volume fractions of the voids, the magnitude of stress in all K–S cases increases from the 45°, 90°, to the 0° orientations, while the observed stresses in the N–W bicrystals decreases with increasing PB inclination angle. The stress seems to be more sensitive to the slip mode in this case, with the stress decreasing most notably with the use of the combined $\langle 111\rangle\{110\}$ and $\langle 111\rangle\{112\}$ slip modes in Figure 5.7(c) and (g). Finally, it is important to note how the stress in the two grains of the bicrystal differ, depending on the angle of inclination. For all 0° bicrystals, the axial stress is nearly identical in each grain, allowing the void to grow faster into the softer grain, whether geometrically or materially (the BCC grain). The 90° bicrystals are typically at the same strain (isostrain), and thus have stresses that reflect the hardness of the orientation or material, with the harder grain sustaining a greater stress, allowing faster growth in the harder grain (BCC in each case in the model material). It is interesting to note that the Ta in the 90° bicrystal is in a geometrically hard orientation, but appears to be materially softer than Cu, which is evidenced by a lower stress and higher void volume fraction in the Ta single crystal than the Cu single crystal at this strain. The axial stress in the bicrystal appears to be very similar in both grains in this “isostrain” unit cell, which is perhaps due to the lower contrast in stress apparent in the single crystals, which in turn may explain the faster growth of the void into Ta at the bicrystal. The implications of hardening and history will be discussed further in the next section.

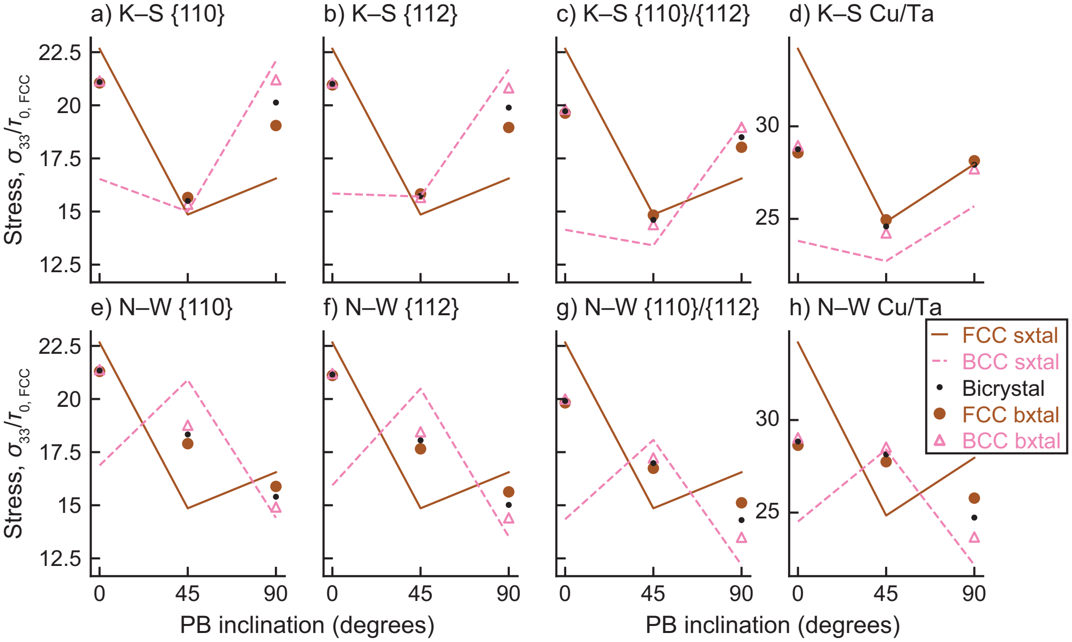

Figure 5.7: The axial stress, $\sigma_{33}/\tau_{0,\text{FCC}}$, in the bicrystals and single crystals with (a-d) the K–S orientation relationship and (e-h) N–W orientation relationship, normalized the by the initial resolved flow stress in the relevant FCC phase (the model FCC or Cu in the model FCC/BCC or Cu/Ta system, respectively). The first three columns (a-c, e-g) show the model FCC/BCC material with a different slip system selection for the BCC phase, as noted above the figure, at 8.4% axial strain, and the last column (d, g) shows the Cu/Ta pair at 5.8% axial strain. Solid brown lines and filled brown circles correspond to single crystal and (partial) bicrystal FCC stresses, the dashed pink lines and open triangles are single and bicrystal values for BCC, and the black dot is the stress in the total bicrystal cell. The slow growth seen in the 45° K–S bicrystals can here be attributed to the lower stress observed in the each grain.

5.3.3 Voids at bicrystal phase boundaries with crystal orientation fixed to the loading direction

The previous section with common orientation relationships makes it difficult to isolate the effects of the crystal orientation and PB inclination on void growth without conflating the results by changing both variables simultaneously. The following set of simulations was designed more fully probe these two variables, using the same bicrystal simulations cells with a void in the center of the cell, and PB plane angles at 0° and 90°. The simulations were assigned five crystallographic orientations ([001], [011], [111], [$\bar{1}$25], and [021]), in all possible permutations of phase pairs, with the orientations always fixed relative to the z-axis, in contrast to the previous subsection.

Figure 5.8 shows an example of data of the normalized void volume, f/f_0, for the study using the five crystal orientations. This is a hypothetical case intended to show how the variables are defined in the following figures, Figure 5.9 to Figure A.1. As in previous figures, the lines are the void properties in single crystals, and the dots and shapes are all data pertaining to the total and partial bicrystal values. The first value, termed v1, is the minimum difference between the value in the bicrystal and the two constituent single crystals, which for volume fraction is measure of whether the void in the bicrystal grows faster than in either single crystal. If the value of f_{v1} is positive (as in the example 90° case), the void volume fraction in the bicrystal is greater than in either single crystal, a phenomenon called "emergent" void growth, introduced in chapter 4. If f_{v1} is negative (as in the example 0° case), the void does not show emergent behavior, and the point lies in between the two values. The second value, v2 is a measure of the contrast of the values in the single crystals (simply the difference in the values). The value favors BCC if positive, i.e. f_{v2} is positive if the void volume fraction is greater in the BCC crystal, and negative if FCC has the greater void volume fraction at this strain.

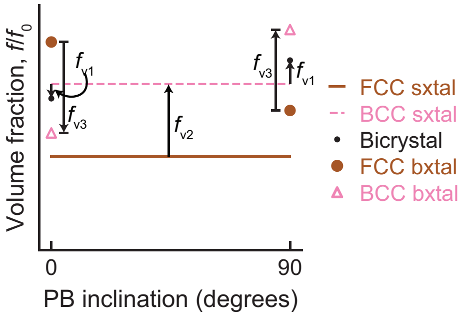

Figure 5.8: A hypothetical example of normalized void volume, f/f_0, plotted as in previous figures, used to illustrate the three key values plotted in Figure 5.9 and Figure 5.10. The first variable is the minimum signed difference between the value in the single crystal and in the total bicrystal with the same phase orientations. $f_{\text{v1}} > 0$ indicates an "emergent" case (the black point in (a) lies above either point), and $f_{\text{v1}} < 0$ indicates a rule-of-mixtures case (it lies between the two). The second variable is the difference between the value in the single crystals, with $f_{\text{v2}} > 0$ indicating that the void grows faster in the BCC single crystal. The third variable measures the difference in void fraction on each half of the bicrystal, with a $f_{\text{v3}} > 0$ indicating faster growth in the BCC half of the bicrystal.

Variable	Name	equation with variable x
v1	emergent behavior	$x_{\text{v1}} = x_{\text{bxtal}} - \max\left(x_{\text{sxtal,FCC}}, x_{\text{sxtal,BCC}}\right)$
v2	single crystal contrast	$x_{\text{v2}} = x_{\text{sxtal,BCC}} - x_{\text{sxtal,FCC}}$
v3	bicrystal anisotropy	$x_{\text{v3}} = x_{\text{bxtal,BCC}} - x_{\text{bxtal,FCC}}$

Table 5.3: Summary of the equations to determine emergent behavior, contrast, and anisotropy.

The third value, v3, measures the anisotropy of growth in the bicrystal, with a positive f_{v3} indicating faster growth in the BCC half, a value of zero indicating equal growth in each half, and a negative value indicating faster growth in the FCC half of the bicrystal. The exact determination of these values is summarized in Table 5.3.

Figure 5.9 shows the three void volume fraction f/f_0 values, demonstrated in Figure 5.8, for all model FCC/BCC simulations using the five orientations at an axial strain of ε_{33}=8.26%. The dashed arrows in Figure 5.9(a-c) indicate the history of the 90° [111]-[111] pair where the $\langle 111\rangle\{110\}$ and $\langle 111\rangle\{112\}$ slip modes are both permitted, which is the case plotted in Figure 5.11. Figure 5.9(a) indicates that the emergent behavior (where the void grows faster at the bicrystal, f_{v1}) only occurs in cases where contrast is low ($|f_{\mathrm{v2}}|$ is small). Figure 5.10(b) does not show any apparent connection between anisotropy, f_{v3}, and emergent behavior, but (c) does indicate a connection between grain boundary inclination angle, contrast, and anisotropy: There is a negative correlation between f_{v2} and f_{v3} for the simulations with a 0° grain boundary (red circles). What this means, is that the void at the bicrystal prefers to grow into the slower-growing single crystal phase. If the FCC single crystal grows faster than the BCC single crystal ($f_{\mathrm{v3}}<0$), the void in the bicrystal grows into the BCC phase with this inclination angle. The opposite is true for the 90° simulations (green circles), but the trend is not as strong. This trend mirrors what was seen in previous grain boundary simulations in chapter 4, and the K–S and N–W simulations. The arrows in each of the three indicate a monotonic trend up to this strain.

Finally, Figure 5.9(d) shows the distribution of the anisotropy, f_{v3}, split by the three slip mode options in BCC. The use of combined slip modes shifts the anisotropy to favor growth in the BCC phase for both the 0° and 90° PB inclinations. In the 0° case, this observation can be rationalized based on the results in Figure 5.9(c), which demonstrates that the isostress case favors void growth into the softer grain. The BCC grain with the combined slip modes would be softer due to the greater number of available slip systems that are capable of accommodating more strain. However, in the 90° case, the reason for the increase is not immediately evident, as this state tends to favor void growth into the harder grain. To understand the role of slip mode availability, we mapped the slip activity in the BCC grain as the void grows. In regions where there was significant plasticity when one slip mode was allowed, such as near the void, the number of active slip systems is greater when both slip modes are allowed. In regions that did not show active slip, far from the expanding void, the number of active slip systems is minimally affected by the number of available slip modes. The enhanced slip activity near the void

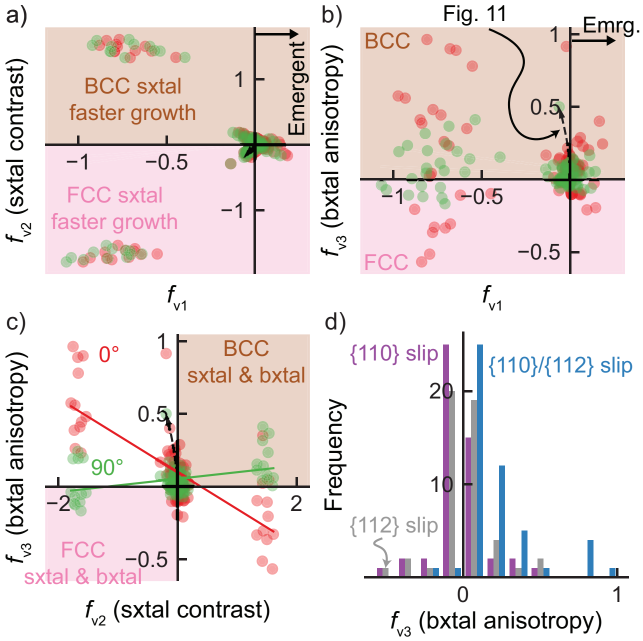

Figure 5.9: Plots of three key void volume fraction f/f_0 variables (indicated in Figure 5.8 and Table 5.3) for the model FCC/BCC simulations at ε_{33}=8.3% for the isostress (0°, red) and isostrain (90°, green) PB inclination, showing the relationship between (a) f_{v1} and f_{v2}, (b) f_{v1} and f_{v3}, and (c)) f_{v2} and f_{v3}. The (a-c) dashed arrows indicate the path of the 90° [111]-[111] pair where the ⟨111⟩{110} and ⟨111⟩{112} slip modes are permitted, which is the case plotted in Figure 5.11. (d) shows the distribution of the anisotropy, f_{v3} for the simulations split by the three slip mode selections (purple, gray, and blue for ⟨111⟩{110}, ⟨111⟩{112}, and combined slip, as indicated by the plane on the figure).

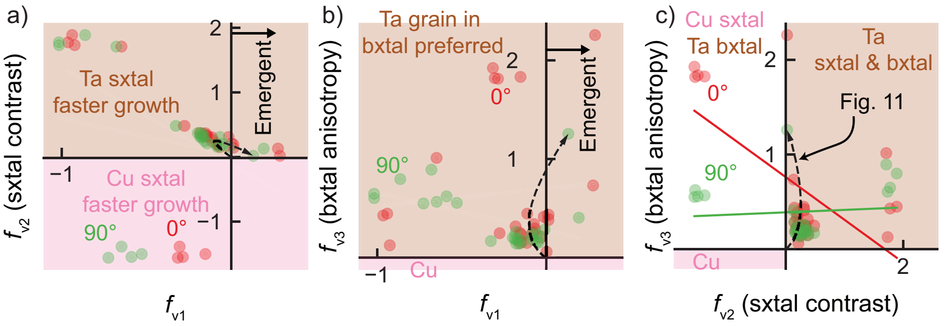

Figure 5.10: Plots of three key void volume fraction f/f_0 variables (indicated in Figure 5.8 and Table 5.3) for the Cu/Ta simulations at ε_{33}=5.8% for the isostress (0°, red) and isostrain (90°, green), showing the relationship between (a) f_{v1} and f_{v2}, (b) f_{v1} and f_{v3}, and (c)) f_{v2} and f_{v3}. The dashed arrows in these plots indicate the path of the 90° [111]-[111] pair, which is the case plotted in Figure 5.11.

encouraged the more rapid deformation in the BCC grain, but the bulk of the material was unaffected, allowing f_{v3} in the isostrain case to be uniformly increased.

To elucidate the role of hardening differences present in Cu/Ta, on void growth in bicrystals, Figure 5.10 shows the same three void volume fraction f/f_0 variables for the Cu/Ta material at ε_{33}=5.8%. The trends are largely the same as in the FCC/BCC case without hardening differences. In Figure 5.10(a) emergent behavior only occurs in low-contrast cases. Also, the void prefers to grow into the slower-growing phase (as a single-crystal) phase in the isostress (0°) state, and weakly prefers to grow into the faster-growing phase in the isostrain (90°) case. However, the main difference is that void growth is always preferred in the Ta grain unlike that seen in the model FCC/BCC case, although this is likely due to the higher number of slip systems in Ta, and the very fast hardening in Cu. Finally, looking at the arrow, which follows the trajectory of the 90° [111]-[111] pair, we see that the progress of the variables in time is not monotonic because it does not stay in the same quadrant, specifically crossing in f_{v1} and f_{v2}. This is discussed in the following figure. The anisotropy f_{v3} appears to increase monotonically in this case.

It is worthwhile to show how the stress and void volume fraction evolves over the course of deformation, as the model FCC/BCC material and Cu/Ta show different trends, as indicated by the dashed arrows in Figures 5.9 and 5.10. Figure 5.11 shows the volume fraction and axial stress of the 90° (isostrain) [111]-[111] set, which are indicated in the dashed arrows in Figures 5.9 and 5.10. In the case of the model FCC/BCC material, the corresponding simulations where the $\langle 111\rangle\{110\}$ and $\langle 111\rangle\{112\}$ slip modes are both permitted are shown in this figure. Figure 5.11(b) shows that void in the Cu/Ta pair begins by following growing at a rate that is between the two single crystals (rule-of-mixtures growth), but eventually accelerates faster than the void in the Ta single crystal (emergent growth), due to the very fast hardening of the Cu phase. The Ta half of the bicrystal is always faster than growth in the Cu half, even as the stress increases in the Cu half (d), thus anisotropy continues to grow. The voids may grow initially in Cu rather than Ta since Cu initially has the lower yields stress. With straining, Cu will harden quickly, whereas Ta will not. This rapid hardening would lead to the formation of a ring of highly slip-resistant material around the void. In contrast, Figure 5.11(a) shows a rule-of-mixtures growth the entire history. The BCC half grows faster, given the higher stress in that half, shown in Figure 5.11(d).

With several references to the nature of the loading condition, or whether the grains are truly in isostrain and isostrain conditions, it is useful to demonstrate those values to support these claims, beginning with stress differences between the two grains in the bicrystal. Figure 5.12 shows stress and strain-rate, plotted as the difference between the BCC and FCC phase in the bicrystal, with positive values favoring BCC ($x_{\text{v3}} = x_{\text{bxtal, BCC}} - x_{\text{bxtal,FCC}}$), against the corresponding value in void volume fraction, f_{v3}. Here, the points are shown at 8.0% and 5.0% in the model FCC/BCC (solid circles) and Cu/Ta simulations (open triangles), respectively. The values are again normalized by the corresponding FCC τ_0. In Figure 5.12(c), the 0° simulations have very small differences in

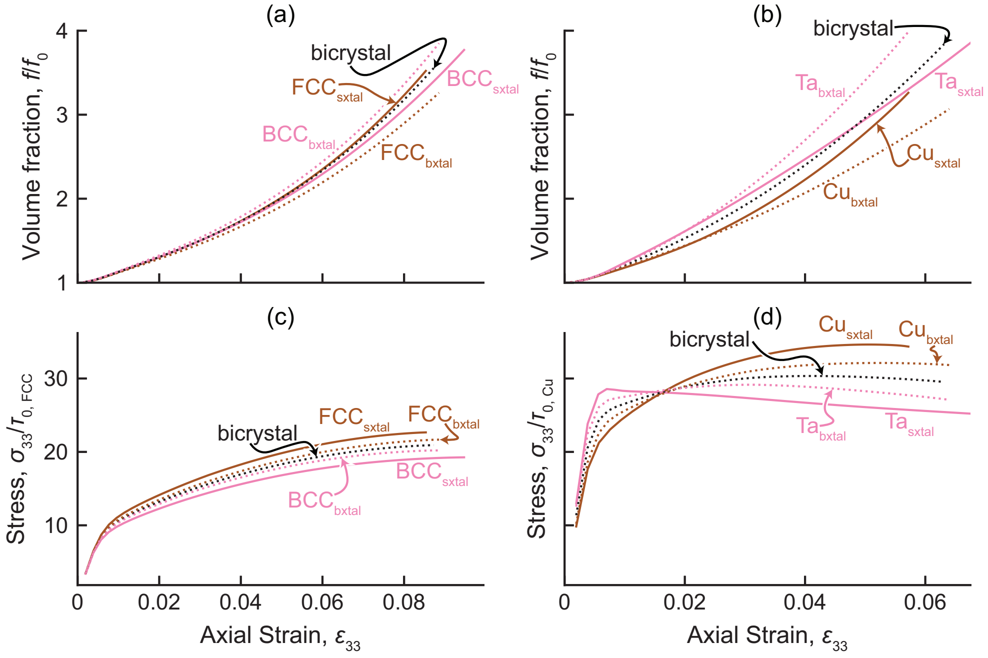

Figure 5.11: (a-b) Volume fraction and (c-d) axial stress as a function of axial strain of the 90° [111]-[111] bicrystal pair and single crystals for both the (a, c) model FCC/BCC where the $\langle 111\rangle\{110\}$ and $\langle 111\rangle\{112\}$ slip modes are both permitted and (b,d) Cu/Ta, which are indicated in arrows in Figures 5.9 and 5.10. Solid lines indicate the single crystal simulations, and the dotted lines represent that of the bicrystal, where brown and pink indicate the values that correspond to the FCC and BCC phases, respectively. The black line is the total values in the bicrystal simulations.

stress between the two phases in the bicrystal ($\langle\sigma_{33}\rangle_{\mathrm{v3}}$ is small), consistent with the label of "isostress" applied earlier. However, that is only true for the stress in the principal axis, σ_{33}, while the phases in the 90° "isostrain" simulations appear to have the same x-component (σ_{11}, shown in (a)), which is consistent with the non-zero stress applied in that direction to maintain a triaxiality of σ_{tx}=3.0. It is worth noting, however, that in all cases with a non-zero stress anisotropy in Figure 5.12(a-c), the degree of stress anisotropy, $\langle\sigma\rangle_{\mathrm{v3}}$, does scale positively with f_{v3}, most notably in the transverse directions (a,b). We thus find that in the model FCC/BCC system, the void grows faster in the grain with the higher stress. Interestingly, this is not the case in the Cu/Ta system.

To explore the idea behind strain rate and void growth, the lower half (d-f) of Figure 5.12 shows the strain-rate difference in the bicrystal. The range of spread for the normal strain rate in the axial direction ($\langle\varepsilon_{33}\rangle_{\mathrm{v3}}$, shown in Figure 5.12(f)) is smaller in the isostrain case (90°), but it is not as close to zero as in the stress plots above. Because the volume averages are taken over the solid material and do not include the void, the deviation from zero is due to the contribution of void growth to the strain rate. If the strain rate of the void in each bicrystal half were taken into account, one might expect that the isostrain condition in the axial direction would be fulfilled. The relationship between $\langle\varepsilon\rangle_{\mathrm{v3}}$ and f_{v3} seen in Figure 5.12(f) appear to be reversed to those seen in Figure 5.12(d), for several reasons. Beginning with Figure 5.12(f), the voids in the 0° bicrystals (red) show a positive relationship between $\langle\varepsilon_{33}\rangle_{\mathrm{v3}}$ and f_{v3}. This is because the grains are at the same stress, so the void grows fastest in the grain that is accommodating the most strain. A negative relationship between $\langle\varepsilon_{33}\rangle_{\mathrm{v3}}$ and f_{v3} is seen in the 90° bicrystals (green). In this case, the halves must be at the same strain-rate, so when the void is grows faster in one half than the other, the surrounding material must deform slower to accommodate. In x-direction, shown in Figure 5.12(d), the relationship is the opposite for both PB inclinations as compared to their counterparts in the primary axis.

The 90° bicrystals (green) in (d) show a positive relationship between $\langle \varepsilon_{11} \rangle_{\mathrm{v3}}$ and f_{v3}, likely for the same reason that the 0° bicrystals (red) in (f) show a positive relationship: when the component of stress is fixed in each grain, the void grows fastest in the material that is able to accommodate greater strains. The 0° bicrystals in (d) shows a negative relationship between $\langle \varepsilon_{11} \rangle_{\mathrm{v3}}$ and f_{v3}, this time likely due to the growth of the void in one direction, causing material contraction in the other two directions. Given that the stress in the primary axis is positive, and stress is not constrained (beyond that the average stress must maintain the applied stress triaxiality), so the faster the grain grows in the axial direction, the slower it grows in the transverse direction. The same effect seen in the 0° bicrystals in (d) is likely the reason for the negative relationship between $\langle \dot{\varepsilon}_{22} \rangle_{\mathrm{v3}}$ and f_{v3} seen in all bicrystals in Figure 5.12(e).

We explored various correlations between anisotropic and emergent behavior and found that the von Mises plastic strain shows a strong connection to both behaviors. The void grows as the material deforms plastically, so it is logical that there is a very strong positive correlation between average von Misses strain and void volume fraction. Figures supporting this correlation can be seen in Appendix A. Since the growth happens by deformation of material surrounding the void, it seems that again there is a strong positive correlation between the standard deviation of $\varepsilon^{\mathrm{p}}_{\mathrm{vM}}$ and void volume fraction, as is the case for average $\varepsilon^{\mathrm{p}}_{\mathrm{vM}}$. A positive v1 for standard deviation indicates that the spread of the data in the bicrystal is higher than in both respective single crystals. It is likely that an increase in the standard deviation translates to a stronger plastic strain gradient. The v3 value for standard deviation indicates a higher variation in one half of the bicrystal (and again, possibly a higher strain gradient). Evidently the plastic strain in the Ta grains is more heterogeneous than in the Cu grains. Because of the greater number of available slip systems, even in cases where Ta has a higher initial yield strength, the average and standard deviation of plastic strain exceeds that of Cu.

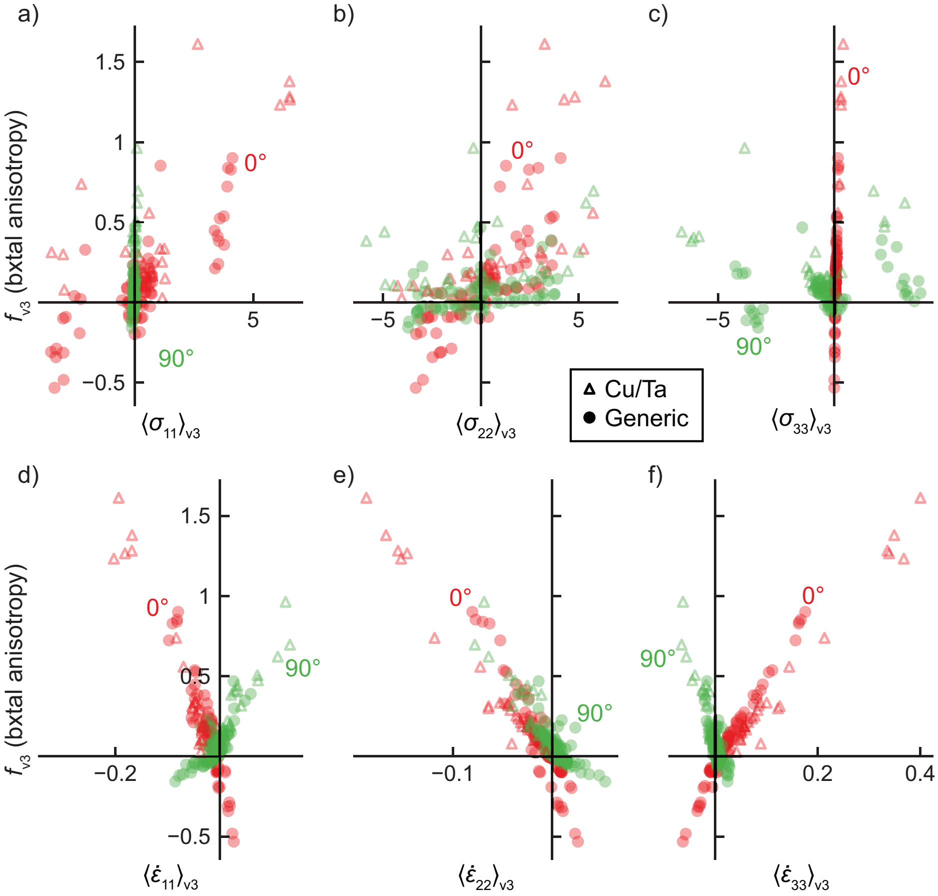

Figure 5.12: Void growth anisotropy in the bicrystal, f_{v3}, plotted against the corresponding difference between grains in the bicrystal for (a-c) normal stress and (d-f) normal strain rate. Red and green correspond to bicrystals with 0° and 90° PB inclination angles. Cu/Ta (open triangles) are shown at 5.03% axial strain, with stress values normalized by 60.8 MPa, the tau_0 of Cu. The model FCC/BCC material (solid circles) are shown at 8.04% axial strain, with stress values normalized by 1.0 MPa, the τ_0 of both materials.

The plastic strain fields for a PB pair showing emergent behavior were studied, and there is an indication that the strains are enhanced relative to the single crystal counterparts, particularly close to the void, creating strong strain gradients. Appendix A shows f_{v1} and f_{v3} as a function of the corresponding average and standard deviation of von Mises plastic strain, $\varepsilon^{\mathrm{p}}_{\mathrm{vM}}$, and the local fields for select single crystals and bicrystals.

To understand the anisotropy and how anisotropy relates to the local plastic strain, three pairs were selected from the model FCC/BCC that showed distinct behaviors. Figure 5.13 shows the von Mises plastic strain field, $\varepsilon_{\mathrm{vM}}(\mathbf{x})$, at 8% total axial strain in the model FCC/BCC, shown in the xz-plane for: (a) fastest growth in the BCC phase (greatest f_{v3}) [111]−[001], (b) least anisotropy (least $|f_{\mathrm{v3}}|$) [$\bar{1}$25]−[111], and (c) fastest growth in the FCC phase (most negative f_{v3}) [111]−[001] grain pairs. The same bicrystals pairs are shown for the Cu/Ta at 5% axial strain in Figure 5.13(d-f). The differences between the single crystal and the corresponding phase in the bicrystal, which are shown in Figure A.2, are not shown here. In the model FCC/BCC material, the anisotropy clearly is connected with the plastic strain near the void, with the phase that is preferred showing enhanced values of plastic strain (and gradient). In the Cu/Ta, all simulations show higher (if only by a small amount) values of plastic strain near the void in Ta. Simply put, the more void growth one grain experiences, the greater the plastic strain in that grain. However, because of fast hardening in Cu, the strain distribution is more diffuse than in Ta: As the void starts to grow and deform the surrounding material, this material hardens quickly. As a consequence, it may then become easier for the void to grow via the deformation of material further away from the void that has yet to harden, leading to a more diffuse strain field.

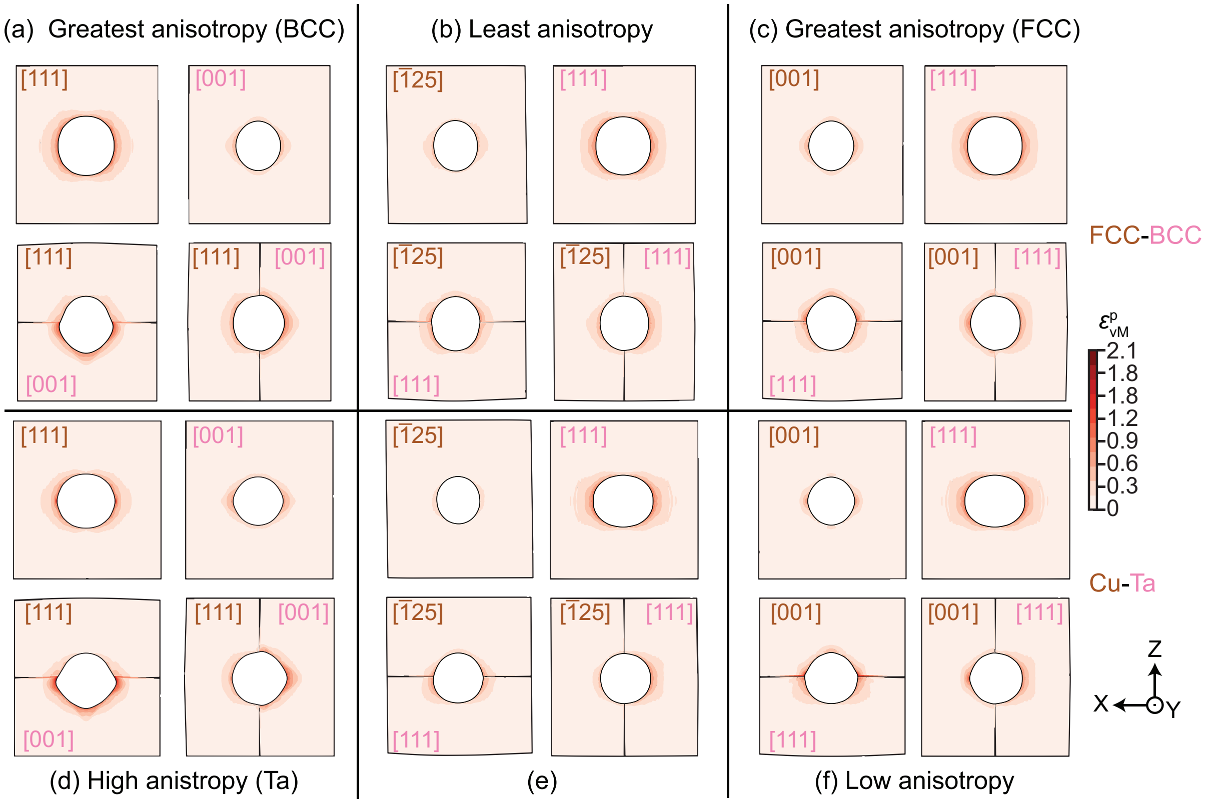

Figure 5.13: Contour plots of von Mises plastic strain field, $\varepsilon_{\mathrm{vM}}(\mathbf{x})$, for the in the (a-c) model FCC/BCC and (d-f) Cu/Ta, showing selected various single crystals (top row), and bicrystals with the same crystal orientations (bottom row). The three orientation pairs are (a,d) [111]−[001] (left two columns), (b,e) [$\bar{1}$25]−[111] (middle two columns), and (c,f) [001]−[111] (right two columns), which represent the decreasing f_{v3} values from left to right. In contrast to the previous figure, the difference between single crystalline and bicrystalline simulations are not shown.

5.3.4 What promotes void growth in strain-rate controlled biphase bicrystals?

The previous sections focuses on factors related void growth, but doesn't address the question of what contributes to the fastest overall growth of voids in the bicrystal. Figure 5.14 shows all of the bicrystal simulations, from the previous two sections, for (a) the model material at 8.3% axial strain and (b) Cu/Ta at 5.8% axial strain, which is the maximum strain that all simulations were able to achieve before numerical convergence became impossible. On the dependent axes, the rule-of-mixtures average of the normalized void volume fraction at the respective strain in single crystal simulations with the corresponding orientations for each phase. The void volume fraction of the bicrystal is plotted on the independent axis. The dashed line has a slope of 1, above which the bicrystal void volume fraction exceeds the rule of mixtures' prediction (but does not necessarily display emergent behavior), and below which the void in the bicrystal is growing slower than this prediction. The simulations from subsection 5.3.2 are shown as open square symbols, and the results from subsection 5.3.3 are shown as filled circles. The colors red, blue, and green indicate PB inclination angles of 0°, 45°, and 90°, respectively. The fastest growing voids of all bicrystals is the [111]-[111] bicrystals (which is shown earlier in Figure 5.11 for the 90°bicrystal with $\langle 111\rangle\{110\}$ and $\langle 111\rangle\{112\}$ slip available), which are the geometrically hardest orientations in both phases. The next fastest growing void is within the N–W 0° bicrystal, which is identical to the 0° [111]-[011] bicrystal simulations for both materials. However, because it combines the hardest orientation ([111]) with a much softer orientation ([011]), it does not grow as quickly as the [111]-[111] bicrystal. For the model FCC/BCC, the inclination angle does not have a very strong effect when the orientations remain the same, as is the case with the closed symbols. The K–S and N–W simulations, given that the inclination angle is fixed to the

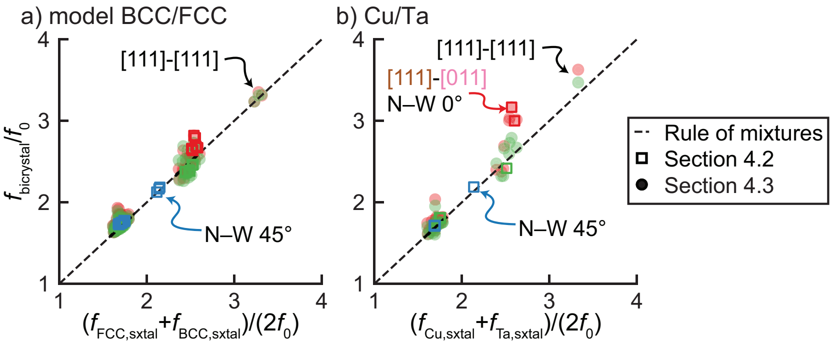

Figure 5.14: Plot of void volume fraction in the bicrystals in Subsections 5.3.2 and 5.3.3 as a function of the average of the void in the single crystals with the same orientations as in each bicrystal. These values are plotted at (a) ε_{33}=8.3% in the model FCC/BCC and (b) ε_{33}=5.8% in Cu/Ta. The dashed lines have a slope of 1 and pass through the origin.

normal of the phase boundary, change with their respective single crystals. Overall, the rule-of-mixtures average in the model material is an excellent predictor.

In the Cu/Ta (Figure 5.14(b)), the rule of mixtures' predictions are frequently exceeded. This likely has to do with the different histories of the single crystal and bicrystals, given different hardening behavior. In this case, the PB inclination did have a slight impact, particularly when harder crystals were involved. The 0° bicrystals appear to have faster growth relative to the 90° bicrystals. The fastest growing void is in the 0° [111]-[111] bicrystal, which is emergent. This is notable, because this is the fastest growing void in the single crystals, indicating that voids in this bicrystal exceeds that of any single crystal.

5.4 Discussion

The behaviors of bicrystals that we focused on in this study were the presence of emergent behavior, which is an enhancement of void growth at the bicrystal relative to its single crystal constituents, and anisotropy, when growth is preferred in one phase over the other in the bicrystal. A third behavior studied is contrast, which is the relative difference in growth in the constituent single crystal, which is roughly a measure of how soft or hard a crystal orientation is, had a strong influence on both of these behaviors. When the contrast is high, this implies that the void is at a pair where one phase is soft and the other is hard. When the values are close, the two grains/phases have similar strengths in this orientation. In this study, it was confirmed that emergent behavior occurs only when the contrast is low. Anisotropic behavior was generally enhanced by this contrast, although anisotropy was also highly dependent on the inclination of the phase boundary, which affected the loading state of each grain.

These behaviors are similar to the previous study of voids at grain boundaries in FCC in the previous chapter. When there is little difference between the two phases other than the use of the slip mode (as in the model FCC/acbcc material), there were no noticeable differences present. The selection of the slip mode had a small effect on the material, lowering the stress needed to initiate plasticity and thus making the material, in general, softer. As in the previous chapter, which uses LS-EVP-FFT on voids at grain junctions, the overall growth of the material is impacted by the crystal orientation relative to the axis of primary loading, although the triaxiality of stress affects this slightly. In the model material, there is no preference for growth in BCC or FCC, but there is a tendency for the loading condition to dictate the level of anisotropy. This mirrors the grain boundary simulations (chapter 4) and the intragranular simulations (chapter 2), the latter of which showed that the loading state, whether strain rate or stress controlled, dictated the ordering of the void growth rate in single crystals. For real-world applications, the local loading state of a fully dense material, in general, would likely be able to show the likelihood of anisotropy. Finally, the presence of emergent growth is, as in the previous study, observable in low-contrast bicrystals in both the model FCC/BCC and Cu/Ta bicrystals. The plastic activity is enhanced on both halves of the bicrystal relative to the single crystal, which causes enhanced void growth.

However, there were some deviations from the grain boundary simulations, particularly in the case of Cu/Ta. While anisotropy was present, and had the same *overall* trend (the anisotropy was higher in the case of the 0° bicrystals, likely due to the loading state of each grain), the material preferred growth in Ta, even in the few cases where Cu was the geometrically, and eventually, materially harder phase. This behavior was reflected in the plasticity experienced near the void: Ta, in general, experiences greater plasticity. Emergent behavior was not present in the same cases in Cu/Ta (notably, the [111]-[111] pair, which would not have resulted in any emergent behavior in single phase materials, because it would behave as a single crystal, even if it were a twin boundary), due to the different behavior between the two phases. This different behavior, notably the difference in hardening, did give rise to non-monotonic behavior in the sense of emergent behavior. This different hardening behavior meant that while the tantalum may initially be at a higher stress (in the 90° bicrystal), eventually the Cu grain would overtake it. Still, the void would always be larger in the Ta crystal. The important implication here is that modeling this and developing a model for implicit behavior would not be as simple because the history of the material would additionally have to be captured. It would not be possible to run single-step simulations to formulate an instantaneous yielding criterion without testing to see if the behavior is consistent with the entire hardening history of the material.

The crystal orientations relative to the loading direction strongly indicated how quickly the void would grow. With strain-rate control, the voids grow most quickly in grains that have geometrically hard orientations relative to the primary axis. The fastest growing void in a stress-controlled simulation (or experiment) would likely be in the softest crystal, likely the [001]-oriented grain, although this could change depending on triaxiality, as indicated in chapter 2. Because K–S and N–W orientation relationships join a geometrically hard orientation ([111]) with a softer orientation ([101] or [100]), there is no configuration that would align both grains in a geometrically hard orientation. A twin grain boundary, or a similar phase boundary, where the grains are aligned such that they are both being loaded along the [111] direction would contain the fastest growing void.

Although the rule of mixtures calculation was an excellent predictor for the growth of voids in the model material, the Cu/Ta simulations indicate that hardening rate differences in the two constituent materials in a void in biphase materials can cause a significant deviation from this calculation. This has implications for damage models that seek to implicitly model void growth and ductile damage. If hardening is similar in both materials, or if the void is at a single-phase grain boundary, there is no need to develop a separate damage model outside of one that takes crystal orientation into account to capture the overall void growth at grain and phase boundaries. However, if the hardening behavior is significantly different, a closer look may be necessary, although this necessitates further research.

Finally, the enhanced strain gradients that are caused by the enhanced plastic strain near the surface of the void that correlate with the emergent behavior and anisotropy have interesting implications with respect to size effects, specifically those that relate geometrically necessary dislocations by means of strain-gradient plasticity models. Given that some models reduce the gradient, would emergent behavior and anisotropy, too, be suppressed?

5.5 Conclusions

In this work, using a large-strain elastic-viscoplastic fast-Fourier transform (LS-EVP-FFT)-based model, we investigated the effects of crystallographic orientation, phase boundary inclination, and slip mode selection on void growth at interphase boundaries. To focus on void growth, instead of nucleation or coalescence, two sets of simulations were conducted with an initial void volume fraction of 1%. All simulations were carried out with a set of model face-centered cubic (FCC)/body-centered cubic (BCC) materials with slip modes of $\langle 111\rangle\{110\}$, $\langle 111\rangle\{112\}$, or both for the BCC materials, as well as Cu/Ta with both slip modes active. The first set of simulations investigated the crystallographic effects of void growth using two commonly observed orientation relationships to see the general trends of the variation in material properties, and the second set used a selection of five orientations fixed to the loading direction, while varying the phase boundary inclination angle to avoid conflating the results of the two variables.

Some general conclusions may be drawn from this study. First, in two-phase bicrystals, voids generally grow faster in softer grains, which exhibit higher plastic strain rates at a given stress, in stress-controlled/isostress conditions, preferring harder grains only in some strain-controlled/isostrain conditions. Phase boundary (PB) inclination angle, which strongly affects the local loading condition of the grains, and thus the growth of voids in each individual grain, weakly affects the total void growth. Slip mode selection does not have a strong affect on the overall behavior of the material, but when more slip systems are available, the BCC phase was softer and had slightly faster void growth in the bicrystal. Finally, there is a subset of orientations in which the growth of voids is similar in single crystals, where the growth of voids is faster in the bicrystal than in either single crystal ("emergent growth").

However, these trends begin to break down in real materials due to the low yield stress but high strain hardening in typical FCC metals (Cu in this work) and the high yield and low to no strain hardening in BCC (Ta in this work). Void growth in Ta is faster in the bicrystal, regardless of orientation, due to the higher number of slip systems. In contrast to the model material, where emergent behavior is nearly instantly apparent, the history of the material hardening additionally matters. In a few cases in Cu/Ta, while the void did not initially show emergent behavior, it eventually showed emergent behavior. Comparison with the model FCC/BCC case indicates that this is again due to the different strain hardening behavior.

Ultimately, though, the loading conditions dictate in which bicrystals the voids grew fastest in. In strain-rate controlled simulations, voids at the intersection of two phases that are geometrically hard show the fastest growth.

As far as the authors are aware, emergent growth has not been confirmed outside of CP-FFT, and thus using crystal plasticity finite element (CP-FE) to confirm the presence of emergent growth would be valuable. Because void growth in crystalline media is highly dependent on loading condition, additional studies using different triaxialities, Lode parameters, and stress-controlled simulations would add value to the current knowledge base. Now that studies have been done on FCC/BCC, studies on FCC/HCP and BCC/HCP materials are important to conduct. Finally, the use of strain-gradient plasticity on the systems noted in this paper would elucidate the connection between plastic strain and anisotropic and emergent behavior.

Chapter 6

Summary and Conclusions

This dissertation focuses on the effect of triaxiality, crystallographic nature, and phase on the growth of voids in crystalline metals. Void growth is a plastically mediated process, whether by the emission or absorption of dislocations. Here we treat plasticity at the mesoscale and use a quasi-static crystal plasticity model to identify the key micromechanical variables for void growth. This dissertation focuses on the progressive introduction of more heterogeneous neighborhoods around voids: within the crystals, at grain boundaries, and finally, at phase boundaries.

In chapter 2, a dilitational viscoplastic fast-Fourier transform (DVP-FFT) algorithm was used to study the effect of lattice orientation and triaxiality on the growth of voids in single crystals and grain interiors. It was found that in single crystals, in strain-rate controlled simulations with a fixed stress triaxiality, the voids in the hardest grains, that is, the grains oriented such that at the same stress they exhibit less plasticity, exhibited fastest growth, while the softer grains showed slower growth. The opposite was true in fully stress-controlled simulations, a finding that has not been explored to date in the literature. When there were many interacting voids in a polycrystalline material, the correlation between void growth rate and orientation was very weak. However, on average, the trends in void growth observed in single crystals were similar in the polycrystalline material, and the orientation effects on void growth strengthen with triaxiality, possibly due to more isotropic *overall* behavior of the polycrystal at higher triaxialities.

In chapter 3, a large-strain elastic-viscoplastic fast-Fourier transform (LS-EVP-FFT) model was introduced, which was used in the remainder of the research in this dissertation. The LS-EVP-FFT allows for geometrically accurate representations of spheres, reducing the noise in the mechanical fields created by the edges and corners of the voxels in the DVP-FFT, and also incorporates elasticity. Several modifications were made to improve numerical stability by reducing excessive deformation of the void voxels, which are infinitely compliant, at the material-void interface. Several cases are presented as validation, and several single-crystal simulations in the previous chapter are compared to single-crystal simulations using the LS-EVP-FFT, to indicate that the trends seen in the previous chapter are maintained.

In chapter 4, we applied the LS-EVP-FFT algorithm to study the growth of voids at grain junctions. Total void growth was largely dependent on the crystal orientation of the grains, rather than the grain boundary misorientation or inclination angle. We found that, given a fixed stress triaxiality and constant strain rate, voids at grain boundaries grow faster into softer grains when the axial stress was equal in both grains but that voids occasionally grow faster into the harder grains in the case where the axial strain rate was most similar. There were also a small number of cases where the voids grew faster when placed at the grain boundary or triple junction than in any constituent single crystal. This “emergent” behavior occurred when the slip activity was enhanced in all grains relative to their single-crystal counterparts. The study indicates that faster void growth continues once it has begun but still indicates the possibility that voids may be forming primarily embedded in one grain in studies that indicate a preference for grain growth.

Finally, we used the knowledge and work gained in the previous chapters to understand void growth at phase boundaries in chapter 5. A model FCC/BCC material, which differed only in slip mode selection, showed very similar behavior to the grain boundary results, confirming the presence of emergent behavior at low-contrast grain boundaries. A Cu/Ta material shows similar trends, but does indicate that voids grow slightly faster into Ta in bicrystal simulations, in part due to the higher number of slip systems in Ta. Because of the higher hardening of Cu, Cu eventually overtook Ta in flow stress, which led to non-monotonic behavior, and led to a greater deviation from a void growth rate that followed a rule of mixtures' of the void growth in single crystals with the same orientations. The difference in hardening rate did not appear to have a strong impact on the grain in which the void preferred to grow. Strain gradients appeared to increase in emergent cases.

Overall, the results follow a common trend: the loading condition and the crystal orientation(s) of the material will dictate how quickly the voids grow. For strain-rate controlled crystals, voids placed in the single crystal or at an interface grow fastest in and within the crystals with a "hard" orientation, which is not immediately intuitive. For stress-controlled simulations, voids grow fastest in and within the crystals with a “soft” orientation. This distinction is important and is related not only to the macroscopic boundary conditions, but also to the grain-averaged loading condition. For voids that are at grain or phase boundaries, the inclination of the grain or phase boundary can change this loading condition. In general, the inclination angle has only a small effect on the growth of the void, provided that the orientation of crystals relative to the primary loading axis remains fixed. The crystal orientation(s) of the unit cell and the macroscopic loading have a stronger effect on overall void growth. Simulations and experiments that modify both variables simultaneously cannot say with certainty that one variable or another is the root cause of any observed change in void growth. It is also of utmost importance to clearly outline the loading state of the material because it has a clear impact on the conclusions: it dictates whether void growth is faster in geometrically soft or hard orientations.

The appearance of emergent behavior, in which voids grow faster at the interface of two or more crystals than in any of the constituent single crystals with the same boundary conditions applied macroscopically, to the knowledge of the authors, has not been explored or observed outside of these simulations. These bicrystals typically have greater overall slip activity than their corresponding single crystals and occur only at interfaces between crystals with similar — but not equal — growth as single crystals. Where hardening behavior is similar, this behavior is immediately in effect, but some cases of emergent behavior only become apparent when one material hardens more than the other, which is a behavior that is characteristic of FCC/BCC biphase materials.

Chapter 7

Recommendations

The use of crystal-plasticity-based fast-Fourier transform algorithms to explore void growth in metals has enabled us to better understand the importance of crystal orientation and loading condition. Further research is necessary to explore and quantify ductile growth in failure in quasi-static and dynamic loading conditions. The author has recommendations for future research prospects that can be categorized as experimental, explicit, and implicit/analytical modeling.

First, experiments are critical to verify and validate this model. While it may be difficult to replicate the loading conditions within large single crystals or bicrystals with voids, experiments could be conducted to understand whether emergent void growth is indeed a true phenomenon. The use of additively manufactured metals, tracking the formation of voids during the 3D printing process [135], with purposely seeded voids could be one way to achieve a coarse-grain structure. Specific orientations would be achieved by machining or printing the parts such that it can be gripped with the loading direction in mind. More simulations might have to be conducted to find a suitable grain or phase boundary pair that would be predicted to be emergent and possible to manufacture, and then single crystals with voids would need to be tested as well. The crystals or bicrystals would need to be large enough to grip, test, and characterize the material. The microstructure would need to be tracked with a non-destructive 3D technique such as 3D x-ray computed tomography [96] to track the void's growth. In general, though, more experimental data of this type, tracking the void growth prior to coalescence is still necessary to validate simulations to eventually enable prediction of the progress of ductile failure in porous metals.

There are many opportunities to further explore the growth of voids in metals using simulations that explicitly model the void. First, applying other models (MD, DD, FEA) to similar biphase systems to validate the occurrence of emergent void growth in these systems is a necessary step prior to continued FFT simulations exploring emergent behavior. If emergent growth is indeed a possible phenomenon, the lower-scale models (MD, DD) might better identify its contributing mechanisms and how it is affected by void length scale/size. Other higher-scale models, such as those that incorporate dislocation climb or accounting for drag and relativistic effects to model higher strain rates, might also look into emergent growth as a possible phenomenon.

FEA and FFT could be used to continue to extend our understanding of emergent behavior at the grain scale. Specific grain boundary behaviors, such as grain boundary sliding, can be taken into account to see whether this affects void growth. Strain-gradient plasticity is also a possible avenue to explore, as the LS-EVP-FFT has a version developed that incorporates strain-gradient plasticity. The phase boundary simulations in this dissertation indicated that the strain gradient was higher in the bicrystal than in single crystal counterparts when emergent behavior was present, and higher in the part of the bicrystal that experienced faster growth. Using the LS-EVP-FFT that incorporates strain-gradient theory to model void growth might suppress these behaviors, since strain gradient models tend to reduce high strain gradients. Further modeling could also be used to generate a grain/phase orientation map to predict emergent behavior for FCC and BCC grain and phase boundaries.

Finally, the conclusions of the dissertation are important for developing better implicit models. If total void growth is all that is concerned, the grain or phase boundary inclination angle does not strongly affect void growth at grain boundaries, nor does the grain/phase misorientation. The crystal orientation relative to the loading direction is a stronger predictor of void growth, but care should be taken to capture emergent behavior.

The author and collaborators have used DVP-FFT to develop an improved damage model for porous FCC, using the average stress potential of voided single crystals using single-step simulations [49]. For developing and calibrating damage models, DVP-FFT would likely sufficiently calculate the emergent behavior in simple grain boundaries within the first step, as the simulations in this dissertation indicated that emergent behavior is immediately present in those cases. Furthermore, if the hardening rate is the same in polycrystalline or multiphase metals, predicting the growth of voids at grain or phase boundaries as two voids in each phase should suffice as a first approximation. However, to calibrate the model to account for materials with different hardening behavior, as in BCC/FCC phase boundaries, longer simulations might be necessary to adequately capture the behavior. More research should be conducted on phase boundaries in metals with distinct hardening rates to understand the interaction between void growth and stress state before further implicit models are developed.

Appendix A

Von Mises plastic strain averages and field comparisons around voids at FCC/BCC interphase boundaries

To illustrate and confirm the connection between plastic strain and void growth, Figure A.1 shows f_{v1} and f_{v3} see Table 5.3 for reference to the v variables) as a function of the corresponding manipulation of average and standard deviation of von Mises plastic strain, $\varepsilon^{\mathrm{p}}_{\mathrm{vM}}$. In chapter 4, the maximum slip rate was shown to be an indicator of emergent behavior in single phase bicrystals, and $\varepsilon^{\mathrm{p}}_{\mathrm{vM}}$ is related to the total sum of the slip. The positive correlation in Figure A.1(a) supports the idea that slip is enhanced in the material in the emergent cases. The average von Mises plastic strain, and therefore overall slip, is enhanced in the emergent cases, but it also seems that the variation is greater. The standard deviation, in fact, seems to have a stronger relationship for both v1 and v3. To confirm, Figure A.1(b,d) demonstrates the standard deviation in the von Mises plastic strain. As shown, the Ta grains demonstrate a higher variation of von Mises plastic strain in all Cu/Ta (triangles) cases, in line with the preferred growth in Ta.

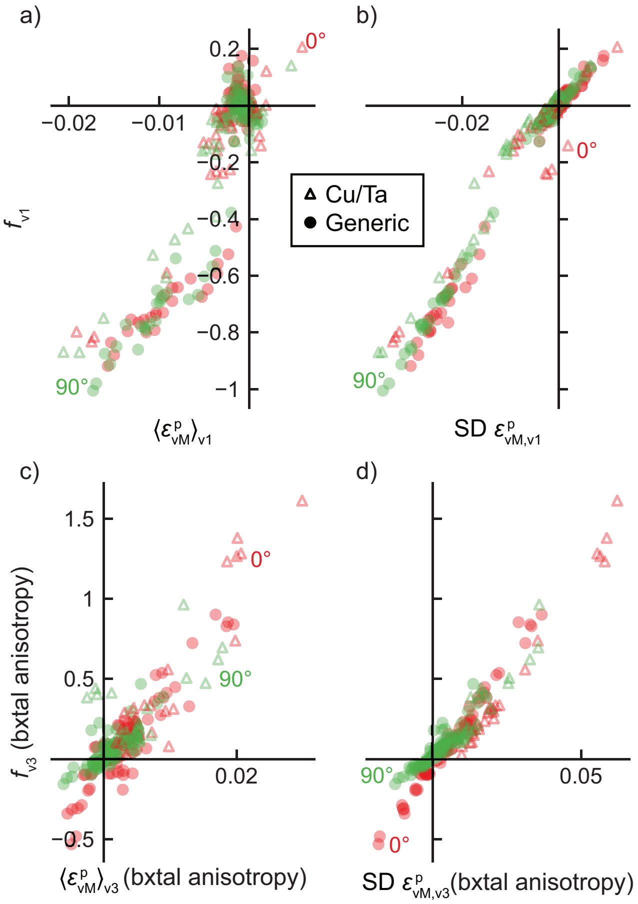

Figure A.1: Plot of f/f_0 against the average (a,c) average and (b,d) the standard deviation of von Mises plastic strain, $\varepsilon^{\mathrm{p}}_{\mathrm{vM}}$. Specifically, the plots show (a) f_{v1} vs $\langle\varepsilon^{\mathrm{p}}_{\mathrm{vM}}\rangle_{\mathrm{v1}}$, (b) f_{v1} vs the v1 standard deviation of von Mises plastic strain, SD $\left(\varepsilon^{\mathrm{p}}_{\mathrm{vM}}\right)_{\mathrm{v1}}$, (c) f_{v3} vs $\langle\varepsilon^{\mathrm{p}}_{\mathrm{vM}}\rangle_{\mathrm{v3}}$, (d) f_{v3} vs the v3 standard deviation of von Mises plastic strain, SD $\left(\varepsilon^{\mathrm{p}}_{\mathrm{vM}}\right)_{\mathrm{v3}}$. Darker symbols are the cases shown in figures A.2 and 5.13.

Considering the apparent variations in the bicrystals that show emergent behavior compared to their single crystal counterparts, we looked further into the local fields for von Mises plastic strain to see if the strain gradient is enhanced in the case of emergent materials, Figure A.2 shows the von Mises plastic strain field, $\varepsilon_{\mathrm{vM}}(\mathbf{x})$, at 5% total axial strain in the Cu/Ta material, shown in the xz-plane for: (a) emergent [011]−[001], (b) low-contrast [011]−[021], and (c) high-contrast $[\bar{1}25]$−[111] grain pairs, marked by darker symbols in Figure A.1(a,b). The top row shows the plastic strain field in single crystals, the middle row shows the field in the bicrystals, and the bottom row shows the difference between the field in the bicrystal and the corresponding single crystalline fields. Compared to the other two grain pairs, the (a) emergent [001]−[011] grain pair shows a significant increase in plastic strain on one half (specifically in the Ta [011] grain) of the bicrystal, particularly near the void, while both the (b) low-contrast and (c) high-contrast pairs show no significant elevation in plastic strain without a decrease on the opposite side. This increase in the maximum plastic strain appears to happen over the same distance, meaning that the strain gradient in those regions is likewise enhanced. In general, in the bicrystal, the Ta half shows elevated plastic strains near the void.

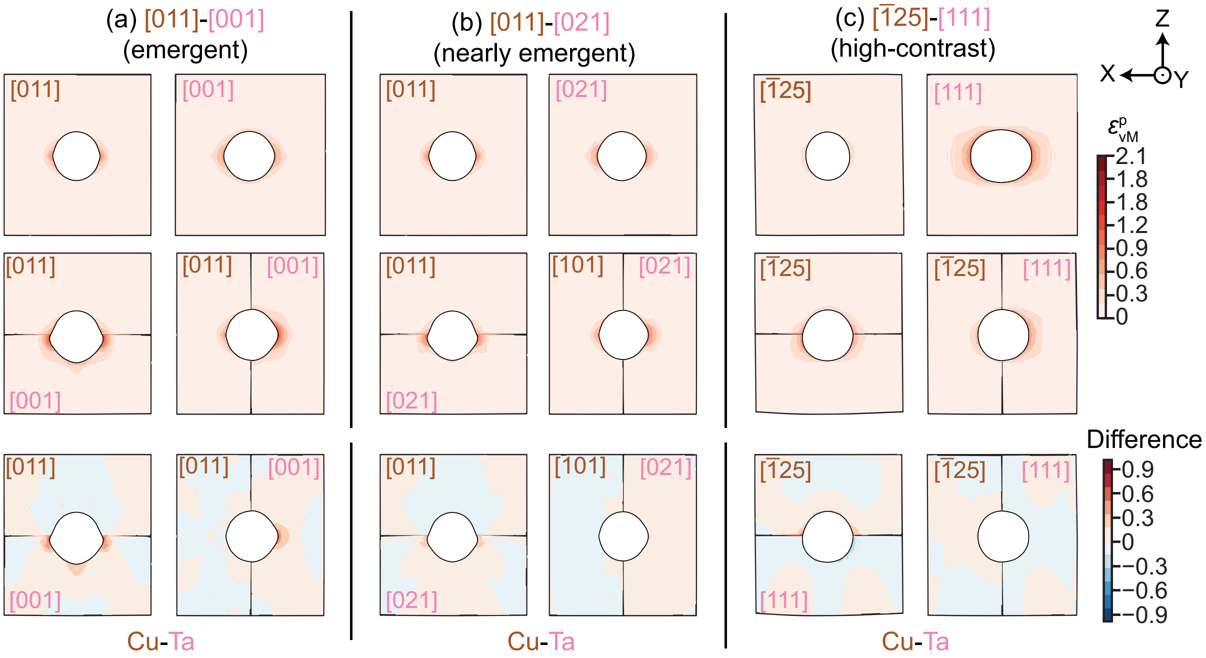

Figure A.2: Contour plots of von Mises plastic strain field, $\varepsilon_{\mathrm{vM}}(\mathbf{x})$, in various single crystals (top row), bicrystals (middle row), and the difference between the single crystal simulations and bicrystal cells of the same orientation (bottom row) in the Cu/Ta material at 5% total axial strain. The three orientation pairs are (a) $[011]-[001]$ (left two columns), (b) $[011]-[021]$ (middle two columns), and (c) $[\bar{1}25]-[111]$ (right two columns), which represent emergent, low-contrast, and high-contrast simulations, respectively.

Bibliography

[1] C. A. Bronkhorst, G. T. Gray, F. L. Addessio, V. Livescu, N. K. Bourne, S. A. McDonald, and P. J. Withers. Response and representation of ductile damage under varying shock loading conditions in tantalum. *Journal of Applied Physics*, 119(8):085103, 2 2016. ISSN 0021-8979. doi: 10.1063/1.4941823. URL `http://aip.scitation.org/doi/10.1063/1.4941823`.

[2] C. Ling, J. Besson, S. Forest, B. Tanguy, F. Latourte, and E. Bosso. An elastoviscoplastic model for porous single crystals at finite strains and its assessment based on unit cell simulations. *International Journal of Plasticity*, 84:58–87, 1 2016. ISSN 07496419. doi: 10.1016/j.ijplas.2016.05.001.

[3] M. A. Meyers and C. Taylor Aimone. Dynamic fracture (spalling) of metals. *Progress in Materials Science*, 28(1):1–96, 1 1983. ISSN 0079-6425. doi: 10.1016/0079-6425(83)90003-8.

[4] D. R. Curran, L. Seaman, and D. A. Shockey. Dynamic failure of solids. *Physics Reports*, 147(5-6):253–388, 3 1987. ISSN 0370-1573. doi: 10.1016/0370-1573(87) 90049-4.

[5] N. A. Pedrazas, D. L. Worthington, D. A. Dalton, P. A. Sherek, S. P. Steuck, H. J. Quevedo, A. C. Bernstein, E. M. Taleff, and T. Ditmire. Effects of microstructure and composition on spall fracture in aluminum. *Materials Science and Engineering: A*, 536:117–123, 2 2012. ISSN 0921-5093. doi: 10.1016/J.MSEA.2011.12.083.

[6] S. Fensin, J. Escobedo-Diaz, C. Brandl, E. Cerreta, G. Gray, T. Germann, and S. Valone. Effect of loading direction on grain boundary failure under shock loading. *Acta Materialia*, 64:113–122, 2 2014. ISSN 13596454. doi: 10.1016/j.actamat.2013.11.026. URL `https://linkinghub.elsevier.com/retrieve/pii/S1359645413008768`.

[7] T. Francis, P. F. Rottmann, A. T. Polonsky, M.-A. Charpagne, M. P. Echlin, V. Livescu, D. Jones, G. Gray, M. De Graef, and T. M. Pollock. Multimodal 3D characterization of voids in shock-loaded tantalum: Implications for ductile spallation mechanisms. *Acta Materialia*, 215:117057, 8 2021. ISSN 1359-6454. doi: 10.1016/J.ACTAMAT.2021.117057.

[8] W. Han, E. Cerreta, N. Mara, I. Beyerlein, J. Carpenter, S. Zheng, C. Trujillo, P. Dickerson, and A. Misra. Deformation and failure of shocked bulk Cu–Nb nanolaminates. *Acta Materialia*, 63:150–161, 1 2014. ISSN 1359-6454. doi: 10.1016/J.ACTAMAT.2013.10.019. URL `https://www.sciencedirect.com/science/article/pii/S1359645413007702`.

[9] J. A. Slotwinski, E. J. Garboczi, and K. M. Hebenstreit. Porosity Measurements and Analysis for Metal Additive Manufacturing Process Control. *Journal of Research of the National Institute of Standards and Technology*, 119:494, 2014. ISSN 21657254. doi: 10.6028/JRES.119.019. URL `/pmc/articles/PMC4487290//pmc/articles/PMC4487290/?report=abstracthttps://www.ncbi.nlm.nih.gov/pmc/articles/PMC4487290/`.

[10] F. H. Kim and S. P. Moylan. Literature review of metal additive manufacturing defects. Technical report, National Institute of Standards and Technology, Gaithersburg, MD, 5 2018. URL `http://nvlpubs.nist.gov/nistpubs/ams/NIST.AMS.100-16.pdf`.

[11] M. Montazeri, A. R. Nassar, A. J. Dunbar, and P. Rao. In-process monitoring of porosity in additive manufacturing using optical emission spectroscopy. *https://doi.org/10.1080/24725854.2019.1659525*, 52(5):500–515, 5 2019. ISSN 24725862. doi: 10.1080/24725854.2019.1659525. URL `https://www.tandfonline.com/doi/abs/10.1080/24725854.2019.1659525`.

[12] A. Sola and A. Nouri. Microstructural porosity in additive manufacturing: The formation and detection of pores in metal parts fabricated by powder bed fusion. *Journal of Advanced Manufacturing and Processing*, 1(3):e10021, 7 2019. ISSN 2637-403X. doi: 10.1002/AMP2.10021. URL `https://onlinelibrary.wiley.com/doi/full/10.1002/amp2.10021https://onlinelibrary.wiley.com/doi/abs/10.1002/amp2.10021https://aiche.onlinelibrary.wiley.com/doi/10.1002/amp2.10021`.

[13] S. Ahmad, S. Mujumdar, and V. Varghese. Role of porosity in machinability of additively manufactured Ti-6Al-4V. *Precision Engineering*, 76:397–406, 7 2022. ISSN 0141-6359. doi: 10.1016/J.PRECISIONENG.2022.04.010.

[14] C. Reina, J. Marian, and M. Ortiz. Nanovoid nucleation by vacancy aggregation and vacancy-cluster coarsening in high-purity metallic single crystals. *Physical Review B - Condensed Matter and Materials Physics*, 84(10):104117, 9 2011. ISSN 10980121. doi: 10.1103/PHYSREVB.84.104117/FIGURES/13/MEDIUM. URL `https://journals.aps.org/prb/abstract/10.1103/PhysRevB.84.104117`.

[15] H. Sui, L. Yu, W. Liu, Y. Liu, Y. Cheng, and H. Duan. Theoretical models of void nucleation and growth for ductile metals under dynamic loading: A review. *Matter*

and Radiation at Extremes, 7(1):018201, 12 2021. ISSN 2468-2047. doi: 10.1063/5.0064557. URL https://aip.scitation.org/doi/abs/10.1063/5.0064557.

[16] A. Mishra, J. Lind, M. Kumar, and A. M. Dongare. Understanding the phase transformation mechanisms that affect the dynamic response of Fe-based microstructures at the atomic scales. *Journal of Applied Physics*, 130(21):215902, 12 2021. ISSN 0021-8979. doi: 10.1063/5.0069935. URL https://aip.scitation.org/doi/abs/10.1063/5.0069935.

[17] S. Kanamori, M. Saito, E. Abe, T. Tagwa, and T. Miyata. Effects of triaxiality and microstructure on ductile fracture of α/β Titanium alloys. *Zairyo/Journal of the Society of Materials Science, Japan*, 51(8):900–905, 2002. ISSN 05145163. doi: 10.2472/jsms.51.900. URL http://www.jstage.jst.go.jp/article/jsms1963/51/8/51_8_900/_article/-char/ja/.

[18] A. L. Stevens, L. Davison, and W. E. Warren. Spall fracture in aluminum monocrystals: a dislocation-dynamics approach. *Journal of Applied Physics*, 43(12):4922–4927, 12 1972. ISSN 0021-8979. doi: 10.1063/1.1661046. URL https://aip.scitation.org/doi/abs/10.1063/1.1661046http://aip.scitation.org/doi/10.1063/1.1661046.

[19] V. A. Lubarda, M. S. Schneider, D. H. Kalantar, B. A. Remington, and M. A. Meyers. Void growth by dislocation emission. *Acta Materialia*, 52(6):1397–1408, 2004. ISSN 13596454. doi: 10.1016/j.actamat.2003.11.022.

[20] D. C. Ahn, P. Sofronis, and R. Minich. On the micromechanics of void growth by prismatic-dislocation loop emission. *Journal of the Mechanics and Physics of Solids*, 54(4):735–755, 4 2006. ISSN 0022-5096. doi: 10.1016/J.JMPS.2005.10.011.

[21] L. Wang, J. Zhou, Y. Liu, S. Zhang, Y. Wang, and W. Xing. Nanovoid growth in nanocrystalline metal by dislocation shear loop emission. *Materials Science and Engineering: A*, 528(16-17):5428–5434, 6 2011. ISSN 0921-5093. doi: 10.1016/J.MSEA.2011.03.074.

[22] F. D. Fischer and T. Antretter. Deformation, stress state and thermodynamic force for a growing void in an elastic–plastic material. *International Journal of Plasticity*, 25(10):1819–1832, 10 2009. ISSN 0749-6419. doi: 10.1016/J.IJPLAS.2008.11.007.

[23] H. J. Chang, J. Segurado, and J. LLorca. Three-dimensional dislocation dynamics analysis of size effects on void growth. *Scripta Materialia*, 95(1):11–14, 1 2015. ISSN 1359-6462. doi: 10.1016/J.SCRIPTAMAT.2014.09.018.

[24] R. B. Sills and B. L. Boyce. Void growth by dislocation adsorption. *Materials Research Letters*, 8(3):103–109, 3 2020. ISSN 21663831. doi: 10.1080/21663831.2019.1702114/SUPPL{_}FILE/TMRL{_}A{_}1702114{_}SM5828.PDF. URL https://www.tandfonline.com/doi/abs/10.1080/21663831.2019.1702114.

[25] R. O. Scattergood and D. J. Bacon. The strengthening effect of voids. *Acta Metallurgica*, 30(8):1665–1677, 8 1982. ISSN 0001-6160. doi: 10.1016/0001-6160(82) 90188-2.

[26] J. Dérès, L. Proville, and M. C. Marinica. Dislocation depinning from nano-sized irradiation defects in a bcc iron model. *Acta Materialia*, 99:99–105, 10 2015. ISSN 1359-6454. doi: 10.1016/J.ACTAMAT.2015.07.067.

[27] F. Bergner, F. Gillemot, M. Hernández-Mayoral, M. Serrano, G. Török, A. Ulbricht, and E. Altstadt. Contributions of Cu-rich clusters, dislocation loops and nanovoids to the irradiation-induced hardening of Cu-bearing low-Ni reactor pressure vessel steels. *Journal of Nuclear Materials*, 461:37–44, 6 2015. ISSN 0022-3115. doi: 10.1016/J.JNUCMAT.2015.02.031.

[28] N. Li, M. Demkowicz, N. Mara, Y. Wang, and A. Misra. Hardening due to Interfacial He Bubbles in Nanolayered Composites. *Materials Research Letters*, 4(2):75–82, 4 2016. ISSN 2166-3831. doi: 10.1080/21663831.2015.1110730. URL `https://www.tandfonline.com/doi/abs/10.1080/21663831.2015.1110730http://www.tandfonline.com/doi/full/10.1080/21663831.2015.1110730`.

[29] A. M. Roach, S. Xu, D. J. Luscher, D. S. Gianola, and I. J. Beyerlein. Interaction of extended dislocations with nanovoid clusters. Submitted for publication.

[30] M. Cheng, C. Li, M. X. Tang, L. Lu, Z. Li, and S. N. Luo. Intragranular void formation in shock-spalled tantalum: Mechanisms and governing factors. *Acta Materialia*, 148:38–48, 4 2018. ISSN 13596454. doi: 10.1016/j.actamat.2018.01.029.

[31] W. A. Witzen, M. P. Echlin, M.-A. Charpagne, T. M. Pollock, and I. J. Beyerlein. Subgrain geometrically necessary dislocation density mapping in spalled Ta in three dimensions. *Acta Materialia*, 244:118366, 1 2023. ISSN 13596454. doi: 10.1016/j.actamat.2022.118366. URL `https://linkinghub.elsevier.com/retrieve/pii/S1359645422007443`.

[32] A. Needleman. Void Growth in an Elastic-Plastic Medium. *Journal of Applied Mechanics*, 39(4):964, 12 1972. ISSN 00218936. doi: 10.1115/1.3422899. URL `http://AppliedMechanics.asmedigitalcollection.asme.org/article.aspx?articleid=1400610`.

[33] J. Koplik and A. Needleman. Void growth and coalescence in porous plastic solids. *International Journal of Solids and Structures*, 24(8):835–853, 1 1988. ISSN 0020-7683. doi: 10.1016/0020-7683(88)90051-0.

[34] A. A. Benzerga and J. B. Leblond. *Ductile Fracture by Void Growth to Coalescence*, volume 44. Elsevier, 1 2010. doi: 10.1016/S0065-2156(10)44003-X.

[35] J. R. Rice and D. M. Tracey. On the ductile enlargement of voids in triaxial stress fields. *Journal of the Mechanics and Physics of Solids*, 17(3):201–217, 6 1969. ISSN 00225096. doi: 10.1016/0022-5096(69)90033-7.

[36] A. L. Gurson. Continuum Theory of Ductile Rupture by Void Nucleation and Growth: Part I—Yield Criteria and Flow Rules for Porous Ductile Media. *Journal of Engineering Materials and Technology*, 99(1):2–15, 1 1977. ISSN 15288889. doi: 10.1115/1.3443401. URL http://materialstechnology.asmedigitalcollection.asme.org/article.aspx?articleid=1422194http://asmedigitalcollection.asme.org/materialstechnology/article-pdf/99/1/2/5788715/2_1.pdf.

[37] V. Tvergaard. Influence of voids on shear band instabilities under plane strain conditions. *International Journal of Fracture*, 17(4):389–407, 8 1981. ISSN 03769429. doi: 10.1007/BF00036191. URL https://link.springer.com/article/10.1007/BF00036191.

[38] V. Tvergaard. Material Failure by Void Growth to Coalescence. In J. W. Hutchinson and T. Y. Wu, editors, *Advances in Applied Mechanics*, volume 27, pages 83–151. Elsevier, 1 1989. ISBN 9780120020270. doi: 10.1016/S0065-2156(08)70195-9. URL https://www.sciencedirect.com/science/article/pii/S0065215608701959https://linkinghub.elsevier.com/retrieve/pii/S0065215608701959.

[39] A. Needleman, V. Tvergaard, and J. W. Hutchinson. Void Growth in Plastic Solids. In *Topics in Fracture and Fatigue*, pages 145–178. Springer New York, New York, NY, 1992. doi: 10.1007/978-1-4612-2934-6{_}4. URL http://link.springer.com/10.1007/978-1-4612-2934-6_4.

[40] V. Tvergaard and A. Needleman. Analysis of the cup-cone fracture in a round tensile bar. *Acta Metallurgica*, 32(1):157–169, 1 1984. ISSN 00016160. doi: 10.1016/0001-6160(84)90213-X.

[41] J. B. Leblond, G. Perrin, and P. Suquet. Exact results and approximate models for porous viscoplastic solids. *International Journal of Plasticity*, 10(3):213–235, 1 1994. ISSN 07496419. doi: 10.1016/0749-6419(94)90001-9.

[42] M. Gologanu, J. B. Leblond, and J. Devaux. Approximate models for ductile metals containing nonspherioal voids-case of axisymmetric oblate ellipsoidal cavities. *Journal of Engineering Materials and Technology, Transactions of the ASME*, 116(3):290–297, 7 1994. ISSN 15288889. doi: 10.1115/1.2904290. URL http://asmedigitalcollection.asme.org/materialstechnology/article-pdf/116/3/290/5516590/290_1.pdf.

[43] M. Gărăjeu, J. C. Michel, and P. Suquet. A micromechanical approach of damage in viscoplastic materials by evolution in size, shape and distribution of voids. *Computer Methods in Applied Mechanics and Engineering*, 183(3-4):223–246, 3 2000. ISSN 00457825. doi: 10.1016/S0045-7825(99)00220-0.

[44] A. A. Benzerga and J. Besson. Plastic potentials for anisotropic porous solids. *European Journal of Mechanics, A/Solids*, 20(3):397–434, 5 2001. ISSN 09977538. doi: 10.1016/S0997-7538(01)01147-0.

[45] V. Monchiet, O. Cazacu, E. Charkaluk, and D. Kondo. Macroscopic yield criteria for plastic anisotropic materials containing spheroidal voids. *International Journal of Plasticity*, 24(7):1158–1189, 7 2008. ISSN 07496419. doi: 10.1016/j.ijplas.2007.08.008.

[46] O. Cazacu and J. B. Stewart. Analytic plastic potential for porous aggregates with matrix exhibiting tension-compression asymmetry. *Journal of the Mechanics and Physics of Solids*, 57(2):325–341, 2 2009. ISSN 00225096. doi: 10.1016/j.jmps.2008.10.010.

[47] J. B. Stewart and O. Cazacu. Analytical yield criterion for an anisotropic material containing spherical voids and exhibiting tension-compression asymmetry. *International Journal of Solids and Structures*, 48(2):357–373, 1 2011. ISSN 00207683. doi: 10.1016/j.ijsolstr.2010.10.009.

[48] X. Han, J. Besson, S. Forest, B. Tanguy, and S. Bugat. A yield function for single crystals containing voids. *International Journal of Solids and Structures*, 50(14-15):2115–2131, 7 2013. ISSN 00207683. doi: 10.1016/j.ijsolstr.2013.02.005.

[49] A. Rovinelli, P. G. Christodoulou, R. A. Lebensohn, and L. Capolungo. Generalization of the concept of gauge factor to predict void growth in single crystals deforming by diffusion and dislocation creep. In preparation.

[50] S. K. Yerra, C. Tekoğlu, F. Scheyvaerts, L. Delannay, P. Van Houtte, and T. Pardoen. Void growth and coalescence in single crystals. *International Journal of Solids and Structures*, 47(7-8):1016–1029, 4 2010. ISSN 00207683. doi: 10.1016/j.ijsolstr.2009.12.019.

[51] T. Chen, R. Sakidja, W. Y. Ching, and C. Zhou. Crystal Plasticity Modeling of Void Growth on Grain Boundaries in Ni-Based Superalloys. *JOM*, 71(11):3859–3868, 11 2019. ISSN 15431851. doi: 10.1007/s11837-019-03694-3. URL `https://doi.org/10.1007/s11837-019-03694-3https://link.springer.com/article/10.1007/s11837-019-03694-3`.

[52] H. J. Guo, C. Ling, E. P. Busso, Z. Zhong, and D. F. Li. Crystal plasticity based investigation of micro-void evolution under multi-axial loading conditions.

International Journal of Plasticity, 129:102673, 6 2020. ISSN 07496419. doi: 10.1016/j.ijplas.2020.102673.

[53] S. Traiviratana, E. M. Bringa, D. J. Benson, and M. A. Meyers. Void growth in metals: Atomistic calculations. *Acta Materialia*, 56(15):3874–3886, 2008. ISSN 13596454. doi: 10.1016/j.actamat.2008.03.047.

[54] K. J. Zhao, C. Q. Chen, Y. P. Shen, and T. J. Lu. Molecular dynamics study on the nano-void growth in face-centered cubic single crystal copper. *Computational Materials Science*, 46(3):749–754, 9 2009. ISSN 0927-0256. doi: 10.1016/J.COMMATSCI.2009.04.034.

[55] E. M. Bringa, S. Traiviratana, and M. A. Meyers. Void initiation in fcc metals: Effect of loading orientation and nanocrystalline effects. *Acta Materialia*, 58(13):4458–4477, 2010. ISSN 13596454. doi: 10.1016/j.actamat.2010.04.043. URL `www.elsevier.com/locate/actamathttp://dx.doi.org/10.1016/j.actamat.2010.04.043`.

[56] Y. Tang, E. M. Bringa, and M. A. Meyers. Ductile tensile failure in metals through initiation and growth of nanosized voids. *Acta Materialia*, 60(12):4856–4865, 7 2012. ISSN 1359-6454. doi: 10.1016/J.ACTAMAT.2012.05.030.

[57] V. Krasnikov and A. Mayer. Plasticity driven growth of nanovoids and strength of aluminum at high rate tension: Molecular dynamics simulations and continuum modeling. *International Journal of Plasticity*, 74:75–91, 11 2015. ISSN 07496419. doi: 10.1016/j.ijplas.2015.06.007. URL `https://linkinghub.elsevier.com/retrieve/pii/S0749641915001035`.

[58] Y. Cui and Z. Chen. Material transport via the emission of shear loops during void growth: A molecular dynamics study. *Journal of Applied Physics*, 119(22):225102, 6 2016. ISSN 0021-8979. doi: 10.1063/1.4953089. URL `http://aip.scitation.org/doi/10.1063/1.4953089`.

[59] Y. Cui, Z. Chen, and Y. Ju. Fundamental insights into the mass transfer via full dislocation loops due to alternative surface cuts. *International Journal of Solids and Structures*, 161:42–54, 4 2019. ISSN 00207683. doi: 10.1016/j.ijsolstr.2018.11.005. URL `https://linkinghub.elsevier.com/retrieve/pii/S0020768318304360`.

[60] L. D. Nguyen and D. H. Warner. Improbability of void growth in aluminum via dislocation nucleation under typical laboratory conditions. *Physical Review Letters*, 108(3):035501, 1 2012. ISSN 00319007. doi: 10.1103/PHYSREVLETT.108.035501/FIGURES/3/MEDIUM. URL `https://journals.aps.org/prl/abstract/10.1103/PhysRevLett.108.035501`.

[61] M. M. Sichani and D. E. Spearot. A molecular dynamics study of the role of grain size and orientation on compression of nanocrystalline Cu during shock. *Computational Materials Science*, 108:226–232, 10 2015. ISSN 0927-0256. doi: 10.1016/J.COMMATSCI.2015.07.021.

[62] C. M. Liu, C. Xu, Y. Cheng, X. R. Chen, and L. C. Cai. Orientation-dependent responses of tungsten single crystal under shock compression via molecular dynamics simulations. *Computational Materials Science*, 110:359–367, 12 2015. ISSN 0927-0256. doi: 10.1016/J.COMMATSCI.2015.08.051.

[63] G. Sainath and B. K. Choudhary. Orientation dependent deformation behaviour of BCC iron nanowires. *Computational Materials Science*, 111:406–415, 1 2016. ISSN 0927-0256. doi: 10.1016/J.COMMATSCI.2015.09.055.

[64] E. N. Hahn, S. J. Fensin, and T. C. Germann. The role of grain boundary orientation on void nucleation in tantalum. In *AIP Conference Proceedings 1979*, page 050008, 2018. ISBN 9780735416932. doi: 10.1063/1.5044791. URL `https://doi.org/10.1063/1.5044791https://doi.org/10.1063/1.5044784https://doi.org/10.1063/1.4971590`.

[65] M. J. Echeverria, S. Galitskiy, A. Mishra, R. Dingreville, and A. M. Dongare. Understanding the plasticity contributions during laser-shock loading and spall failure of Cu microstructures at the atomic scales. *Computational Materials Science*, 198: 110668, 10 2021. ISSN 0927-0256. doi: 10.1016/J.COMMATSCI.2021.110668.

[66] Y. Zhang, S. Jiang, X. Zhu, and D. Sun. Orientation dependence of void growth at triple junction of grain boundaries in nanoscale tricrystal nickel film subjected to uniaxial tensile loading. *Journal of Physics and Chemistry of Solids*, 98:220–232, 2016. ISSN 00223697. doi: 10.1016/j.jpcs.2016.07.018.

[67] T. W. Chiang, A. Chernatynskiy, S. B. Sinnott, and S. R. Phillpot. Interaction between voids and grain boundaries in UO2 by molecular-dynamics simulation. *Journal of Nuclear Materials*, 448(1-3):53–61, 5 2014. ISSN 0022-3115. doi: 10.1016/J.JNUCMAT.2014.01.027.

[68] J. Segurado and J. Llorca. An analysis of the size effect on void growth in single crystals using discrete dislocation dynamics. *Acta Materialia*, 57(5):1427–1436, 3 2009. ISSN 1359-6454. doi: 10.1016/J.ACTAMAT.2008.11.031.

[69] J. Segurado and J. LLorca. Discrete dislocation dynamics analysis of the effect of lattice orientation on void growth in single crystals. *International Journal of Plasticity*, 26(6):806–819, 6 2010. ISSN 0749-6419. doi: 10.1016/J.IJPLAS.2009.10.009.

[70] R. J. Asaro. Crystal Plasticity. *Journal of Applied Mechanics*, 50(4b):921–934, 12 1983. doi: 10.1115/1.3167205. URL `http://AppliedMechanics.asmedigitalcollection.asme.org/article.aspx?articleid=1407286`.

[71] A. Srivastava and A. Needleman. Effect of crystal orientation on porosity evolution in a creeping single crystal. *Mechanics of Materials*, 90:10–29, 11 2015. ISSN 01676636. doi: 10.1016/j.mechmat.2015.01.015.

[72] M. Dakshinamurthy, K. Kowalczyk-Gajewska, and G. Vadillo. Influence of crystallographic orientation on the void growth at the grain boundaries in bi-crystals. *International Journal of Solids and Structures*, 212:61–79, 3 2021. ISSN 00207683. doi: 10.1016/j.ijsolstr.2020.11.035.

[73] U. B. Asim, M. A. Siddiq, and M. E. Kartal. A CPFEM based study to understand the void growth in high strength dual-phase titanium alloy (Ti-10V-2Fe-3Al). *International Journal of Plasticity*, 122:188–211, 11 2019. ISSN 07496419. doi: 10.1016/j.ijplas.2019.07.002.

[74] W. Jeong, C. H. Lee, J. Moon, D. Jang, and M. G. Lee. Grain Scale Representative Volume Element Simulation to Investigate the Effect of Crystal Orientation on Void Growth in Single and Multi-Crystals. *Metals 2018, Vol. 8, Page 436*, 8(6):436, 6 2018. ISSN 20754701. doi: 10.3390/MET8060436. URL `https://www.mdpi.com/2075-4701/8/6/436/htmhttps://www.mdpi.com/2075-4701/8/6/436`.

[75] F. Fritzen, S. Forest, T. Böhlke, D. Kondo, and T. Kanit. Computational homogenization of elasto-plastic porous metals. *International Journal of Plasticity*, 29(1):102–119, 2 2012. ISSN 07496419. doi: 10.1016/j.ijplas.2011.08.005.

[76] H. Moulinec and P. Suquet. A fast numerical method for computing the linear and nonlinear mechanical properties of composites. *C. R. Acad. Sci. Paris*, 318(II):1417–1423, 1994. URL `https://hal.archives-ouvertes.fr/hal-03019226`.

[77] H. Moulinec and P. Suquet. A numerical method for computing the overall response of nonlinear composites with complex microstructure. *Computer Methods in Applied Mechanics and Engineering*, 157(1-2):69–94, 4 1998. ISSN 00457825. doi: 10.1016/S0045-7825(97)00218-1.

[78] J. Michel, H. Moulinec, and P. Suquet. A Computational Method Based on Augmented Lagrangians and Fast Fourier Transforms for Composites with High Contrast, 2000. URL `https://www.techscience.com/CMES/v1n2/24683`.

[79] J. C. Michel, H. Moulinec, and P. Suquet. A computational scheme for linear and non-linear composites with arbitrary phase contrast. *International Journal for Numerical Methods in Engineering*, 52(12):139–160, 9 2001. ISSN 00295981. doi: 10.1002/nme.275. URL `http://doi.wiley.com/10.1002/nme.275`.

[80] R. A. Lebensohn. N-site modeling of a 3D viscoplastic polycrystal using Fast Fourier Transform. *Acta Materialia*, 49(14):2723–2737, 8 2001. ISSN 13596454. doi: 10.1016/S1359-6454(01)00172-0.

[81] R. A. Lebensohn, R. Brenner, O. Castelnau, and A. D. Rollett. Orientation image-based micromechanical modelling of subgrain texture evolution in polycrystalline copper. *Acta Materialia*, 56(15):3914–3926, 9 2008. ISSN 13596454. doi: 10.1016/j.actamat.2008.04.016. URL `https://linkinghub.elsevier.com/retrieve/pii/S1359645408002887`.

[82] R. A. Lebensohn, M. Montagnat, P. Mansuy, P. Duval, J. Meysonnier, and A. Philip. Modeling viscoplastic behavior and heterogeneous intracrystalline deformation of columnar ice polycrystals. *Acta Materialia*, 57(5):1405–1415, 3 2009. ISSN 13596454. doi: 10.1016/j.actamat.2008.10.057.

[83] R. A. Lebensohn, A. K. Kanjarla, and P. Eisenlohr. An elasto-viscoplastic formulation based on fast Fourier transforms for the prediction of micromechanical fields in polycrystalline materials. *International Journal of Plasticity*, 32-33:59–69, 5 2012. ISSN 07496419. doi: 10.1016/j.ijplas.2011.12.005. URL `http://dx.doi.org/10.1016/j.ijplas.2011.12.005https://linkinghub.elsevier.com/retrieve/pii/S0749641911001951`.

[84] P. Eisenlohr, M. Diehl, R. A. Lebensohn, and F. Roters. A spectral method solution to crystal elasto-viscoplasticity at finite strains. *International Journal of Plasticity*, 46:37–53, 7 2013. ISSN 07496419. doi: 10.1016/j.ijplas.2012.09.012.

[85] N. Lahellec, J. C. Michel, H. Moulinec, and P. Suquet. Analysis of Inhomogeneous Materials at Large Strains using Fast Fourier Transforms. In C. Miehe, editor, *IUTAM Symposium on Computational Mechanics of Solid Materials at Large Strains*, pages 247–258. Springer, Dordrecht, Stuttgart, Germany, 8 2003. doi: 10.1007/978-94-017-0297-3{_}22. URL `https://link.springer.com/chapter/10.1007/978-94-017-0297-3_22https://link.springer.com/10.1007/978-94-017-0297-3_22`.

[86] F. Roters, M. Diehl, P. Shanthraj, P. Eisenlohr, C. Reuber, S. L. Wong, T. Maiti, A. Ebrahimi, T. Hochrainer, H. O. Fabritius, S. Nikolov, M. Friák, N. Fujita, N. Grilli, K. G. Janssens, N. Jia, P. J. Kok, D. Ma, F. Meier, E. Werner, M. Stricker, D. Weygand, and D. Raabe. DAMASK – The Düsseldorf Advanced Material Simulation Kit for modeling multi-physics crystal plasticity, thermal, and damage phenomena from the single crystal up to the component scale. *Computational Materials Science*, 158:420–478, 2 2019. ISSN 0927-0256. doi: 10.1016/J.COMMATSCI.2018.04.030.

[87] A. Marano, L. Gélébart, and S. Forest. Intragranular localization induced by softening crystal plasticity: Analysis of slip and kink bands localization modes from

high resolution FFT-simulations results. *Acta Materialia*, 175:262–275, 8 2019. ISSN 1359-6454. doi: 10.1016/J.ACTAMAT.2019.06.010.

[88] S. Lucarini and J. Segurado. DBFFT: A displacement based FFT approach for non-linear homogenization of the mechanical behavior. *International Journal of Engineering Science*, 144:103131, 11 2019. ISSN 0020-7225. doi: 10.1016/J.IJENGSCI.2019.103131.

[89] M. Zecevic, R. A. Lebensohn, and L. Capolungo. New large-strain FFT-based formulation and its application to model strain localization in nano-metallic laminates and other strongly anisotropic crystalline materials. *Mechanics of Materials*, 166:104208, 3 2022. ISSN 01676636. doi: 10.1016/j.mechmat.2021.104208. URL `https://linkinghub.elsevier.com/retrieve/pii/S0167663621004154`.

[90] R. Lebensohn, M. Idiart, P. P. Castañeda, and P.-G. Vincent. Dilatational viscoplasticity of polycrystalline solids with intergranular cavities. *Philosophical Magazine*, 91(22):3038–3067, 8 2011. ISSN 1478-6435. doi: 10.1080/14786435.2011.561811. URL `http://www.tandfonline.com/doi/abs/10.1080/14786435.2011.561811`.

[91] R. A. Lebensohn, J. P. Escobedo, E. K. Cerreta, D. Dennis-Koller, C. A. Bronkhorst, and J. F. Bingert. Modeling void growth in polycrystalline materials. *Acta Materialia*, 61(18):6918–6932, 10 2013. ISSN 1359-6454. doi: 10.1016/J.ACTAMAT.2013.08.004. URL `https://www.sciencedirect.com/science/article/pii/S1359645413005909`.

[92] N. Bilger, F. Auslender, M. Bornert, J. C. Michel, H. Moulinec, P. Suquet, and A. Zaoui. Effect of a nonuniform distribution of voids on the plastic response of voided materials: A computational and statistical analysis. In *International Journal of Solids and Structures*, volume 42, pages 517–538. Elsevier Ltd, 1 2005. doi: 10.1016/j.ijsolstr.2004.06.048.

[93] R. A. Lebensohn and O. Cazacu. Effect of single-crystal plastic deformation mechanisms on the dilatational plastic response of porous polycrystals. *International Journal of Solids and Structures*, 49(26):3838–3852, 12 2012. ISSN 0020-7683. doi: 10.1016/J.IJSOLSTR.2012.08.019. URL `https://www.sciencedirect.com/science/article/pii/S0020768312003642`.

[94] P. G. Vincent, P. Suquet, Y. Monerie, and H. Moulinec. Effective flow surface of porous materials with two populations of voids under internal pressure: II. Full-field simulations. *International Journal of Plasticity*, 56:74–98, 5 2014. ISSN 07496419. doi: 10.1016/j.ijplas.2013.11.012.

[95] P.-G. Vincent, H. Moulinec, L. Joëssel, M. I. Idiart, and M. Gărăjeu. Porous polycrystal plasticity modeling of neutron-irradiated austenitic stainless steels. *Journal of Nuclear Materials*, 542:152463, 12 2020. ISSN 00223115. doi: 10.1016/j.

jnucmat.2020.152463. URL https://linkinghub.elsevier.com/retrieve/pii/S0022311520310710.

[96] L. Lecarme, E. Maire, A. Kumar K.C., C. De Vleeschouwer, L. Jacques, A. Simar, and T. Pardoen. Heterogenous void growth revealed by in situ 3-D X-ray microtomography using automatic cavity tracking. *Acta Materialia*, 63:130–139, Jan. 2014. ISSN 13596454. doi: 10.1016/j.actamat.2013.10.014. URL http://linkinghub.elsevier.com/retrieve/pii/S1359645413007659.

[97] F. Hannard, T. Pardoen, E. Maire, C. Le Bourlot, R. Mokso, and A. Simar. Characterization and micromechanical modelling of microstructural heterogeneity effects on ductile fracture of 6xxx aluminium alloys. *Acta Materialia*, 103: 558–572, Jan. 2016. ISSN 13596454. doi: 10.1016/j.actamat.2015.10.008. URL http://linkinghub.elsevier.com/retrieve/pii/S1359645415300094.

[98] S. H. Goods and L. M. Brown. Overview No. 1. The nucleation of cavities by plastic deformation. *Acta Metallurgica*, 27(1):1–15, 1 1979. ISSN 00016160. doi: 10.1016/0001-6160(79)90051-8.

[99] F. Roters, P. Eisenlohr, L. Hantcherli, D. D. Tjahjanto, T. R. Bieler, and D. Raabe. Overview of constitutive laws, kinematics, homogenization and multiscale methods in crystal plasticity finite-element modeling: Theory, experiments, applications. *Acta Materialia*, 58(4):1152–1211, 2 2010. ISSN 13596454. doi: 10.1016/j.actamat.2009.10.058.

[100] K. Danas, M. I. Idiart, and P. P. Castañeda. A homogenization-based constitutive model for isotropic viscoplastic porous media. *International Journal of Solids and Structures*, 45(11-12):3392–3409, 6 2008. ISSN 00207683. doi: 10.1016/j.ijsolstr.2008.02.007.

[101] A. Mbiakop, A. Constantinescu, and K. Danas. An analytical model for porous single crystals with ellipsoidal voids. *Journal of the Mechanics and Physics of Solids*, 84:436–467, 11 2015. ISSN 00225096. doi: 10.1016/j.jmps.2015.07.011.

[102] J. Liu, M. Huang, Z. Li, L. Zhao, and Y. Zhu. Microvoid growth mechanism in FCC polycrystals and a statistical damage model. *International Journal of Plasticity*, 137:102888, 2 2021. ISSN 0749-6419. doi: 10.1016/J.IJPLAS.2020.102888.

[103] A. Needleman and V. Tvergaard. An analysis of ductile rupture modes at a crack tip. *Journal of the Mechanics and Physics of Solids*, 35(2):151–183, 1 1987. ISSN 00225096. doi: 10.1016/0022-5096(87)90034-2.

[104] S. Ghosh, J. Bai, and D. Paquet. Homogenization-based continuum plasticity-damage model for ductile failure of materials containing heterogeneities. *Journal of the Mechanics and Physics of Solids*, 57(7):1017–1044, 7 2009. ISSN 00225096. doi: 10.1016/j.jmps.2009.04.002.

[105] N. Bilger, F. Auslender, M. Bornert, H. Moulinec, and A. Zaoui. Bounds and estimates for the effective yield surface of porous media with a uniform or a nonuniform distribution of voids. *European Journal of Mechanics, A/Solids*, 26(5):810–836, 9 2007. ISSN 09977538. doi: 10.1016/j.euromechsol.2007.01.004.

[106] D. Sulsky and H. L. Schreyer. Axisymmetric form of the material point method with applications to upsetting and Taylor impact problems. *Computer Methods in Applied Mechanics and Engineering*, 139(1-4):409–429, 12 1996. ISSN 00457825. doi: 10.1016/S0045-7825(96)01091-2.

[107] C. Tomé, G. R. Canova, U. F. Kocks, N. Christodoulou, and J. J. Jonas. The relation between macroscopic and microscopic strain hardening in F.C.C. polycrystals. *Acta Metallurgica*, 32(10):1637–1653, 10 1984. ISSN 00016160. doi: 10.1016/0001-6160(84)90222-0.

[108] L. Delannay, P. J. Jacques, and S. R. Kalidindi. Finite element modeling of crystal plasticity with grains shaped as truncated octahedrons. *International Journal of Plasticity*, 22(10):1879–1898, 10 2006. ISSN 07496419. doi: 10.1016/j.ijplas.2006.01.008.

[109] S. Dancette, L. Delannay, K. Renard, M. A. Melchior, and P. J. Jacques. Crystal plasticity modeling of texture development and hardening in TWIP steels. *Acta Materialia*, 60(5):2135–2145, 3 2012. ISSN 13596454. doi: 10.1016/j.actamat.2012.01.015.

[110] L. Lecarme, C. Tekoğlu, and T. Pardoen. Void growth and coalescence in ductile solids with stage III and stage IV strain hardening. *International Journal of Plasticity*, 27(8):1203–1223, 8 2011. ISSN 07496419. doi: 10.1016/j.ijplas.2011.01.004.

[111] R. A. Lebensohn, Y. Liu, and P. P. Castañeda. On the accuracy of the self-consistent approximation for polycrystals: Comparison with full-field numerical simulations. *Acta Materialia*, 52(18):5347–5361, 10 2004. ISSN 13596454. doi: 10.1016/j.actamat.2004.07.040.

[112] E. J. Lieberman, R. A. Lebensohn, D. B. Menasche, C. A. Bronkhorst, and A. D. Rollett. Microstructural effects on damage evolution in shocked copper polycrystals. *Acta Materialia*, 116:270–280, 9 2016. ISSN 1359-6454. doi: 10.1016/J.ACTAMAT.2016.06.054.

[113] R. Pokharel, R. A. Lebensohn, D. C. Pagan, T. L. Ickes, B. Clausen, D. W. Brown, C.-F. Chen, D. S. Dale, and J. V. Bernier. In-Situ Grain Resolved Stress Characterization During Damage Initiation in Cu-10%W Alloy. *JOM 2019 72:1*, 72(1):48–56, 7 2019. ISSN 1543-1851. doi: 10.1007/S11837-019-03692-5. URL `https://link.springer.com/article/10.1007/s11837-019-03692-5`.

[114] D. P. Naragani, J. S. Park, P. Kenesei, and M. D. Sangid. Void coalescence and ductile failure in IN718 investigated via high-energy synchrotron X-ray tomography and diffraction. *Journal of the Mechanics and Physics of Solids*, 145, 12 2020. doi: 10.1016/J.JMPS.2020.104155.

[115] P. G. Christodoulou, S. Dancette, R. A. Lebensohn, E. Maire, and I. J. Beyerlein. Role of crystallographic orientation on intragranular void growth in polycrystalline FCC materials. *International Journal of Plasticity*, 147:103104, 12 2021. ISSN 07496419. doi: 10.1016/j.ijplas.2021.103104.

[116] F. Willot. Fourier-based schemes for computing the mechanical response of composites with accurate local fields. *Comptes Rendus Mécanique*, 343(3):232–245, 3 2015. ISSN 1631-0721. doi: 10.1016/J.CRME.2014.12.005.

[117] S. Berbenni, V. Taupin, K. S. Djaka, and C. Fressengeas. A numerical spectral approach for solving elasto-static field dislocation and g-disclination mechanics. *International Journal of Solids and Structures*, 51(23-24):4157–4175, 11 2014. ISSN 0020-7683. doi: 10.1016/J.IJSOLSTR.2014.08.009. URL `https://www.sciencedirect.com/science/article/pii/S0020768314003138`.

[118] R. A. Lebensohn and A. Needleman. Numerical implementation of non-local polycrystal plasticity using fast Fourier transforms. *Journal of the Mechanics and Physics of Solids*, 97(SI):333–351, 12 2016. ISSN 00225096. doi: 10.1016/j.jmps.2016.03.023. URL `http://dx.doi.org/10.1016/j.jmps.2016.03.023`.

[119] T. Mura. *Micromechanics of defects in solids*, volume 3 of *Mechanics of Elastic and Inelastic Solids*. Kluwer Academic Publishers, Dordrecht, second, re edition, 1987. ISBN 978-90-247-3256-2. doi: 10.1007/978-94-009-3489-4. URL `http://link.springer.com/10.1007/978-94-009-3489-4`.

[120] P. Noell, J. Carroll, K. Hattar, B. Clark, and B. Boyce. Do voids nucleate at grain boundaries during ductile rupture? *Acta Materialia*, 137:103–114, 9 2017. ISSN 13596454. doi: 10.1016/j.actamat.2017.07.004.

[121] W. H. Liu, X. M. Zhang, J. G. Tang, and Y. X. Du. Simulation of void growth and coalescence behavior with 3D crystal plasticity theory. *Computational Materials Science*, 40(1):130–139, 7 2007. ISSN 0927-0256. doi: 10.1016/J.COMMATSCI.2006.11.009.

[122] G. P. Potirniche, J. L. Hearndon, M. F. Horstemeyer, and X. W. Ling. Lattice orientation effects on void growth and coalescence in fcc single crystals. *International Journal of Plasticity*, 22(5):921–942, 5 2006. ISSN 07496419. doi: 10.1016/j.ijplas.2005.06.003.

[123] M. Yang and X. Dong. Simulation of lattice orientation effects on void growth and coalescence by crystal plasticity. *Acta Metallurgica Sinica (English Letters)*, 22(1):40–50, 2 2009. ISSN 10067191. doi: 10.1016/S1006-7191(08)60069-1. URL `https://linkinghub.elsevier.com/retrieve/pii/S1006719108600691`.

[124] W. Liu, X. Zhang, and J. Tang. Study on the growth behavior of voids located at the grain boundary. *Mechanics of Materials*, 41(7):799–809, 7 2009. ISSN 01676636. doi: 10.1016/j.mechmat.2009.02.001.

[125] W. Liu, H. Huang, and J. Tang. FEM simulation of void coalescence in FCC crystals. *Computational Materials Science*, 50(2):411–418, 12 2010. ISSN 0927-0256. doi: 10.1016/J.COMMATSCI.2010.08.033.

[126] Z. X. Wen and Z. F. Yue. On the crystallographic study of growth characterization of isolated void in the grain boundary. *Computational Materials Science*, 40(1): 140–146, 7 2007. ISSN 0927-0256. doi: 10.1016/J.COMMATSCI.2006.11.008.

[127] A. P. Sutton and R. W. Balluffi. Overview no. 61 On geometric criteria for low interfacial energy. *Acta Metallurgica*, 35(9):2177–2201, 9 1987. ISSN 0001-6160. doi: 10.1016/0001-6160(87)90067-8.

[128] R. J. Asaro. Micromechanics of Crystals and Polycrystals. *Advances in Applied Mechanics*, 23(C):1–115, 1 1983. ISSN 0065-2156. doi: 10.1016/S0065-2156(08) 70242-4.

[129] S. Zheng, S. Shao, J. Zhang, Y. Wang, M. J. Demkowicz, I. J. Beyerlein, and N. A. Mara. Adhesion of voids to bimetal interfaces with non-uniform energies. *Scientific Reports 2015 5:1*, 5(1):1–8, 10 2015. ISSN 2045-2322. doi: 10.1038/srep15428. URL `https://www.nature.com/articles/srep15428`.

[130] C. A. Bronkhorst, J. Chen, H. Cho, S. J. Fensin, G. T. Gray III, D. R. Jones, V. Livescu, P. W. Marcy, E. N. Hahn, H. M. Mourad, B. Runnels, S. A. Vander Wiel, and S. Zentgraf. Inter-Granular Mechanics of Metallic Ductile Damage under Dynamic Loading Conditions. In *Society for Engineering Science*, Madrid, Spain, 2018.

[131] J. Chen, S. N. Mathaudhu, N. Thadhani, and A. M. Dongare. Correlations between dislocation density evolution and spall strengths of Cu/Ta multilayered systems at the atomic scales: The role of spacing of KS interfaces. *Materialia*, 5:100192, 3 2019. ISSN 2589-1529. doi: 10.1016/J.MTLA.2018.100192.

[132] J. Chen, S. N. Mathaudhu, N. Thadhani, and A. M. Dongare. Unraveling the Role of Interfaces on the Spall Failure of Cu/Ta Multilayered Systems. *Scientific Reports 2020 10:1*, 10(1):1–15, 1 2020. ISSN 2045-2322. doi: 10.1038/s41598-019-57048-9. URL `https://www.nature.com/articles/s41598-019-57048-9`.

[133] K. Chockalingam, M. R. Tonks, J. D. Hales, D. R. Gaston, P. C. Millett, and L. Zhang. Crystal plasticity with Jacobian-Free Newton-Krylov. *Computational Mechanics*, 51(5):617–627, 7 2013. ISSN 01787675. doi: 10.1007/S00466-012-0741-7/METRICS. URL `https://link.springer.com/article/10.1007/s00466-012-0741-7`.

[134] Z. Feng, M. Zecevic, M. Knezevic, and R. A. Lebensohn. Predicting extreme anisotropy and shape variations in impact testing of tantalum single crystals. *International Journal of Solids and Structures*, 241:111466, 4 2022. ISSN 0020-7683. doi: 10.1016/J.IJSOLSTR.2022.111466.

[135] J. Mazumder. Design for Metallic Additive Manufacturing Machine with Capability for "Certify as You Build". *Procedia CIRP*, 36:187–192, 1 2015. ISSN 2212-8271. doi: 10.1016/J.PROCIR.2015.01.009.